Thermal-Structural analysis of High Pressure Superheater 1 of

a Heat Recovery Steam Generator

by

Hardeep Singh

A Thesis Presented in Partial Fulfillment
of the Requirements for the Degree
Master of Science

Approved July 2012 by the
Graduate Supervisory Committee:

Ramendra P. Roy, Co-Chair
Taewoo Lee, Co-Chair
Marc Mignolet

ARIZONA STATE UNIVERSITY

August 2012

ABSTRACT

High Pressure Superheater 1 (HPSH1) is the first heat exchange tube bank inside the Heat Recovery Steam Generator (HRSG) to encounter exhaust flue gas from the gas turbine of a Combined Cycle Power Plant. Steam flowing through the HPSH1 gains heat from the flue gas prior to entering the steam turbine. During cold start-ups, rapid temperature changes in operating condition give rise to significant temperature gradients in the thick-walled components of HPSH1 (manifolds, links, and headers). These temperature gradients produce thermal-structural stresses in the components. The resulting high cycle fatigue is a major concern as this can lead to premature failure of the components.

The main objective of this project was to address the thermal-structural stress field induced in HPSH1 during a typical cold start-up transient. To this end, computational fluid dynamics (CFD) was used to carry out the thermal-fluid analysis of HPSH1. The calculated temperature distributions in the component walls were the primary inputs for the finite element (FEA) model that performed structural analysis. Thermal-structural analysis was initially carried out at full-load steady state condition in order to gain confidence in the CFD and FEA methodologies.

Results of the full-load steady state thermal-fluid analysis were found in agreement with the temperature values measured at specific locations on the outer surfaces of the inlet links and outlet manifold. It was found from the subsequent

structural analysis that peak effective stresses were located at the connecting regions of the components and were well below the allowed stress values.

Higher temperature differences were observed between the thick-walled HPSH1 components during the cold start-up transient as compared to the full-load steady state operating condition. This was because of the rapid temperature changes that occurred, especially in the steam temperature at the HPSH1 entry, and the different rates of heating or cooling for components with different wall thicknesses. Results of the transient thermal-fluid analysis will be used in future to perform structural analysis of the HPSH1.

The developed CFD and FEA models are capable of analyzing various other transients (e.g., hot start-up and shut-down) and determine their influence on the durability of plant components.

ACKNOWLEDGEMENTS

TABLE OF CONTENTS

LIST OF TABLES

LIST OF FIGURES

xiv

xv

CHAPTER 1

INTRODUCTION

1.1 Heat Recovery Steam Generator (HRSG)

The Heat Recovery Steam Generator (HRSG) is an important component of combined cycle power plants (CCPPs). CCPPs utilize gas turbines as well as steam turbines to generate electricity. The HRSG extracts thermal energy from the gas turbine's exhaust (flue) gas to heat feed water and produce steam. This steam is then expanded through a steam turbine. Thus, the performance of the HRSG greatly affects the efficiency of a CCPP.

The HRSG is mainly comprised of multiple series of heat exchange tube banks. Flue gas flows over the tube banks and transfers heat to the steam/water flowing through the tubes. In addition to the tube banks, the HRSG contains carbon monoxide (CO) and selective catalytic reduction (SCR) catalysts for controlling of flue gas emission. The HRSG flue gas is eventually discharged to the atmosphere through a stack.

HRSGs are categorized into two types, based on steam pressure levels [1]:

1. Single-pressure

2. Multi-pressure

A single-pressure HRSG has only one steam drum and generates steam at one pressure level, whereas the multi-pressure HRSG generates steam either at two or three pressure levels. The triple-pressure HRSG generates steam at: high pressure (HP), intermediate pressure (IP), and low pressure (LP), correspond to three

sections of the associated steam turbine. For each pressure level, the HRSG contains superheater, evaporator, and economizer tube banks.

HRSGs are also categorized as either horizontal-tube or vertical-tube, based on the orientation of tube banks, and horizontal or vertical, based on the direction of flue gas flow in the HRSG [1].

A triple-pressure, vertical-tube, horizontal HRSG is analyzed in this work.

1.2 High Pressure Superheater (HPSH) of HRSG

The High Pressure Superheater is comprised of a series of tube banks within the HRSG; it supplies superheated steam at high pressure to the HP section of the steam turbine. Typically, steam is fed to the superheaters from the top of the HP steam drum, which collects steam/water from HP evaporators. The tube banks are placed in the hottest flue gas zone near the HRSG entrance; these are followed by IP and LP tube banks that supplies steam to the IP and LP sections of the steam turbine.

There are two types of HPSH assemblies: multi-row harp assembly and single-row harp assembly. In the multi-row harp assembly, multiple rows of harp tubes are connected to a common header; in the single-row harp assembly, each row of harp tubes is connected to one header.

The work reported in this thesis deals with HPSH1, which is the first HPSH tube bank to encounter the exhaust flue gas.

1.3 Motivation for this work

The high pressure components such as HPSH in HRSGs are designed and built in accordance with standard codes and rules [2] for the base-load operating mode. In recent years, however many plants have been required to operate more in the load-following mode rather than in the base-load mode. This has given rise to thermal fatigue concern for these components. Previous studies have indicated that the interconnected parts of the HPSH, with different wall thickness, are highly susceptible to thermal fatigue damage in the load-following mode [3,4]. The stepped-component-thickness design of the single-row harp assembly does distribute the thermal stress among the components [5]. Nevertheless, during cold start-up, rapid temperature changes occur in the steam and flue gas, this giving rise to large temperature gradients in the thick-walled components of the HPSH such as headers, links, and manifolds. These temperature gradients produce thermal-structural stresses, which result in high cycle fatigue in the parts. Thermal-structural analyses of HPSH components are therefore necessary for transient operating conditions such as cold start-up.

1.4 Literature survey

Researchers and industry personal have been engaged in several studies to analyze the effects of thermal-structural stresses on the HPSH components during transient operations. A summary of some of these works is as follows.

T. B. Brown (1994) of Babcock assessed the effect of thermal transients on the long-term creep-fatigue damage of HRSG components caused by two-shift

operation of CCPPs. Analysis was performed for the superheater outlet header, the part most susceptible to creep-fatigue damage. This part was modeled by the finite element (FEA) method; steam temperature and heat transfer coefficient obtained from thermal design analysis were inputs. The resulting stress distribution pointed the internal crotch of the header and tube as being the peak stress location. Babcock also developed a method of online thermal fatigue monitoring based on FEA methodology [6]. Transfer functions were used to relate the temperature values measured at the outer surface of the outlet header with the thermal stresses induced in the part. These transfer functions were derived before the online monitoring system was installed.

Lu and Wilson (1998) developed an online life monitoring system for two-shifting CCPPs that calculated the thermal stresses and fatigue life usage of selected high pressure, thick-walled components, such as headers and manifold, of the HPSH during transient operations. The recursive identification method and Laplace transfer function were proposed to concurrently calculate the inner surface temperature and the subsequent thermal stress from the measured outer surface temperature of the components. To simplify the calculations, the cylindrical components were treated as a plate insulated on one side (flue gas), with constant convective heat transfer coefficient on other side (steam). The results were compared with accurate solutions, this affirming that these methods were fast, reasonably accurate, and suitable for engineering calculations of online stress monitoring.

Węglowski, Taler, and Duda [2003] studied the transient temperature and stress distributions in thick-walled pressure components of HRSG, such as HPSH and reheater headers, during start-up and shut-down operating conditions. First, time and space dependent temperature distributions in the components were calculated using the inverse heat conduction method [9,10] from measured temperature values taken at the selected points on the outer surface of the components. Next, thermal stresses were determined from the temperature distributions using the FEA method. Measured pressure changes were used to calculate internal pressure-caused stresses. It was concluded that during transient operations the calculated stresses in the HPSH header were considerably smaller than the allowable values.

Bauver, Perrin, and Mastronarde in collaboration with ALSTOM [2003] addressed issues related to the fatigue damage of critical components of large HRSGs during fast start-up operating condition. Superheater outlet headers were identified as the critical components that needed to be analyzed. Insulated thermocouples were installed at selected locations on the outer surfaces of tubes and outlet headers of the superheater to monitor their thermal and mechanical responses during transient operation. Thermal stress analysis of the components was performed using the FEA method. Tube row-to-row temperature difference due to temperature drop in the flue gas along rows, tube-to-header temperature difference due to the differential heating of the components with different wall thickness, and component-to-component temperature difference due to the rapid

internal heating by steam were the main issues addressed in this analysis. It was concluded that stepped component thickness design and single-row harp assembly improve the thermal response of a superheater during fast start-up.

An Electric Power Research Institute (EPRI) report [2009] presented a detailed quantitative approach to analysis of the thermal-mechanical damage on high pressure thick-wall components of HRSG during start-up and shut-down of CCPPs. Two methods, European standard EN12952-3 and FEA, were employed to calculate the permissible number of operating cycles for the high pressure components corresponding to each type of transient. Case studies were performed for two outlet header designs with wall thicknesses of 1.2 inch (thin) and 2.5 inch (thick), respectively. These two designs were analyzed for "as-found" start-up and shut-down operating conditions of the plants. Based on this analysis, the optimum start-up and shut-down operating procedures were developed to minimize fatigue damage in the outlet headers of superheater while maintaining important operating characteristics. It was concluded that the thickness of HPSH headers should be less than 1.2 inch and optimized transient operating procedures are critically important for reducing creep-fatigue damage for thick-wall as well as thin-wall headers.

1.5 Scope of work

The main objective of this work is to address the thermal-structural stress field induced in the HPSH1 of Santan Unit-5B HRSG during a typical cold start-up transient. To this end, Computational Fluid Dynamics (CFD) and Finite

Element Analysis (FEA) models were developed to carry out the thermal-fluid and structural analysis, respectively. ANSYS-Fluent, a commercial CFD tool, was used for the thermal-fluid analysis to obtain the inner and outer surface temperature distributions in the HPSH1 components. The calculated temperature distributions in the component walls were the main inputs for the FEA tool, Siemens NX 7.5, that obtained the thermal-structural stress field in the components. Prior to the transient cold start-up analysis, thermal-structural analysis was performed for the full-load steady state operating condition in order to gain confidence in the CFD and FEA methodologies. The required input data for the full-load steady state and cold start-up transient analyses were procured from the Santan plant personal.

Analysis was carried out for one symmetrical half of the HPSH1 to reduce computational cost.

1.6 Organization of thesis

Detailed descriptions of the Santan Unit-5B HRSG and its HPSH1 are provided in chapter 2.

In chapter 3, the operating conditions for full-load steady state and cold start-up transient analysis are provided. This chapter also contains details pertaining to the modeling of key HRSG internal components. The methodologies for modeling flue gas flow inside the HRSG and steam/water flow through the HPSH1 tube bank as well as the solution approaches for steady state and transient

analysis are included. Thermal and physical properties of the flue gas, steam, and wall material used in CFD simulations are provided in this chapter.

Chapter 4 gives an overview of the CFD tool, ANSYS-Fluent, employed to perform the thermal-fluid analysis of HPSH1. It explains the governing conservation equations, turbulence model, wall function, pressure-velocity coupling, and the boundary conditions used to solve the governing equations.

Chapter 5 presents results and their discussion for the thermal-fluid and structural analysis at full-load steady state operating condition.

Chapter 6 presents results and their discussion for the thermal-fluid analysis during a cold start-up transient. The transient structural analysis, which will be performed at a later date, is also discussed in this chapter.

Finally, chapter 7 offers concluding remarks for the thermal-fluid and structural analysis at full-load steady state, and the thermal-fluid analysis for cold start-up transient operating conditions. Possible future directions for this project are also suggested.

CHAPTER 2

SALT RIVER PROJECT SANTAN GENERATING STATION UNIT-5B

The Salt River Project (SRP) Santan generating station, located in Gilbert, AZ, comprises of five one-on-one, and one two-on-one combine-cycle units generating approximately 1200 MW of electricity (e). This chapter details the HRSG and HPSH1 of unit-5B.

2.1 Unit-5B and its HRSG

Unit-5B is a part of the two-on-one combined-cycle unit of the Santan generating station. The capacity of the unit-5B gas turbine is 150 MWe and that of the steam turbine is 300 MWe. A schematic of the unit is shown in figure 2.1.

A triple-pressure, vertical-tube bank, horizontal HRSG is contained in this unit. The HRSG contains five tube bank modules corresponding to different pressures of steam/water flowing through them. Gas turbine exhaust flue gas flows across the modules in the following order:

Module one: This is the first module to encounter flue gas and consists of the following tube banks:

HPSH1

Reheater 1 (RHTR1)

HPSH2

Module two: The second module consists of the following tube banks:

HPSH3

Reheater 2 (RHTR2)

Generator

Air

Natural
Gas

C T

Combustion
Turbine

HRSG1

HPSH1
RHTR1
HPSH2
Duct Burner
HPSH3
RHTR2
HPSH4
HP EVAP
HP ECON1
IPSH
LPSH
HP ECON2
IP EVAP
HP ECON3
IP ECON
HP ECON4
LP EVAP
PREHEATER

Integral DA

Stack

From HRSG2
From HRSG2

To HRSG2

From HRSG2

HPFW

IPFW

To HRSG2

HP IP LP Generator

Steam Turbine

Condenser

From Cooling
Tower

To Cooling
Tower

Condensate
Pump

High Pressure steam/water path

Reheater steam/water path

Intermediate Pressure steam/water path

Low Pressure steam/water path

Figure 2.1 Santan Unit-5B

HPSH4

High pressure evaporators 1 (HPEVAP1)

High pressure evaporators 2 (HPEVAP2)

Module three: This module consists of the following tube banks:

High pressure economizer 1 (HPECON1)

Intermediate pressure superheater (IPSH)

Low pressure superheater (LPSH)

High pressure economizer 2 (HPECON2)

Intermediate pressure evaporator (IPEVAP)

Module four: The fourth module consists of the following tube banks:

High pressure economizer 3 (HPECON3)

Intermediate pressure economizer (IPECON)

High pressure economizer 4 (HPECON4)

Low pressure evaporator (LPEVAP)

Module five: The last module consists of the following tube banks:

Feed-water preheater 1 (FWHTR1)

Feed-water preheater 2 (FWHTR2)

Feed-water preheater 3 (FWHTR3)

The steam/water flow path for the HP series is as follows: water from the feed-water preheaters flows sequentially through HPECON 4, 3, 2, and 1 and enters the HP steam drum. From the drum bottom, water is supplied to the HP

11

evaporators via a downcomer; and a steam-water mixture is collected back in the drum from the evaporators.

Saturated steam exits from the top of the drum and passes sequentially through the HPSH 4, 3, 2, HP desuperheater, and HPSH1. The HPSH1 supplies steam to the high pressure section of the steam turbine.

The steam/water flow paths from the feed-water preheaters to HP, IP, and LP sections of the steam turbine are shown in figure 2.1. The expanded steam from the exit of the steam turbine HP section is routed sequentially through reheaters 2 and 1, and fed to the IP section of the steam turbine.

In addition to the tube banks, the HRSG contains a perforated plate upstream of module one that helps distribute the flue gas entering the HRSG. A duct burner immediately downstream of module one provides supplemental heat to the flue gas if needed. The SCR and CO catalysts downstream of module two, figure 2.2, control emissions of NO_x and CO into the atmosphere.

1   HRSG inlet
2   Perforated plate
3   Module one (HPSH1, RHTR1, HPSH2)
4   Duct burner
5   Module two
6   SCR and CO catalysts
7   Module three
8   Module four
9   Module five
10 Stack

All dimensions are in ft

Side view of HRSG
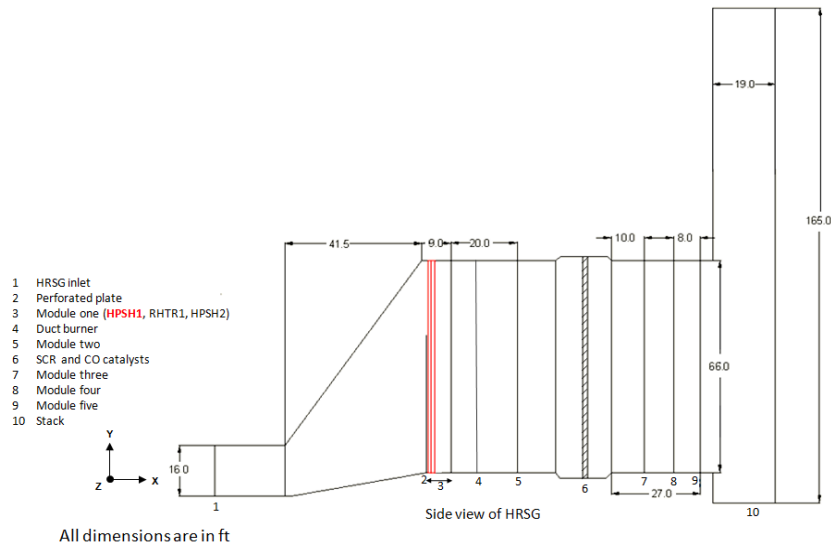
Figure 2.2 HPSH1 position inside the HRSG

12

Main steam inlet

HRSG casing

5

Baffle

Harp tubes

1   HRSG inlet
2   Perforated plate
3   HPSH1

2

Baffle

Y

Flue Gas

6,5

3

Main steam outlet

7,5

Z   X

1

All dimensions are in ft
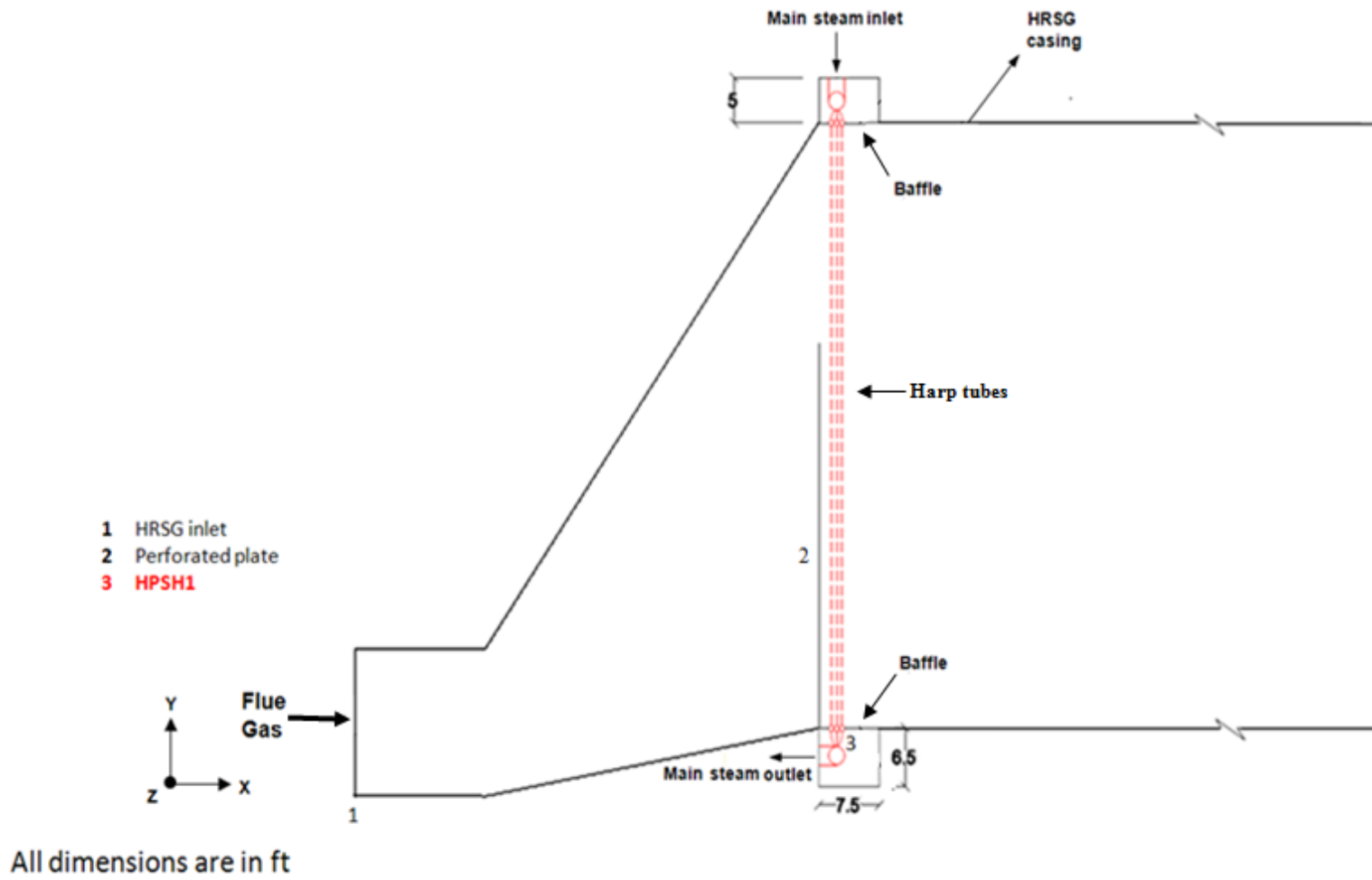
Figure 2.3 The HPSH1 assembly inside the HRSG

2.2 HPSH1 of the HRSG

HPSH1 is the first tube bank to encounter the exhaust flue gas from the turbine. Its position and assembly inside the HRSG are shown in figures 2.2 and 2.3, respectively.

The baffles shown in figure 2.3 are kept at HRSG casing level. The HPSH1 assembly is symmetrical about the x-y plane passing through the middle of the HRSG width in z direction. One symmetrical half of the assembly is shown in figure 2.4.

The components (their numbers given in parenthesis) for one symmetrical half of the HPSH1 assembly, in sequence of steam flow through them are: inlet manifold (1); inlet links (3x3); inlet headers (1x3); harp tubes (42x3); outlet headers (1x3); outlet links (3x3); and outlet manifold (1).

Main steam enters the inlet manifold from the desuperheater and flows into three inlet headers, with three inlet links provided for each header.

From each header, steam is distributed into a row of 42 harp tubes and collected back in the corresponding outlet header.

The steam then flows into the outlet manifold through nine outlet links, with three outlet links provided for each outlet header.

Finally, the steam flows from the outlet manifold to the main steam line, which supplies steam to the steam turbine HP section.

Main steam from desuperheater

Inlet manifold

Inlet links

Inlet headers

Harp tubes

Outlet links

Outlet headers

Main steam to the HP turbine

Outlet manifold
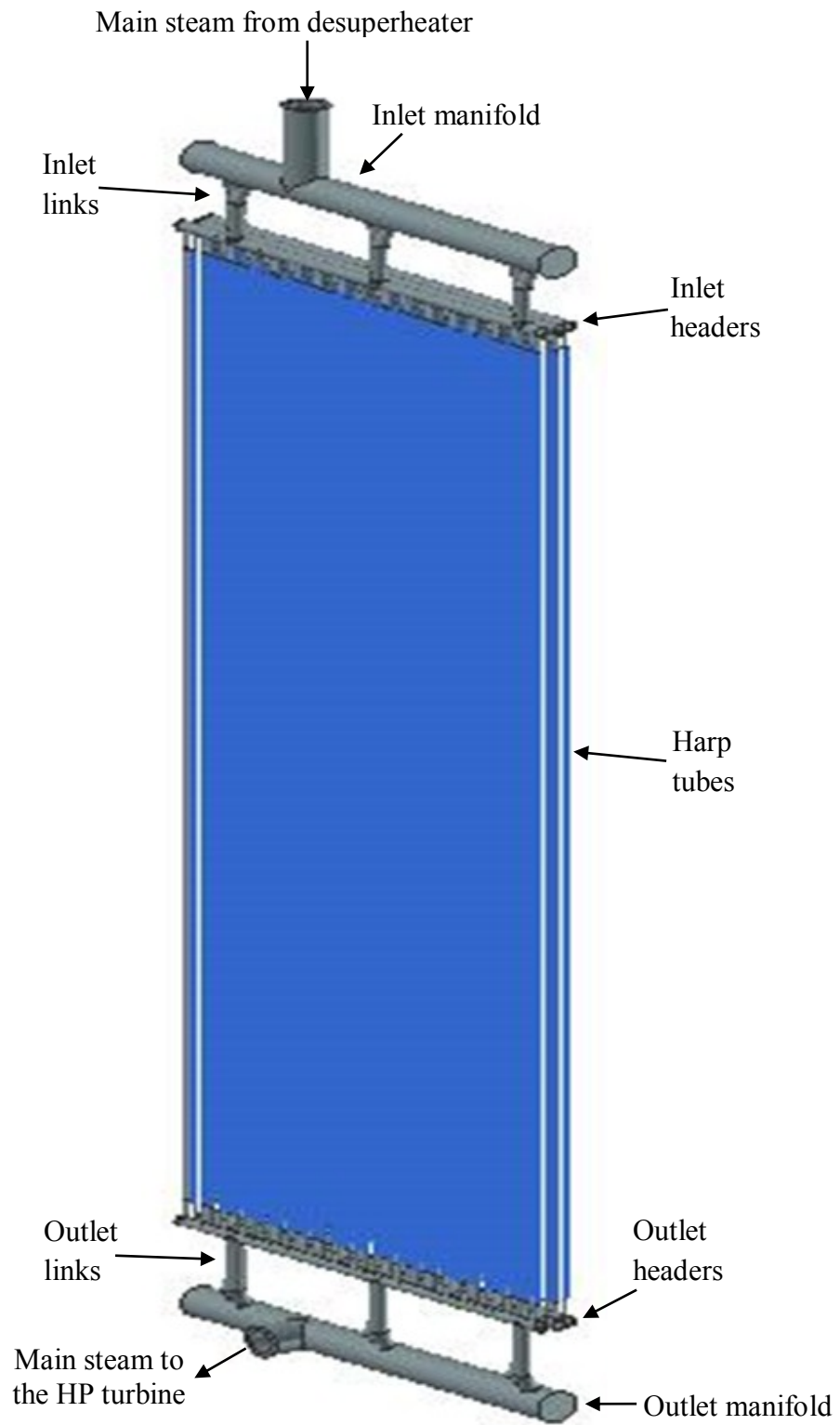
Figure 2.4 One symmetrical half of the HPSH1

CHAPTER 3

FLOW AND HEAT TRANSFER MODELING

3.1 Two operating conditions for Santan Unit-5B

In order to monitor the performance of the unit, several important variables are measured during full-load steady state as well as cold start-up (transient) operating conditions.

The values of variables required for thermal-fluid analysis of the HPSH1 were supplied to us by the Santan generating station personnel.

3.1.1 Full-load steady state

The operation data for the full-load steady state condition of the unit was procured on November 1, 2011. The measured variables are listed in table 3.1.

Flue gas mass flow rate at HRSG inlet	420 kg/s
Flue gas temperature at HRSG inlet	886.5 K
Steam mass flow rate at HPSH1 exit	53.5 kg/s
Steam temperature at HPSH1 inlet	755.5 K
Steam temperature at HPSH1 exit	840.0 K
Steam pressure at HPSH1 exit	7532522 Pa (g)

Table 3.1 Full-load steady state operating conditions

We note here that the steam enters HPSH1 in superheated state.

3.1.2 Cold start-up transient

The data for one cold start-up transient was procured on June 14, 2011 during the interval of 11:15 hrs. to 15:00 hrs. after every 30 seconds. Measured were the values of main steam mass flow rate and pressure at HPSH1 exit, steam temperatures at HPSH1 inlet and exit, and flue gas mass flow rate and temperature at HRSG inlet. These data are shown as time series plots in figures 3.1, 3.2, and 3.3, respectively.
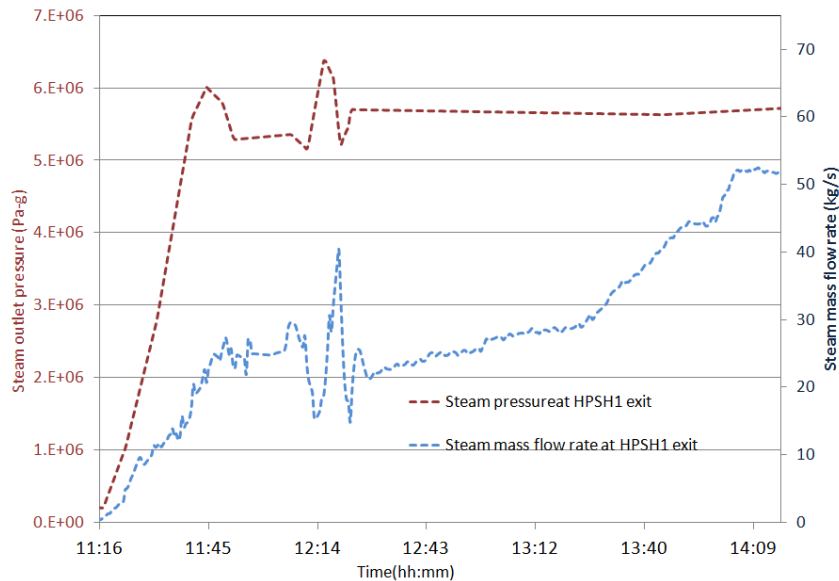
Figure 3.1 Main steam pressure and mass flow rate at HPSH1exit

The steam mass flow rate at HPSH1 exit, shown in figure 3.1, is initially very low – it is less than five percent of the typical steady state value for the time interval 11:16 hr. – 11:23 hr.. The unit reached steady load mode of operation at 14:04 hr. Analysis was performed of the data between 11:23 hr. – 14:09 hr.. During this time interval of 9930 seconds, steam mass flow rate at the HPSH1

17

exit increased from approximately five percent to hundred percent of the eventual steady value.
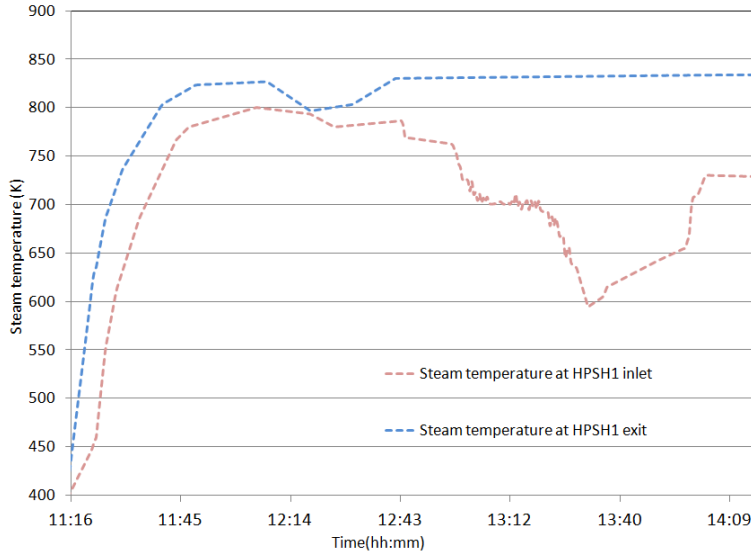
Figure 3.2 Main steam temperatures at HPSH1 inlet and exit
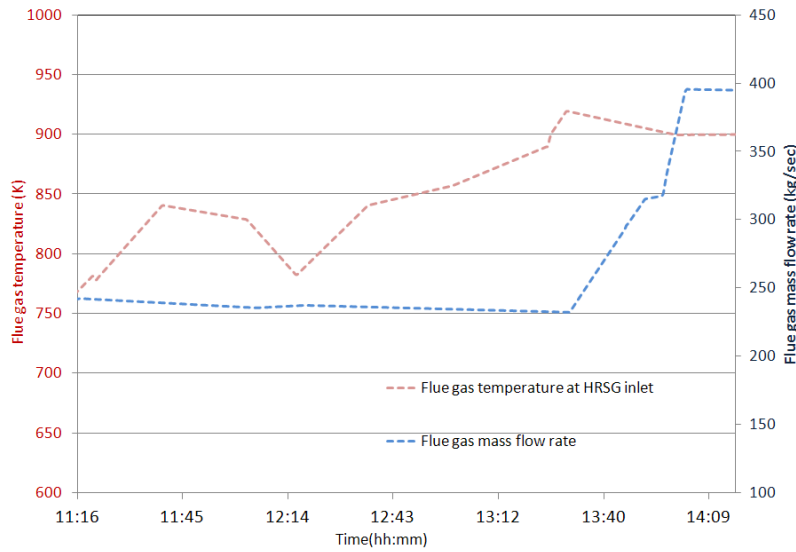
Figure 3.3 Flue gas mass flow rate and temperature at HRSG inlet

It would have been very time-consuming to carry out analysis of the data time series with sharp fluctuations in these. As such, the fluctuations were

18

smoothed using piecewise polynomial functions. The smoothed time series plots corresponding to the figures 3.1, 3.2, and 3.3 are shown in figures 3.4, 3.5, and 3.6, respectively.
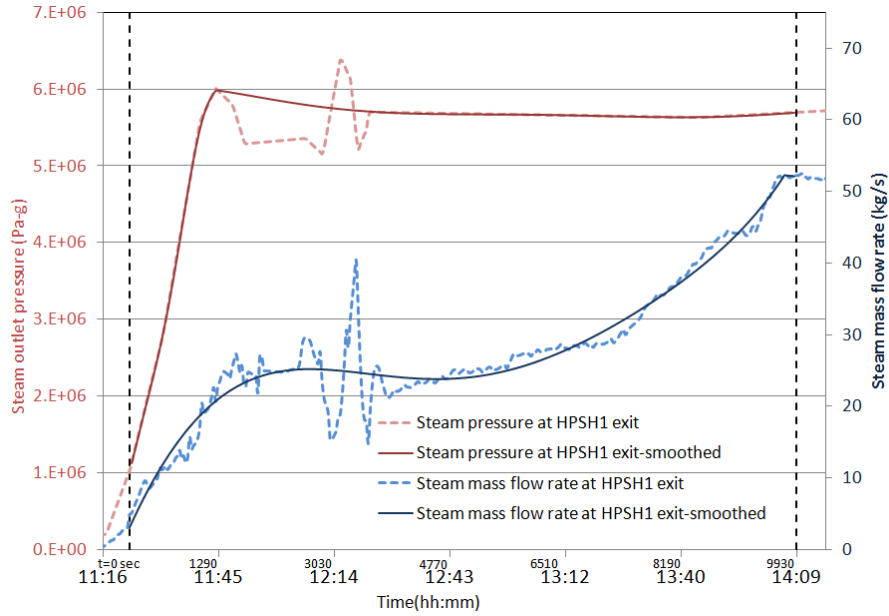
Figure 3.4 Smoothed main steam pressure and mass flow rate at HPSH1exit
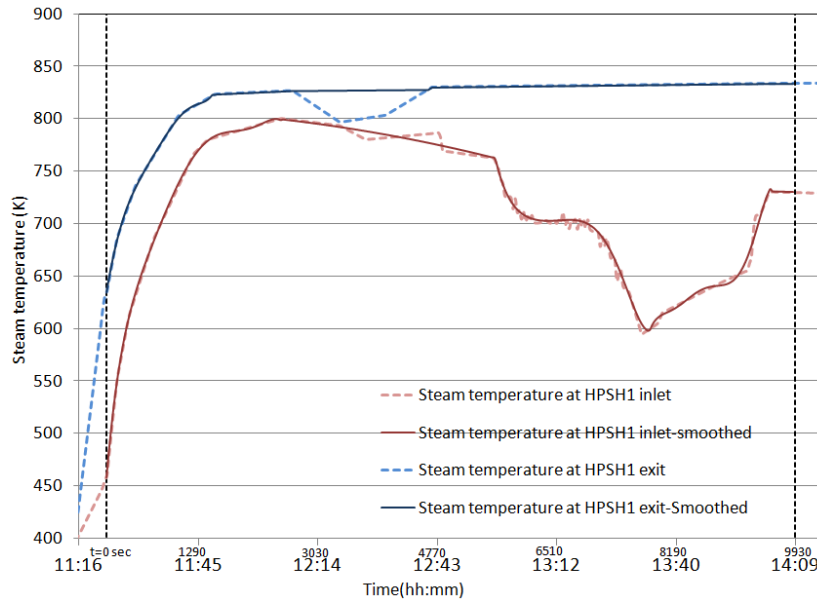
Figure 3.5 Smoothed main steam temperatures at HPSH1 inlet and exit

19
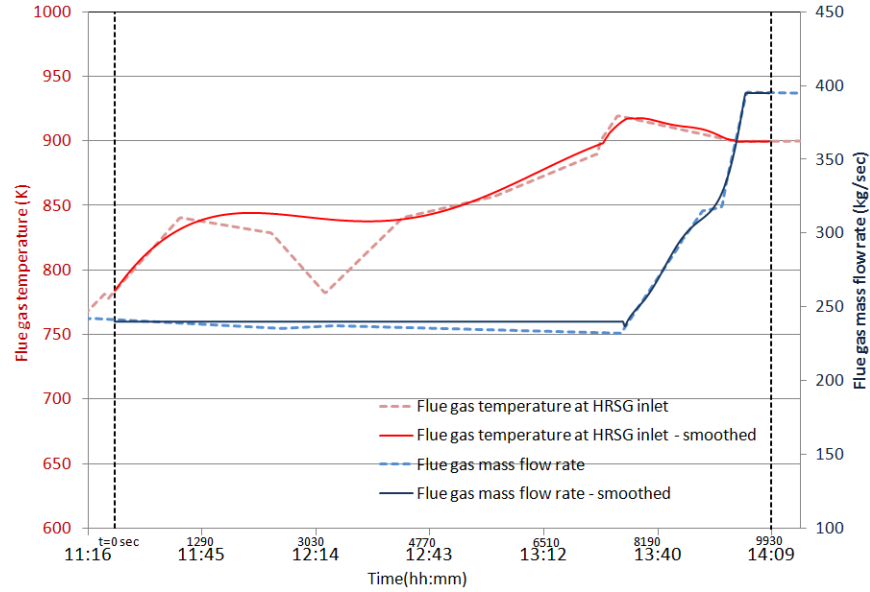
Figure 3.6 Smoothed flue gas mass flow rate and temperature at HRSG inlet

3.2 Modeling of HRSG internal components for flue gas pressure drop calculation

The main components are a perforated plate, the tube banks, and SCR and CO catalysts. Flue gas experiences a pressure drop as it flows through each of these components. The "radiator" feature in ANSYS-Fluent was employed to model the pressure drop across the components.

The radiator is considered as an infinitely thin plane, and the pressure drop through it is proportional to the dynamic head of fluid upstream [12]:

$$\Delta P = K_L * \left(\frac{1}{2} \rho v^2 \right) \tag{1}$$

where, K_L is the loss coefficient for radiator, ρ is density of the fluid, v is the streamwise velocity of fluid upstream of the radiator, and ΔP is the pressure drop across the radiator.

20

The loss coefficient for the radiator is the input parameter for ANSYS-Fluent and calculated from equation (1) using the pressure drop value and the dynamic head of flue gas. To do this, the pressure drops across the components are calculated as follows.

3.2.1 Perforated plate

The perforated plate is considered to be a thick plate because the ratio of plate thickness and perforation diameter is larger than 0.015. The pressure drop across the plate is proportional to the dynamic head of the flue gas upstream of the plate and is calculated as:

$$\Delta P = \zeta * \left(\frac{v^2}{2g}\right) \tag{2}$$

where, ζ is the pressure drop coefficient.
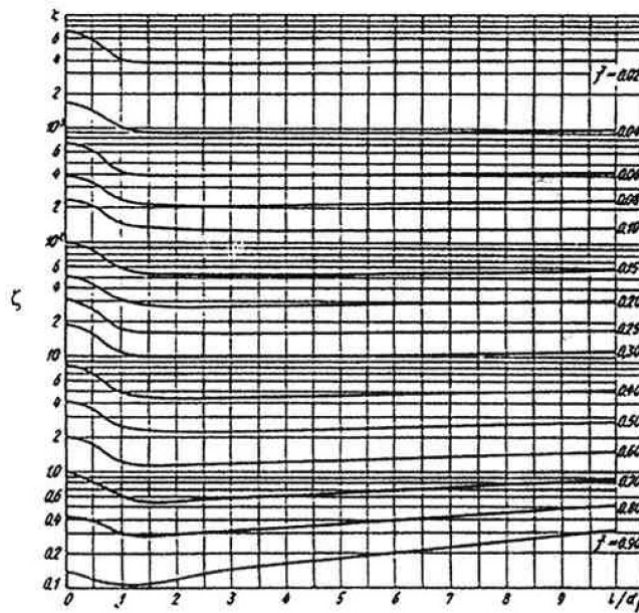
Figure 3.7 Pressure loss coefficient for a thick perforated plate

The pressure drop coefficient is determined from the graph shown in figure 3.7 [13]. It depends on the free area coefficient, $\bar{f}$, and the shape of the perforation edge, l/d_h.

$$\bar{f} = \frac{F_o}{F} \tag{3}$$

where, F_o is the net free area of the plate, and F is the area of the plate.

3.2.2 Tube banks

Flue gas pressure drop across various tube banks are calculated using Extended Surface Corporation of America (ESCOA) method [11]. The pressure drop is a function of the geometry of the tube, the arrangement of tubes in the tube bank, and the Reynolds number of flue gas.

The typical arrangement of a finned tube bank is shown in figure 3.8.
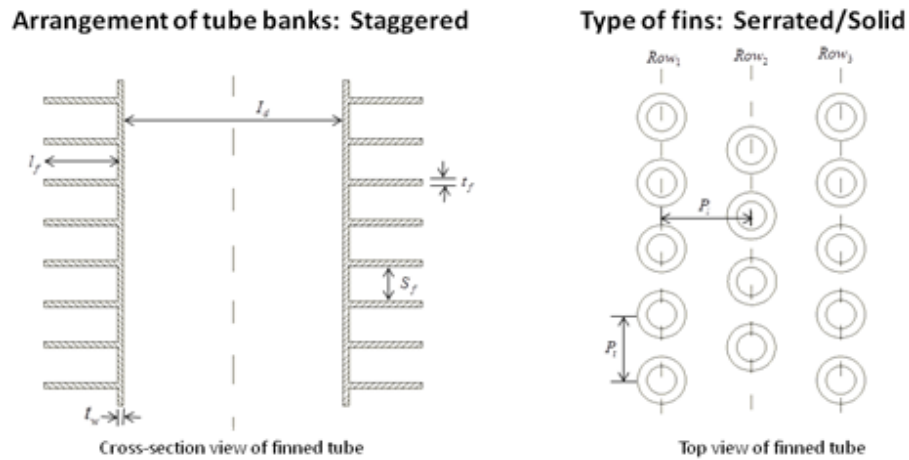
Figure 3.8 Finned tube bank

The pressure drop is calculated as:

$$\Delta P = \left[C_2 C_4 C_6 \left(\frac{f_d}{d_o} \right)^{0.5} \right] * \frac{G_n^2 * Nr}{\rho * 1.083 * 10^9} \tag{4}$$

22

$$G_n = \frac{\dot{m} * p_t}{A_c * A_{min}}$$ (5)

$$A_{min} = [(p_t - t_d) * 1] - \left[t_f * {}^f/_{in} * 2 * l_f \right]$$ (6)

In equation (4), C_2, C_4, and C_6 are Reynolds correction factor, geometry correction factor, and non-equilateral & row correction factor, respectively. They are calculated using Weierman correlations [11] as:

$$C_2 = 0.07 + 8 * Re^{-0.45}$$ (8)

$$C_4 = 0.11 * \left(0.0\,5 * \frac{P_t}{d_o} \right)^{\left(-0.7*\left({}^{l_f}/_{s_f}\right)^{0.23}\right)} \quad \text{(Serrated fins)}$$ (9)

$$C_4 = 0.11 * \left(0.0\,5 * \frac{P_t}{d_o} \right)^{\left(-0.7*\left({}^{l_f}/_{s_f}\right)^{0.20}\right)} \quad \text{(Solid fins)}$$ (10)

$$C_6 = 1.1 + \left(1.8 - 2.1 * e^{-0.15*Nr^2}\right) e^{\left(-2.0*\frac{p_l}{p_t}\right)}$$

$$- \left(0.7 * e^{-0.15*Nr^2}\right) e^{\left(-0.6*\frac{p_l}{p_t}\right)}$$ (11)

$$Re = G_n * \frac{8*d_o}{12*\mu_b}$$ (12)

where,

Nr: number of tube rows $\qquad$ G_n: mass flue gas velocity (lb/hr/ft^2)

m: mass flue gas flow rate (lb/hr) $\quad$ t_w: tube thickness

p_t: transverse pitch $\qquad$ A_c: cross sectional area of HRSG

s_f: fin spacing $\qquad$ f/in: number of fins per inch

l_d: tube inner diameter $\qquad$ A_{min}: net free area for flue gas

d_o: tube outer diameter $\qquad$ Re: Reynolds number

p_l: longitudinal pitch $\qquad$ ρ_{av}: bulk flue gas density

t_f: fin thickness μ_b: bulk viscosity

f_d: fin diameter l_f: fin height

Except for module one, the tube banks are modeled as a single radiator. The HPSH1 tube bank is modeled separately from the other two tube banks (RHTR1 and HPSH2) of module one.

A radiator is placed at the front plane of each modeled tube bank.

3.2.3 SCR and CO catalysts

The SCR and CO catalysts are modeled together as one radiator. The radiator is placed at the front plane of the SCR catalyst.

The flue gas pressure drop across the catalysts is known to be 1.5 inches of water from the plant measurements corresponding to the full-load steady state flue gas mass flow rate of 420 kg/s. This pressure drop is used to calculate the radiator loss coefficient.

3.3 Velocity and pressure distribution model of flue gas flow in HRSG

Flue gas velocity and pressure distributions in the HPSH1 region are required inputs for the thermal-fluid analysis. The modeling of flue gas flow in the HRSG is done in two parts: the stack and the HRSG.

3.3.1 The stack model

This model establishes the pressure value at the inlet to the HRSG stack, the inlet y-z plane being the outlet plane of the HRSG. The stack is 19 ft. in diameter and of 165 ft. height, figure 3.9. The outlet of the stack is open to the

atmosphere. Hence, the flue gas pressure at this outlet plane is the atmospheric pressure, i.e., 0 Pa (gage) for both steady state and transient conditions.
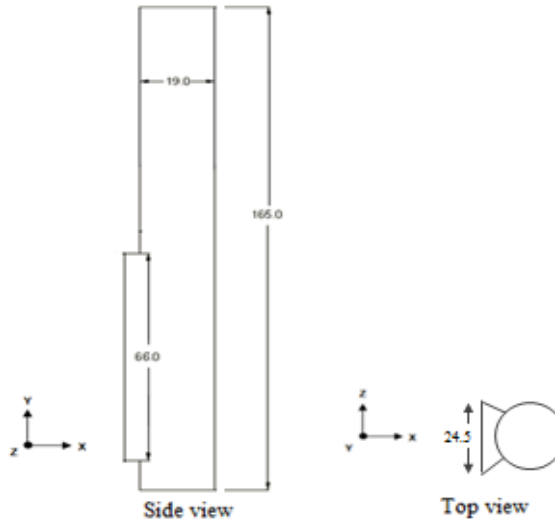
Figure 3.9 The stack model

3.3.2 The HRSG model

The inlet plane of the HRSG model is the outlet plane for exhaust flue gas from the gas turbine, and the outlet plane of the model is the inlet plane of the stack model. The HRSG model geometry is shown in figure 3.10.

Mesh for the HRSG model with tetrahedral and hexahedral elements is shown in figure 3.11.

The flue gas mass flow rate at the inlet y-z plane and the pressure distribution at the outlet y-z plane are used as the inlet boundary condition and the outlet boundary condition, respectively. The pressure distribution at the HRSG outlet plane is obtained from the stack model.

25
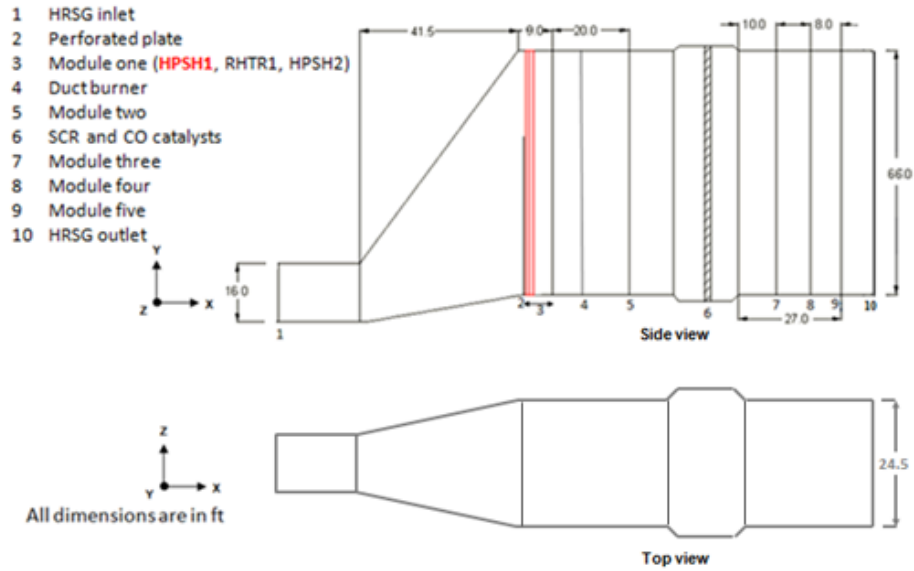
Figure 3.10 The HRSG model geometry

Tetrahedral
elements

Hexahedral
elements
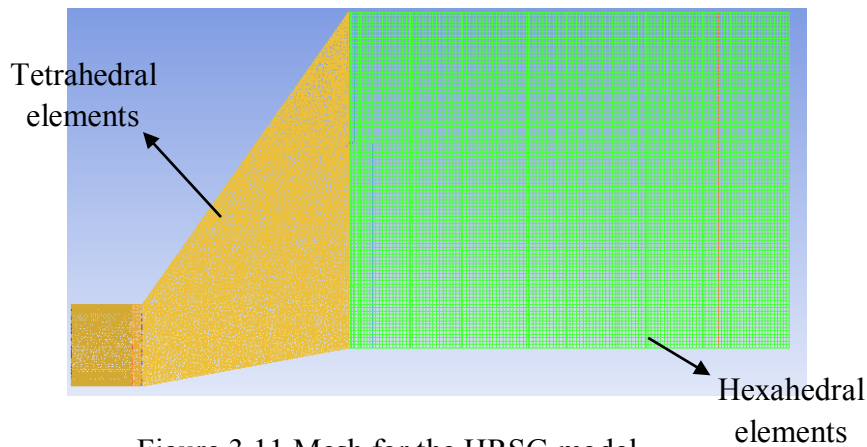
Figure 3.11 Mesh for the HRSG model

3.4 Velocity, pressure, and temperature distribution model of steam and flue gas flows in HPSH1

The thermal-fluid analysis is performed for one symmetrical half of the HPSH1 assembly to reduce computational cost. Due to the still-large computational domain, the HPSH1 assembly is modeled in three separate sections: inlet section, harp tube section, and outlet section, figure 3.12. The portions of the outlet section, $y = 0$ ft. $- 0.93$ ft., and the inlet section, $y = 65.2$ ft.

26

– 66.0 ft., inside the HRSG casing are also shown in figure 3.12. These sections are coupled with the mass flow rate, temperature, and pressure of steam. This means steam mass flow rate, temperature, and pressure at the exit of the inlet section is the inlet mass flow rate, temperature, and pressure for the harp tube section, and steam mass flow rate, temperature, and pressure at the exit of the harp tube section is the inlet mass flow rate, temperature and pressure for the outlet section.
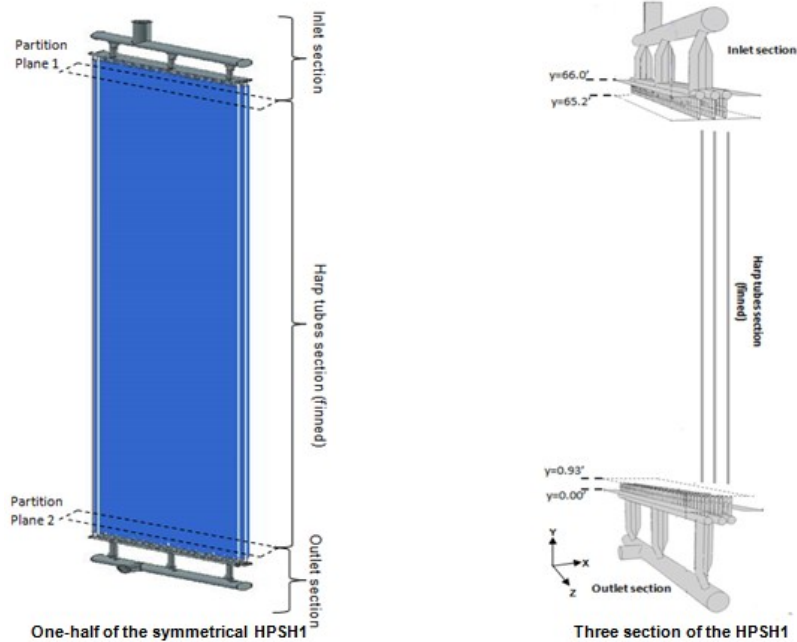
Figure 3.12 Three sections of one half of the HPSH1

3.4.1 Steam and flue gas flow modeling for the inlet section

The inlet section consists of the inlet manifold, the links, the headers, and the unfinned portion of the harp tubes as shown in figure 3.13. Baffles for this section are situated at the level of the headers center line.

The inlet section model has fluid domains for steam and flue gas, and solid domain for P91 wall material.

The main steam enters the inlet manifold and exits from the unfinned harp tubes, whereas the flue gas enters through an y-z plane upstream of the tubes, and exits from an y-z plane downstream of the tubes, figure 3.13. The arrangement of the section is shown in figure 3.14.
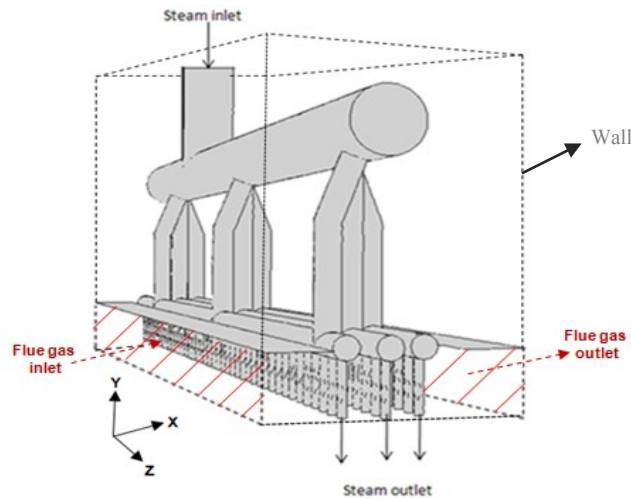
Figure 3.13 Inlet section of HPSH1

The meshed region and number of mesh cells for the inlet section model are provided in figure 3.15 and table 3.2, respectively. The cross-section of the meshed walls of inlet manifold, links, and headers are shown in figure 3.16.

Solution approaches for the inlet section are explained in section 3.5. Velocity, pressure, and temperature distributions in main steam and flue gas are solved for the inlet section. Convective heat transfer on steam and flue gas sides, and conductive heat transfer through component walls are also solved for the section.
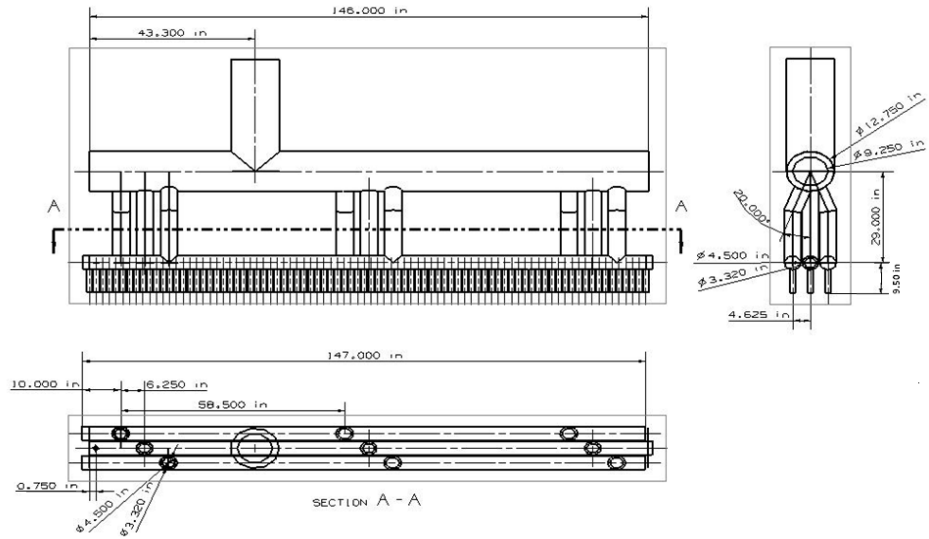
Figure 3.14 Arrangement of the inlet section
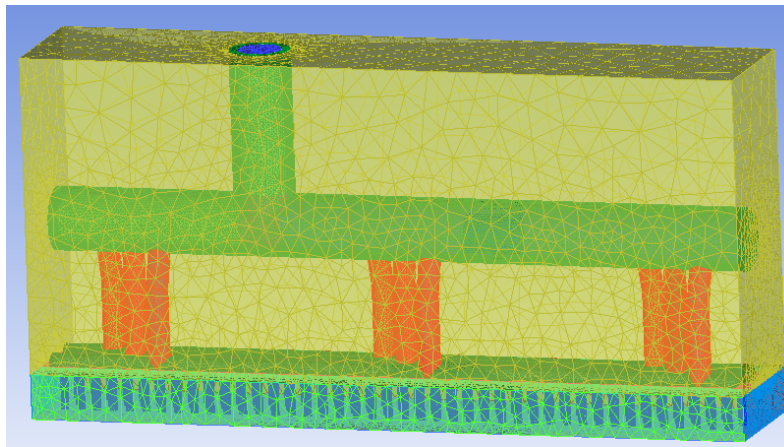
Figure 3.15 Meshed region of the inlet section

Domain	Number of cells
Steam	533643
Flue gas	687448
P-91	1388125
Total	2609216

Table 3.2 Number of mesh cells for the inlet section

29
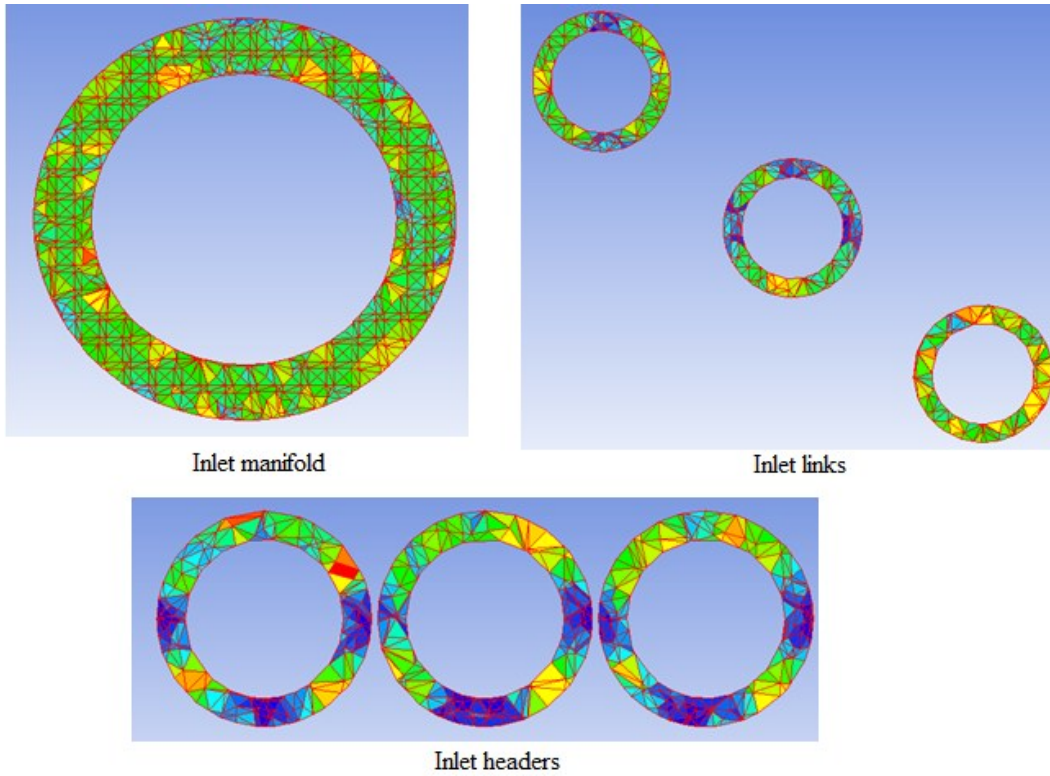
Figure 3.16 Cross-section of the meshed wall for the inlet section

3.4.2 Steam flow modeling for the harp tube section

The harp tube section consists of finned lengths of harp tubes. The arrangement associated and dimensions of the tubes are shown in figure 3.17.
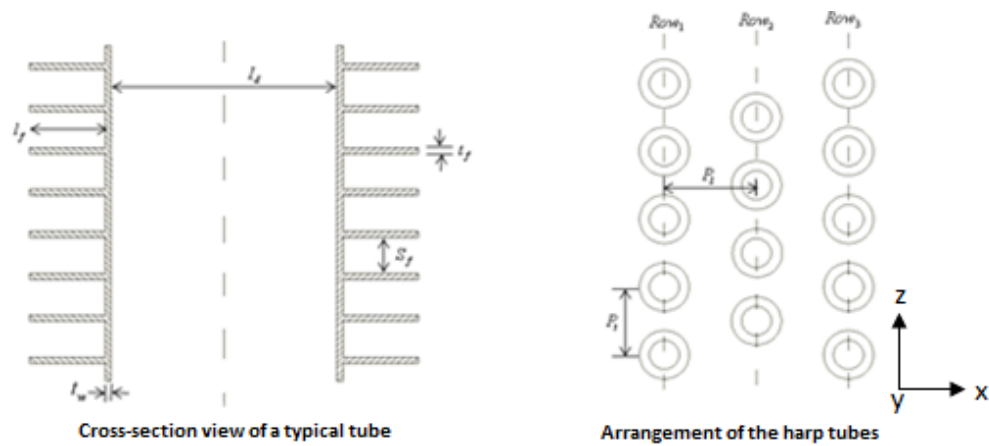
Figure 3.17 Finned HPSH1 harp tubes

30

Number of rows: 3

Number of tubes: 3 x 42

Arrangement: staggered

Type of fins: solid/helical

Longitudinal pitch (P_l): 4.625in

Transverse pitch (P_t): 3.500in

Outside diameter: 1.500in

Tube thickness (t_w): 0.174in

Length of the tubes: 64.28 ft

Fin spacing (s_f): 0.235in

Fin thickness (t_f): 0.05in

Fin length (l_f): 0.5in

The harp tube section has a fluid domain for steam and solid domain for the P91 wall material. The meshed region and cell numbers for a typical tube are shown in figure 3.18 and table 3.3, respectively.
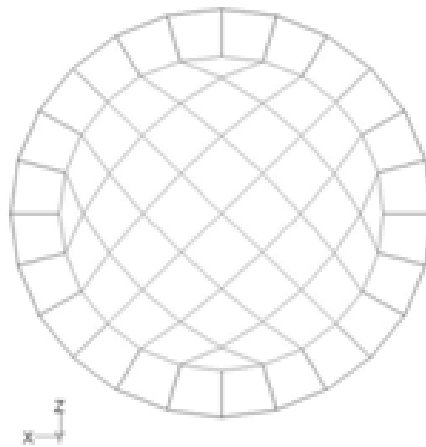
Figure 3.18 Top view of a typical meshed harp tube

Domain	Number of cells
Steam	189,612
P-91 wall	126,408
Total	316,020

Table 3.3 Number of mesh cells for a typical tube

Velocity, pressure, and temperature distributions of steam for the section are solved. Also solved are the convective heat transfer on the steam side and conductive heat transfer through the tube wall. The convective heat transfer on the flue gas side is calculated using heat transfer coefficient and flue gas temperature at the outside surface of the wall.

The finned harp tubes are modeled as bare (i.e., unfinned) tubes and an 'equivalent' heat transfer coefficient is calculated for the outside surface of the bare tube bank such that equal heat transfer occurs for the bare and finned tube banks as given by equation (13).

$$h_f A_{eff}(T_o - T_b) \qquad = \qquad h_{equ} A_b(T_o - T_b) \qquad (13)$$

(heat transfer for actual finned tube bank)   (heat transfer for 'equivalent' bare tube bank)

where,

h_f: outside heat transfer coefficient for finned tube bank

h_{equ}: equivalent outside heat transfer coefficient for the 'equivalent' bare tube bank

A_{eff}: effective outside area for finned tube bank

A_b: outside area for the 'equivalent' bare tube bank

T_o: outside flue gas temperature

T_b: outside surface temperature for the tube bank

The calculations for the equivalent outside heat transfer coefficient and the outside flue gas temperature for the bare tube bank are explained next.

3.4.2.1 Outside heat transfer coefficient for harp tube bank

The equivalent outside heat transfer coefficient for the 'equivalent' bare tube bank is calculated using equation (14), which is derived from the equation (13).

$$h_{equ} = \frac{h_f A_{eff}}{A_b} \tag{14}$$

The outside heat transfer coefficient for the finned harp tube bank is calculated using Wierman correlation [11].

$$\frac{h_f * Pr^{2/3}}{c_p * G_n} = C_1 * C_3 * C_5 * \sqrt{\frac{d_f}{d_o}} * \sqrt[4]{\frac{T_o}{T_f}} \tag{15}$$

C_1, C_3, and C_5 are determined as:

$$C_1 = 0.25 * Re^{-0.35} \tag{16}$$

$$C_3 = 0.35 + 0.65 * e^{\frac{-0.25 * l_f}{s_f}} \tag{17}$$

$$C_5 = 0.7 + \left(0.7 - 0.8 * e^{-0.15 * Nr^2}\right) * e^{\frac{p_l}{p_t}} \tag{18}$$

The effective area for the finned tube bank is calculated as:

$$A_{eff} = \eta_f A_{fins} + A_{base} \tag{19}$$

$$\eta_f = x * (0.9 + 0.1 * x) \tag{20}$$

$$x = \frac{\tanh(m * B)}{m * B} \tag{21}$$

$$B = l_f + \frac{t_f}{2} \tag{22}$$

$$m = \sqrt{\frac{2 * h_o}{k * t_f}} \tag{23}$$

where,

l_f = fin length S_f = fin spacing

t_f = fin thickness k = thermal conductivity of fin

Pr = Prandlt number for flue gas d_f = fin diameter

d_o = tube outside diameter d_i = tube inside diameter

A_{fin} = fins area for finned tube A_{base} = base area for finned tube

T_o = flue gas temperature T_f = average fin temperature

The equivalent outside heat transfer coefficient for the 'equivalent' bare tube bank is calculated for a range of flue gas velocities to accommodate non-uniformity in the flue gas velocity upstream of the tube bank. The plots of h_{equ} and h_f vs. the flue gas velocity are shown in figure 3.19.

A polynomial function of flue gas velocity, which is function of height (y), is used to define the equivalent outside heat transfer coefficient in the harp tube model.
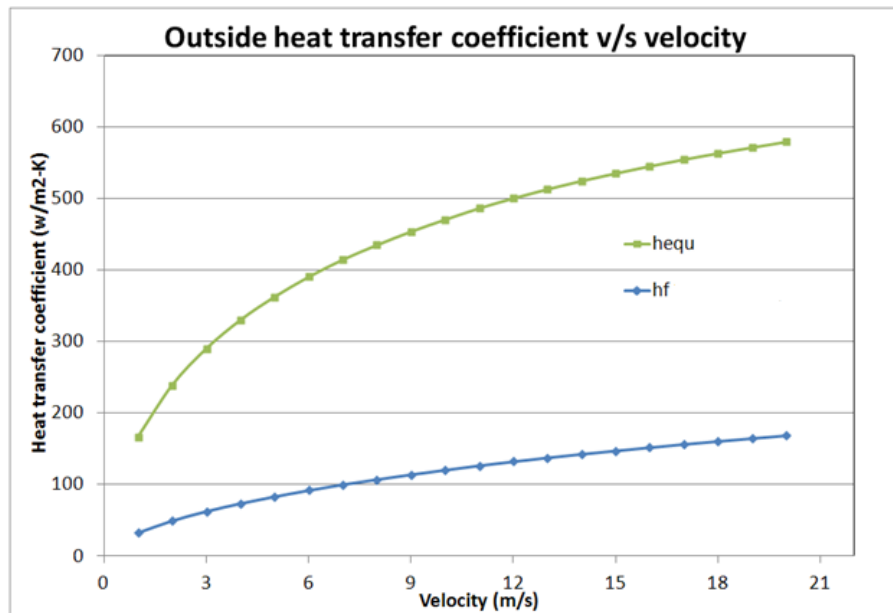
Figure 3.19 Outside heat transfer coefficient for harp tube bank

3.4.2.2 Flue gas temperature for harp tubes

Flue gas temperature at the HRSG inlet is measured for full-load steady state and cold start-up (transient) operating conditions. The outside flue gas temperature for the harp tubes is determined with two approaches and detailed in the following.

3.4.2.2.1 Uniform along the tube length

In this approach, flue gas temperature is assumed to be uniform along the harp tube length (y-axis) as well as in the transverse direction (z-axis). That there is a gradual temperature drop in the flue gas as it progresses over the harp tube rows is taken into account.

Flue gas temperature upstream of tube row 1 is assumed to be equal to its temperature at the HRSG inlet as the HPSH1 is the first tube bank to encounter the flue gas.

The flue gas temperature downstream of row 3 is calculated using heat balance between flue gas and steam as given in equation (24). The heat balance assumes that steam temperatures at the inlet and the outlet of harp tube section are, respectively, equal to main steam temperatures at the inlet and the exit of HPSH1. This assumption will be justified later in the results sections 5.2 and 6.2.

$$\left(m * c_p * \Delta T\right)_{flue} = (m * \Delta h)_{steam} \qquad (24)$$

where,

m = mass flow rate c_p = specific heat capacity of the flue gas

Δh = steam enthalpy difference between the inlet and exit of HPSH1

$\Delta T = T_1 - T_2$

T_1 = flue gas temperature upstream of row 1 tubes

T_2 = flue gas temperature downstream of row 3 tubes
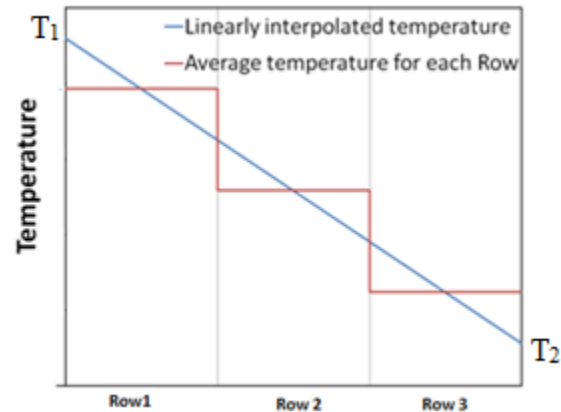
Figure 3.20 Uniform flue gas temperature along the tube length

Flue gas temperature downstream of row 1 and row 2 are calculated by linear interpolation between T_1 and T_2, figure 3.20. The temperature for each row is calculated by taking the average of upstream and downstream temperature of that row.

3.4.2.2.2 Non-uniform along tube length

In this approach, the flue gas temperature distribution is calculated using the Fluent NTU macro model. This model is used only for the full-load steady state condition.

The Fluent NTU macro model solves heat transfer through a series of tube banks (heat exchanger - HX) for non-uniform velocity profile of the primary fluid flowing outside the HX.

The HX is treated as a fluid zone and is sized to its actual physical dimensions. The heat transfer from the auxiliary fluid, flowing inside the HX, to the primary fluid is a source term in the energy equation of the primary fluid.

In the present case, the harp tube bank is the HX, flue gas is the primary fluid, and steam is the auxiliary fluid. The HX is subdivided into macroscopic cells, macros, along the steam path as shown in figure 3.21.

Each macro has a different heat transfer rate based on the mass flow rates and the temperatures of the primary and auxiliary fluids at the inlet of each macro [12].

The chart shown in figure 3.22, explains the methodology used to calculate the non-uniform flue gas temperature from a series of the uniform temperature results using the NTU macro model.
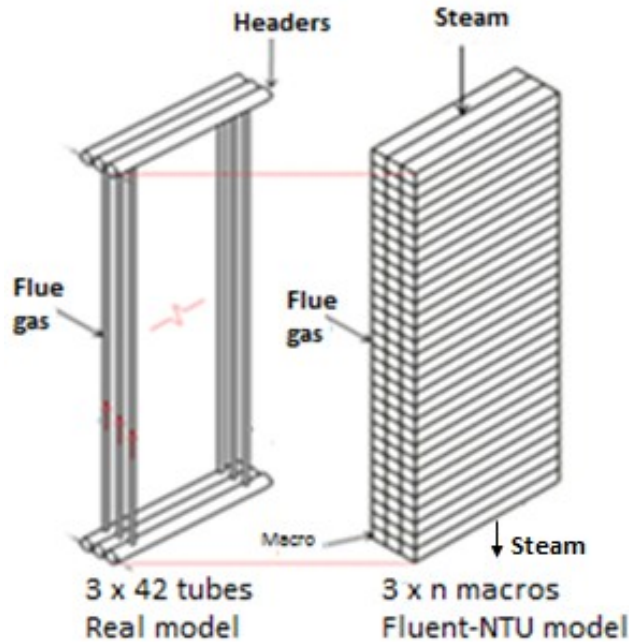
Figure 3.21 NTU macro model for finned tube bank
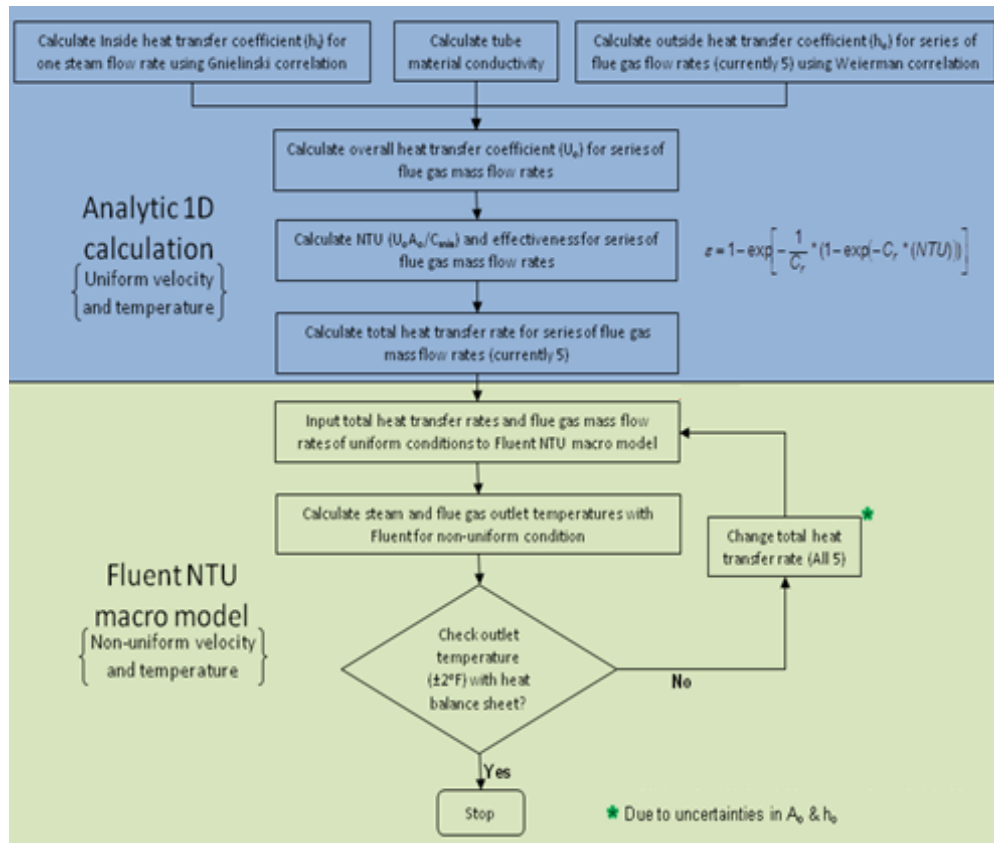
Figure 3.22 Methodology chart to solve for heat transfer through the tube bank

First, one-dimensional analytic calculations are performed for uniform velocity temperature flue gas to obtain an input data set for the Fluent NTU model.

The overall heat transfer coefficient, U_o, is calculated for a series of flue gas mass flow rates and for a single steam mass flow rate by using equation (25) [11]. The inside heat transfer coefficient is calculated using the Gnielinski correlation [14], equation (27); the thermal conductivity of tube material is calculated from equation (26) [15]; and the outside heat transfer coefficient is calculated using the Weierman correlation, equation (15).

38

$$U_0 = \frac{1}{\left(\frac{1}{h_f}+R_{fo}\right)*\frac{A_o}{\eta_f A_{fin}+A_{base}}+\left(\frac{t_w A_o}{k_w A_i}\right)+\left(\frac{1}{h_i}+R_{fi}\right)*\frac{A_o}{A_i}} \tag{25}$$

where,

U_o = overall heat transfer coefficient

h_f = outside heat transfer coefficient

R_{fo} = outside fouling factor η_f = fin efficiency

t_w = tube wall thickness $A_o = A_{fin} + A_{base}$

k_w = tube wall thermal conductivity A_i = inside tube surface area

h_i = inside heat transfer coefficient R_{fi} = inside fouling resistance

$$k_w = -10^{-5} * C^2 + 0.017 * C + 25.535 \tag{26}$$

C = temperature in °C

$$Nu = \frac{h_i*d_i}{k} = \frac{\frac{f}{8}*(Re-1000)*Pr}{1+12.7*\left(\sqrt{\frac{f}{8}}\right)*(Pr^{2/3}-1)} \tag{27}$$

$$f = \frac{1}{(1.82*\log Re-1.64)^2} \tag{28}$$

$$Re = \frac{G_n*d_i}{\mu} \tag{29}$$

Also,

k = avg. thermal conductivity of the steam d_i = tube inside diameter

Pr = avg. Prandlt number for steam

G_n = steam mass flow rate per tube cross-sectional area

μ = avg. dynamic viscosity of steam f = friction factor

The total heat transfer rate for the HX is calculated using equations (31), (32), and (33) as follows:

Number of transfer units for HX (NTU) $= \dfrac{U_o * A_o}{C_{min}}$ (31)

Effectiveness of HX, $\varepsilon = 1 - \exp\left[-\dfrac{1}{C_r} * \left(1 - \exp(-C_r * NTU)\right)\right]$ (32)

Total heat transfer rate, $\dot{Q} = \varepsilon * C_{min} * \left(T_{h,in} - T_{c,in}\right)$ (33)

where,

C_{min} = minimum heat capacity among primary and auxiliary fluids

C_{max} = maximum heat capacity among primary and auxiliary fluids

C_r = heat capacity ratio i.e. the ratio of C_{min} and C_{max}

$T_{h,in}$= primary fluid temperature upstream HX

$T_{c,in}$ = auxiliary fluid inlet temperature for HX

Subsequently, the calculated heat transfer rates for a series of flue gas mass flow rates at uniform velocity and temperature of the gas are provided as inputs to the Fluent NTU model.

The mass flow rate of steam along with thermal properties are also provided as inputs to the Fluent NTU model. The steps involved in the working of the NTU macro model are described in the flow chart shown in figure 3.23 [12].
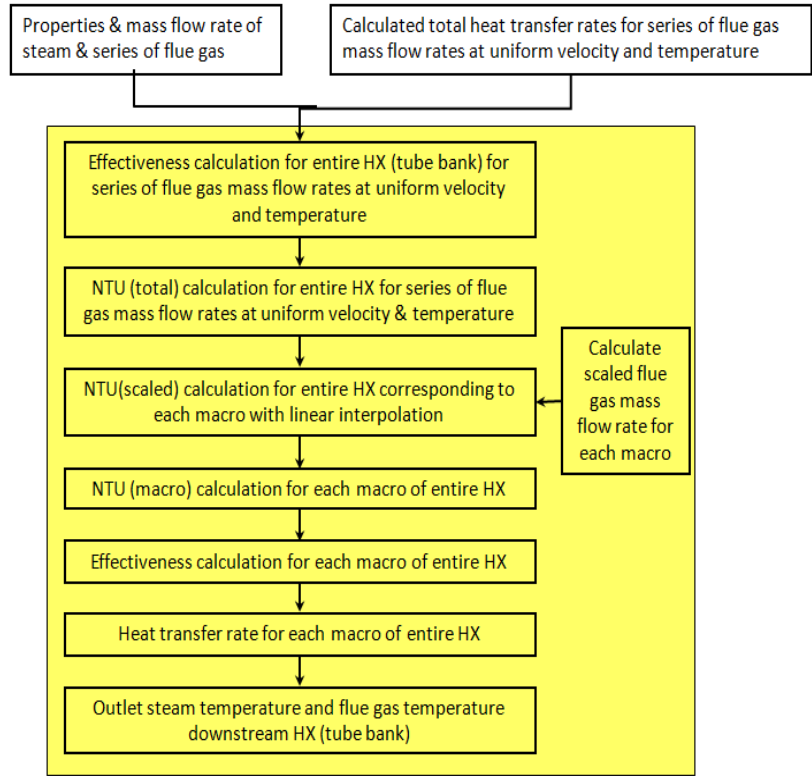
Figure 3.23 Steps involved in the NTU macro model

The effectiveness of the entire HX is computed for the aforementioned series of flue gas mass flow rates using equation (33). The calculated effectiveness values are used to generate a table of the NTU (total) using equation (34).

$$\varepsilon = 1 - \exp\left[-\frac{1}{C_r} * NTU^{0.22} * \left(1 - e^{-C_r NTU^{0.78}}\right)\right] \qquad (34)$$

The NTU (scaled) is calculated for each macro of the HX using the NTU (total) and scaled flue gas mass flow rate corresponding to the particular macro. The NTU (macro) for each macro is calculated from the NTU (scaled).

The equations for calculating NTU (macro) from NTU (scaled) are proprietary to ANSYS-Fluent [12]. The effectiveness and heat transfer rate for

41

each macro are determined from NTU (macro) using equations (32) and (33), respectively [12].

Once the heat transfer rate for the macro is obtained, the flue gas and steam temperatures at the macro exits are determined from equation (35).

$$\Delta T = \frac{\dot{Q}}{\dot{m}\, c_p} \qquad\qquad (35)$$

The flue gas and steam outlet temperatures of a macro are the inlet temperatures for the next macro; heat transfer rate for next macro is calculated in a similar manner. The total heat transfer rate for the HX is the sum of the heat transfer rates of the macros comprising the HX.

The exit steam temperature calculated from the NTU model is compared with the measured HPSH1 main steam exit temperature. If the two temperature values are not within ±1 K then the values of heat transfer rates for the aforementioned series of mass flow rates are changed manually to match them. The values are increased if the calculated steam temperature is lower than the measured one and vice versa. The manual changes in the heat transfer rates are made because of the uncertainties in the exact geometrical details of the harp tubes as well as the correlations used to calculate the heat transfer rates.

3.4.3 Steam and flue gas flow modeling for the outlet section

The outlet section model consists of the outlet manifold, the links, the headers, and unfinned part of the harp tubes as shown in figure 3.24. Baffles for this section are located just above the headers.

There are fluid domains for steam and flue gas, and solid domain for P91 wall material. Main steam enters the unfinned harp tubes and exits from the outlet manifold; the flue gas enters through an y-z plane upstream of the tubes, and exits from an y-z plane downstream of the tubes, figure 3.24. Arrangement of the section is shown in figure 3.25.
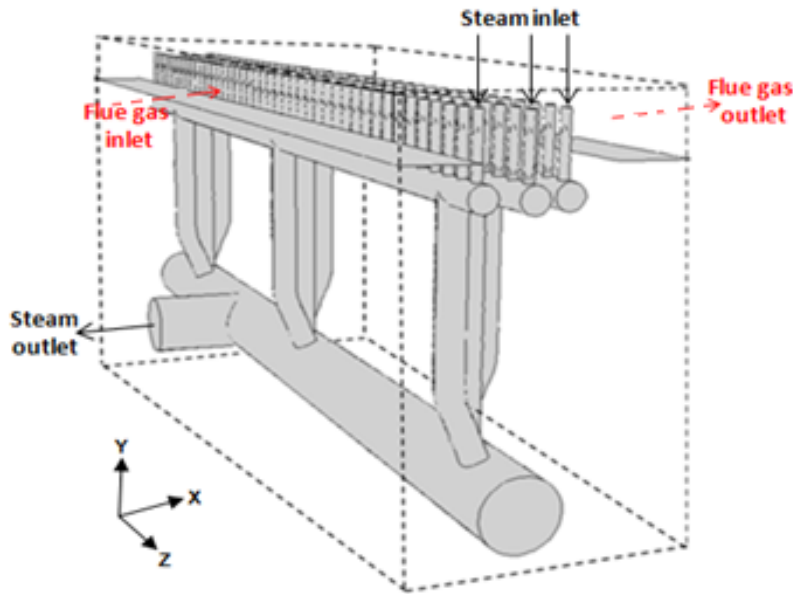
Figure 3.24 Outlet section of HPSH1

The meshed region and number of mesh cells for the outlet section are provided in figure 3.26 and table 3.4, respectively. The cross-section of the meshed walls of inlet manifold, links, and headers are shown in figure 3.27.

Solution approaches for the outlet section are explained in section 3.5. Velocity, pressure, and temperature distributions in main steam and flue gas are solved for the section. Convective heat transfer on steam and flue gas sides, and conductive heat transfer through component walls are also solved for the section.
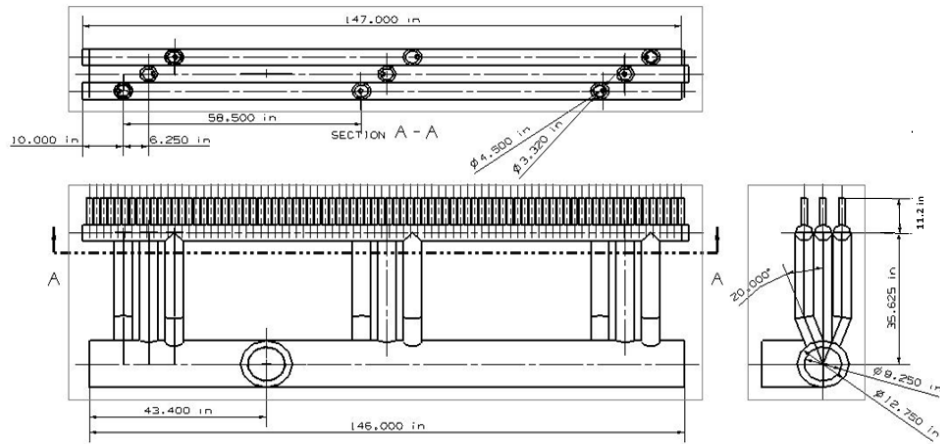
Figure 3.25 Arrangement of the outlet section
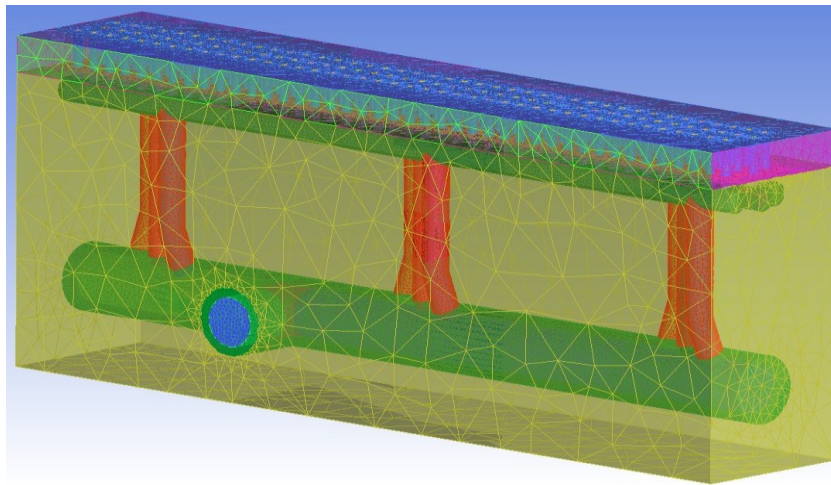
Figure 3.26 Meshed region of the outlet section

Domain	Number of cells
Steam	383,409
Flue gas	707,091
P-91	567,153
Total	1,657,673

Table 3.4 Number of mesh cells for the outlet section

44
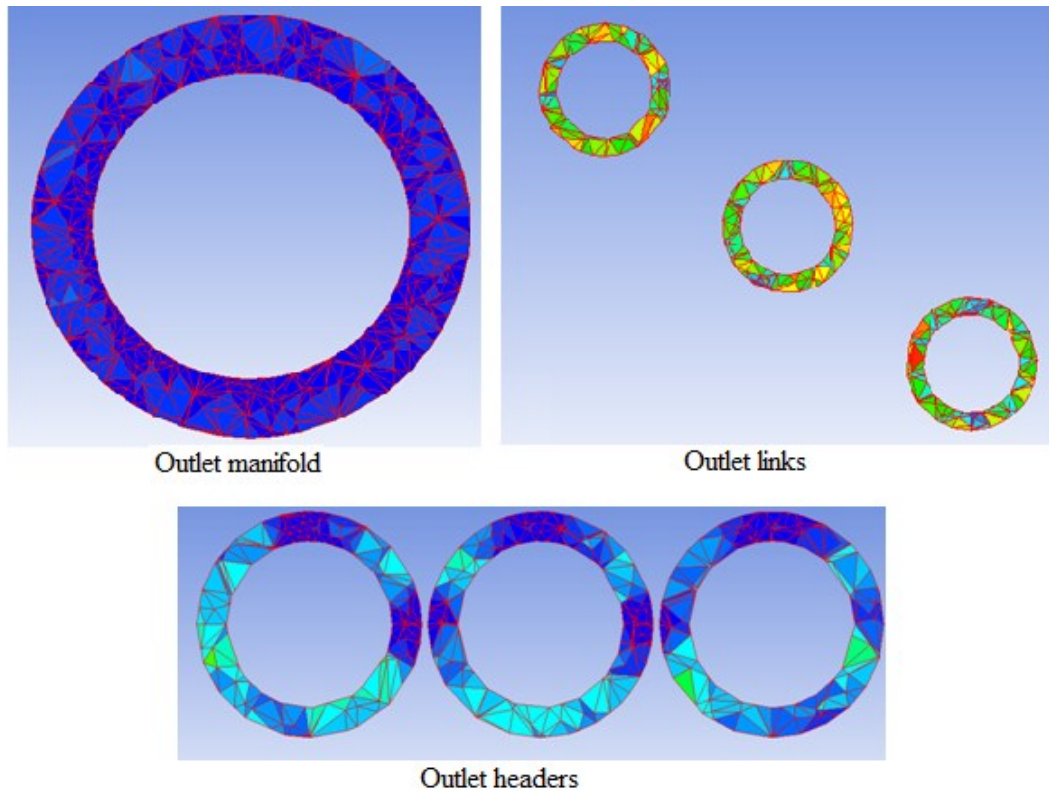
Figure 3.27Cross-section of the wall mesh for the outlet section

3.5 Solution approaches for the HPSH1 models

Two different approaches were taken to solve the HPSH1 models for full-load steady state and cold start up transient analyses.

3.6.1 Steady states

Steam temperature at the HPSH1 inlet, and pressure (P_o) and mass flow rate at the HPSH1 exit are measured at the plant for steady state operating conditions. Steam mass flow rates at the HPSH1 inlet and the exit are equal at steady state.

The inlet section is solved first with steam mass flow rate and temperature as the inlet boundary condition, and P_o as the outlet pressure boundary condition

45

for the steam domain of the section. Note that the actual outlet pressure for the inlet section is expected to be somewhat higher than P_o.

For the flue gas domain of the section, uniform velocity at the inlet plane and uniform pressure at the outlet plane, obtained from the full HRSG model solution, are used, respectively, as the inlet and the outlet boundary conditions. Flue gas temperature at the HRSG inlet is used for the inlet boundary condition.

Results are obtained for velocity, pressure, and temperature distributions of steam and flue gas for the section.

For the harp tube section, steam mass flow rate through each tube and temperature at the inlet of each tube, as obtained from inlet section solution, are used as inlet boundary conditions. P_o is again used as the outlet pressure boundary condition. The outside heat transfer coefficient for the tube bank and flue gas temperature for each harp tube row, explained in section 3.5.2, are used as boundary conditions for the tube wall outer surface.

Results are obtained for velocity, pressure, and temperature distributions of steam. The average pressure drop in steam through the harp tube section, ΔP_2, is calculated from the results.

The outlet section is solved with the steam temperature and mass flow rate at the exit of the tubes, as obtained from the harp tube section solution, as the inlet boundary conditions, and P_o as the outlet pressure boundary condition for the steam domain. For the flue gas domain, uniform velocity at the inlet plane and uniform pressure at the outlet plane, obtained from the full HRSG model solution,

46

are used, respectively, as the inlet and outlet boundary conditions. Flue gas temperature at the HRSG inlet is used as inlet temperature for the flue gas domain.

Results are obtained for velocity, pressure, and temperature distributions of steam and flue gas for the section. Pressure drop in steam through the outlet section, ΔP_3, is calculated from the results.

Finally, the inlet and harp tube sections are solved again with the steam pressure at the exit of the sections set equal to $(P_o + \Delta P_2 + \Delta P_3)$ and $(P_o + \Delta P_3)$, respectively, as the outlet boundary conditions.

3.6.2 Transients

The time-varying steam temperature at the HPSH1 inlet, $T_{in}(t)$, as well as pressure, $P_o(t)$, and mass flow rate, $m_o(t)$, at the HPSH1 exit are measured at the plant during the cold start-up transient.

During any transient, steam mass flow rates at the inlet and exit of HPSH1 are not equal. To begin the solution, it is assumed that the difference between mass flow rates of steam at the inlet and the exit, $\Delta m(t)$, at any time is negligible compared to $m_o(t)$. It is also assumed that the pressure drop in steam through the HPSH1 at any time is negligible compared to $P_o(t)$. These two assumptions must be justified later from the obtained results. The detailed method for solving the transient condition is provided in the flowchart shown in figure 3.28.

First, the flue gas velocity and pressure distributions in the HPSH1 region are obtained from the full HRSG model solution, detailed in section 3.3. The

47

results, thus obtained, provide flue gas velocity profile, $U(y,t)$, upstream of the HPSH1 and pressure profile, $P(y,t)$, downstream of the HPSH1 as functions of height, $y = 0$ ft. – 66 ft., and time.

Next, the inlet section is solved with $m_o(t)$ and $T_{in}(t)$ as the inlet boundary conditions and $P_o(t)$ as the outlet pressure boundary condition for the steam domain. For the flue gas domain of this section, the uniform velocity at the inlet plane, equal to $U(y=65.5ft.,t)$, and the uniform pressure at the outlet plane, equal to $P(y=65.5ft.,t)$ are used, respectively, as the inlet and the outlet boundary conditions. Flue gas temperature at the HRSG inlet is used as the temperature at the flue gas domain inlet.

Results are obtained for velocity, pressure, and temperature distributions of steam and flue gas.

Steam mass flow rate and temperature at the inlet of each harp tube are obtained as a function of time from the inlet section results. The results also provide the pressure drop in steam through the inlet section, $\Delta P_1(t)$, and used to verify that $\Delta m(t)$ for the section is negligible compared to $m_o(t)$.

Due to the large computational cost for the harp tube section, the 42 harp tubes of each row are subdivided into four types based on the steam mass flow rate at their inlet. Only four tubes per row, one corresponding to each type, are solved instead of solving the 42 tubes; it is assumed that all tubes belonging to each type have the same velocity, pressure, and temperature distributions.

The harp tubes are solved with steam mass flow rates and temperatures specified as function of time at the inlet of the tubes as inlet boundary conditions, and $P_o(t)$ as the outlet pressure boundary condition. The height dependent outside heat transfer coefficient, $h(y,t)$ for the tube bank, and the uniform flue gas temperature along the tube length for each harp tube row are used as boundary conditions for the outer surface of the tube wall.

Results are obtained for velocity, pressure, and temperature distributions of steam for the section. The results also provide the pressure drop in steam through the section, $\Delta P_2(t)$, and are used to verify that $\Delta m(t)$ for each tube is negligible compared to the mass flow rate through the tube.

The outlet section is solved with the steam mass flow rates and temperatures prescribed at the exit of the harp tubes, obtained from the harp tubes section solution, as the inlet boundary conditions, and $P_o(t)$ as the outlet pressure boundary condition for the steam domain.

For the flue gas domain of this section, uniform velocity at the inlet plane, equal to $U(y=0.5\text{ft},t)$, and uniform pressure at the outlet plane, equal to $P(y=0.5\text{ft},t)$, are used, respectively, as inlet and outlet boundary conditions. Flue gas temperature at the HRSG inlet is used as the temperature at the flue gas domain inlet.

Results are obtained for velocity, pressure, and temperature distributions of steam and flue gas. The results also provide the pressure drop in steam through

the section, $\Delta P_3(t)$, and are used to verify that $\Delta m(t)$ for the section is negligible compared to $m_o(t)$.

After solving all three sections, it is checked whether that the total pressure drop in steam, $\Delta P(t) = \Delta P_1(t) + \Delta P_2(t) + \Delta P_3(t)$, across the HPSH1 is negligible compared to $P_o(t)$.

In the event that $\Delta P(t)$ is found to be significant compared to $P_o(t)$, the inlet and harp tube sections are solved again with $P_o(t) + \Delta P_2(t) + \Delta P_3(t)$ and $P_o(t) + \Delta P_3(t)$, respectively, as the pressure outlet boundary conditions for the steam domain to obtain the final solution.

Total steam mass flow rate, $m_o(t)$ and pressure, $P_o(t)$ are known at outlet of HPSH1; inlet temperature $T_{in}(t)$ is known at inlet of HPSH1

↓

Divide entire *HPSH1* assembly in 3 sections as shown in figure; *inlet section, harp tubes section* and, *outlet section*

Flue gas inlet mass flow rate, m(t), temperature T1(t) are known at HRSG inlet

Solve for steam and flue gas velocity, pressure, and temperature for *inlet section* with following inputs: Fluent
- mo(t) as total steam inlet mass flow rate
- Po(t) as steam outlet pressure
- Steam inlet temperature, Tin(t)
- Uniform inlet flue gas velocity U(65.5',t) upstream of HPSH1*
- Uniform outlet flue gas pressure P(65.5',t) downstream of HPSH1*
- Inlet flue gas temperature, T1(t)

Obtain results of flue gas velocity and temperature; steam mass flow rate and temperature at inlet of each harp tube (3x42). Also calculate pressure drop across inlet section, $\Delta P1(t)$, and verify that $\Delta m(t)$ for inlet section <<< $m_o(t)$

Calculate outside heat transfer coefficient h(y,t) for all 3 rows along its length from flue gas velocity upstream of HPSH1, U(y,t), using correlation

Subdivide 42 harp tubes of each row into 4 types based upon steam mass flow rate through tubes obtained from solving *inlet section*

Solve for steam velocity, pressure and temperature for *4 types each row* for all 3 rows with following inputs: Fluent
- Steam mass flow rate obtained from inlet section
- Inlet steam temperature obtained from inlet section
- Steam outlet pressure as Po(t)
- Uniform average outside flue gas temperature, Ti(t), for each row (i=1-3)*
- Outside heat transfer coefficient h(y,t) for tubes along their length

Obtain results for steam mass flow rate and temperature at outlet of the 4 types each row; also calculate pressure drop across tube section, $\Delta P2(t)$, and verify $\Delta m(t)$ for each tube <<<mass flow rate through each tube

Calculate pressure drops across tube banks, module 1 through module 5, using Wierman correlation

Solve for flue gas velocity inside *HRSG* casing with following inputs: Fluent
- m(t) as inlet flue gas mass flow rate
- HRSG outlet pressure is back-calculated from stack
- Use radiator feature to define pressure drops across perforated plate, tube banks, and SCR catalyst

Get flue gas velocity profile U(y,t) upstream of HPSH1 and pressure profile, P(y,t) downstream of HPSH1

To next page

Notes:
- $\Delta m(t)$ = steam inlet mass flow rate at time t – steam outlet mass flow rate at time t, $\Delta P(t)$=pressure drop for steam at time t

Figure 3.28 Soution method for HPSH1 transient model

51

From previous page

Impose result of steam mass flow rate and outlet temperature of 4 types each row on *42 tubes each row for all 3 rows;* at inlet of *outlet section*

Solve for steam and flue gas velocity, pressure and temperature for *outlet section* with following inputs:

- Steam mass flow rate for each tube obtained from harp tubes section
- Steam temperature for each tube obtained from harp tubes section
- Po(t) as steam outlet pressure
- Uniform inlet flue gas velocity U(0.5',t) upstream of HPSH1
- Uniform outlet flue gas pressure P(0.5',t) downstream of HPSH1
- Inlet flue gas temperature , T1(t)

Fluent

Obtain results of steam and flue gas velocity and temperature; steam pressure drop across outlet section, ΔP3(t); also verify that Δm(t) for outlet section <<< m_o(t)

Is total *ΔP(t) = ΔP1(t)+ΔP2(t)+ ΔP3(t)* significant

Yes
Back to inlet section

Solve for inlet section again with updated steam pressure at outlet of inlet section as P_o(t)+ ΔP2(t)+ ΔP3(t)

To harp tubes section

Solve for 4tubes/row again with updated steam pressure at tube outlet as P_o(t)+ ΔP3(t)

STOP

Inlet Section
Harp Tubes Section
Outlet Section

Notes:
- Solution flow chart is for one iteration only

Figure 3.28 (contd.)

52

3.6 Physical and thermodynamic properties of materials

It is important that accurate physical and thermodynamic properties of materials are used in CFD simulation.

3.6.1 Flue gas

The composition of flue gas is given in table 3.5.

Gas	Percentage by volume
N_2	72.46
O_2	12.17
H_2O	10.79
CO_2	3.72
Ar	0.87

Table 3.5 Composition of flue gas

Based on this composition, physical and thermal properties of flue gas are calculated. It was observed from the calculations that these properties are insensitive to the flue gas pressure range of 0 - 3250 Pa (g), measured at the plant. Hence, the flue gas properties are considered only as a function of temperature. The variation of flue gas density, specific heat, thermal conductivity, and molecular viscosity with temperature are shown in figures 3.29, 3.30, 3.31, and 3.32, respectively.

Polynomial fits to these property variations with temperature were used in the CFD simulations.
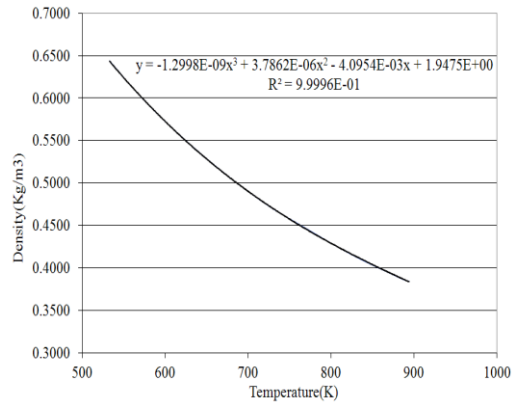
Figure 3.29 Density of the flue gas
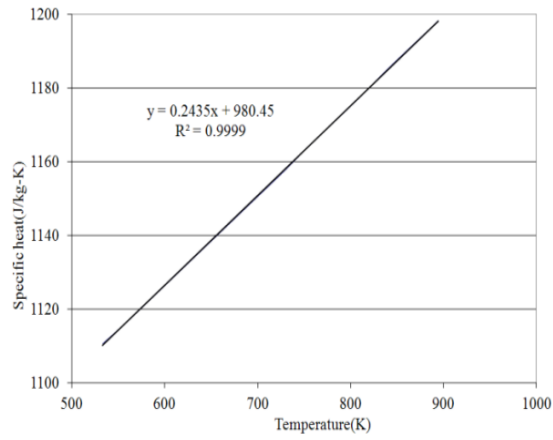
Figure 3.30 Specific heat of the flue gas
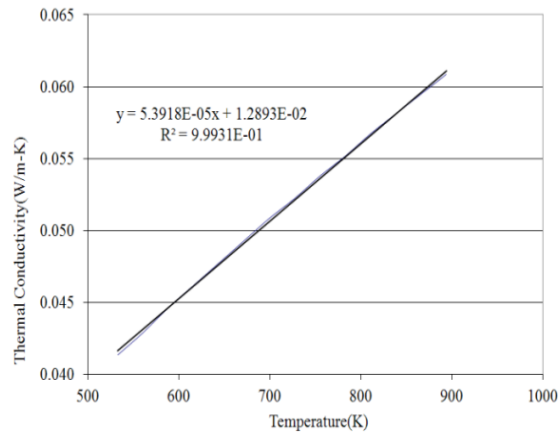
Figure 3.31 Thermal conductivity of the flue gas
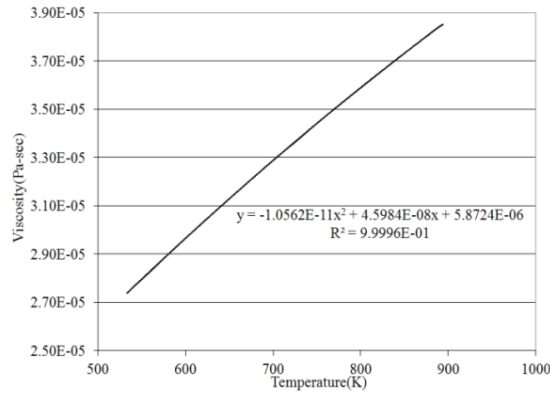
Figure 3.32 Molecular viscosity of the flue gas

3.6.2 Steam

The physical and thermal properties of steam are functions of pressure and temperature. User defined functions (UDF) were compiled for specific heat, enthalpy, density, conductivity and molecular viscosity of steam. Steam properties were obtained from Engineering Equation Solver (EES) software.

3.6.3 P91 Steel

P91/T91 is an alloy steel with the composition of 9 percent Cr and 1 percent Mo. Properties of this material were obtained from [13].

Figures 3.33, 3.34, and 3.35 show, respectively, the variations of density, specific heat, and thermal conductivity for the material with temperature.

Polynomial fits to these property variations with temperature were used in model calculations.

55
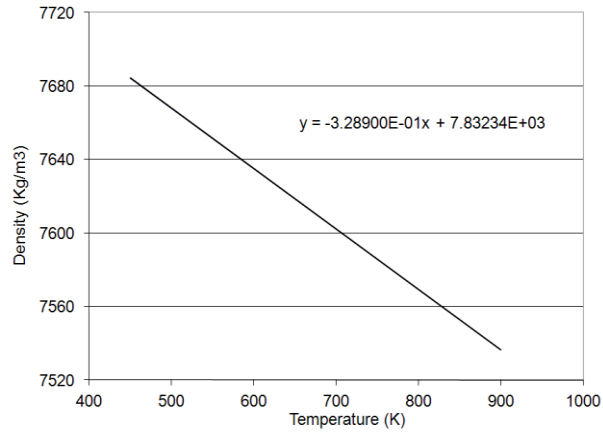
Figure 3.33 Density of P91 steel

$y = -3.28900E\text{-}01x + 7.83234E\text{+}03$
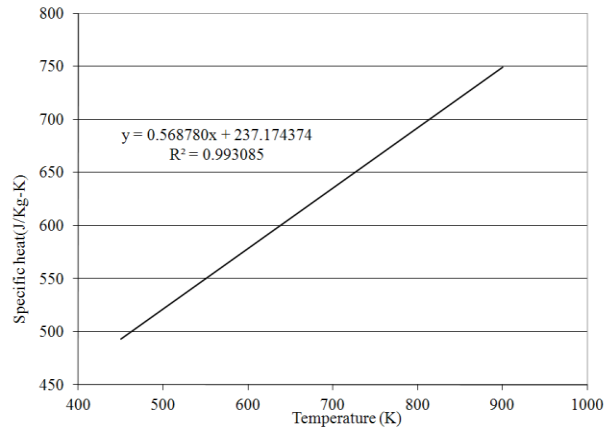
Figure 3.34 Specific heat of P91 steel

$y = 0.568780x + 237.174374$
$R^2 = 0.993085$
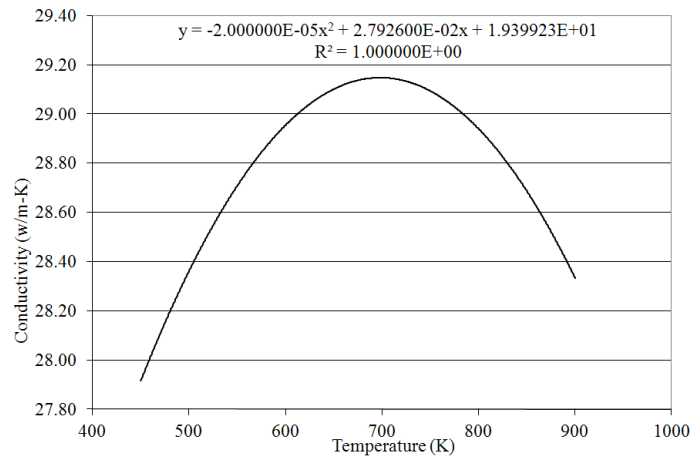
Figure 3.35 Thermal conductivity of P91 steel

$y = -2.000000E\text{-}05x^2 + 2.792600E\text{-}02x + 1.939923E\text{+}01$
$R^2 = 1.000000E\text{+}00$

CHAPTER 4

THE CFD TOOL

CFD is the use of computational power to numerically solve for velocity, pressure, and temperature distributions in fluid flow from the governing equations.

In this work, the commercial CFD tool ANSYS-Fluent is used. This chapter provides an introduction to ANSYS-Fluent, along with the governing equations, the k-ε turbulence model, the pressure-based flow solver, the standard wall function, and the boundary conditions for the computational domain.

4.1   Fluent-introduction

The CFD tool ANSYS-Fluent solves problems involving fluid flow in industrial and research systems. It can model three-dimensional/two-dimensional problems for incompressible/compressible, inviscid/viscous, laminar/turbulent, and single-phase/multi-phase flows. ANSYS-Fluent also has capability of modeling heat transfer, chemical reactions, and combustion reactions.

The governing partial differential equations of mass, momentum, and energy conservation are converted to algebraic equations using the finite-volume method. The algebraic equations are then solved numerically. The governing equations are as follows.

Mass conservation

$$\frac{\partial \rho}{\partial t} + \frac{\partial \rho \vec{v}}{\partial x} = S_m \tag{36}$$

57

In this equation, S_m is the source term for mass, ρ is density, and $\vec{v}$ the velocity vector.

Momentum conservation

$$\underbrace{\frac{\partial(\rho\vec{v})}{\partial t}}_{\text{local acceleration}} + \underbrace{\nabla.(\rho\vec{v}\vec{v})}_{\text{advection}} = \underbrace{-\nabla p}_{\text{pressure gradient}} + \underbrace{\nabla^2(\bar{\bar{\tau}})}_{\text{diffusion}} + \underbrace{\rho\vec{g}+\vec{F}}_{\text{body forces}} \tag{37}$$

In the above equation, p is static pressure, $\bar{\bar{\tau}}$ is stress tensor, and $\rho\vec{g}$ and $\vec{F}$ are gravitational and external body forces, respectively. For newtonian fluids, the stress tensor is defined as:

$$\bar{\bar{\tau}} = \mu\left[(\nabla\vec{v} + \nabla\vec{v}^T) - \frac{2}{3}\nabla.\vec{v}I\right] \tag{38}$$

where, μ is the fluid molecular viscosity, and I the unit tensor.

Energy conservation

For a fluid region, the energy equation is:

$$\frac{\partial(\rho E)}{\partial t} + \nabla.(\vec{v}(\rho E + p)) = \nabla.(k_{eff}\nabla T - \sum_j h_j \vec{J}_j + (\bar{\bar{\tau}}_{eff}.\vec{v}) + S_h \tag{39}$$

For a solid region, the thermal energy equation is:

$$\frac{\partial(\rho_s h_s)}{\partial t} + \nabla.(\vec{u}\rho_s h_s) = \nabla.(k_s\nabla T) + S_s \tag{40}$$

where

$$E = h - \frac{p}{\rho} + \frac{v^2}{2} \tag{41}$$

$$k_{eff} = (k + k_t) \tag{42}$$

Here, h is sensible enthalpy, k is thermal conductivity, k_t is the turbulent thermal conductivity of the fluid, and $\vec{J}_j$ the diffusion flux of species j, h_s is sensible enthalpy, ρ_s is density, and k_s the thermal conductivity of the solid.

The first three terms on the right-hand side of equation (39) represent, respectively, the energy transfer due to conduction, species diffusion, and viscous dissipation. S_h is the heat source term.

The second term on the left-hand side of equation (40) is accounts for convective energy transfer due to rotational or translational motion of solid body. The first term on the right-hand side is accounts for heat conduction within the solid.

4.2   Reynolds-averaged Navier-Stokes (RANS) equations

Fluid flow can be laminar or turbulent depending on the Reynolds number. Turbulent flow is characterized by a chaotic or fluctuating velocity field. The flow is fundamentally unsteady and causes augmented mixing of transported quantities such as momentum and energy. As such, the local instantaneous governing equations are time/ensemble-averaged to obtain a simplified set of equations that are computationally less challenging.

In the Reynolds-averaging method, the unsteadiness is considered to be a part of the turbulence. The variables are decomposed into to mean (time/ensemble-average) and fluctuating parts:

For example, for the fluid:

$$u = \bar{u} + u' \tag{43}$$

$$v = v + v' \tag{44}$$

$$w = \bar{w} + w' \tag{45}$$

where, u, v, and w are instantaneous velocity components in x, y, and z directions, respectively. Likewise, for pressure and other scalar variables:

$$\emptyset_i = \overline{\emptyset}_i + \emptyset_i' \tag{46}$$

where, Φ_i denotes a scalar such as pressure or energy in i_{th} direction (i = x, y, z)

Substituting the decomposed variables into the conservation equations, and taking a time/ensemble-average, the Reynolds-average Navier-Stokes equations (49) – (51) are obtained. Because of the non-linearity in momentum and thermal energy equations, turbulent or Reynolds stress terms appear from the fluctuating part of the turbulence.

The Reynolds stresses must be modeled for the closure of the equations. This can be done using the Boussinesq hypothesis, which relates these terms to the mean velocity components, equations (52) through (57).

$$\frac{\partial \rho}{\partial t} + \frac{\partial \overline{\rho u}}{\partial x} + \frac{\partial \overline{\rho v}}{\partial y} + \frac{\partial \overline{\rho w}}{\partial z} = 0 \tag{47}$$

$$\underbrace{\frac{\partial \overline{u}}{\partial t}}_{local\ acceleration} + \underbrace{\frac{\partial \overline{uu}}{\partial x} + \frac{\partial \overline{vu}}{\partial y} + \frac{\partial \overline{wu}}{\partial z}}_{advection\ term} = \underbrace{-\frac{1}{\rho}\frac{\partial p}{\partial x}}_{pressure\ gradient} + \underbrace{\frac{\partial}{\partial x}\left(\nu\frac{\partial \overline{u}}{\partial x}\right) + \frac{\partial}{\partial y}\left(\nu\frac{\partial \overline{u}}{\partial y}\right) + \frac{\partial}{\partial z}\left(\nu\frac{\partial \overline{u}}{\partial z}\right)}_{diffusion\ term} -$$

$$\underbrace{\left[\frac{\partial(\overline{u'u'})}{\partial x} + \frac{\partial(\overline{u'v'})}{\partial y} + \frac{\partial(\overline{u'w'})}{\partial z}\right]}_{gradients\ of\ Reynolds\ stresses} \tag{48}$$

$$\underbrace{\frac{\partial \overline{v}}{\partial t}}_{local\ acceleration} + \underbrace{\frac{\partial \overline{uv}}{\partial x} + \frac{\partial \overline{vv}}{\partial y} + \frac{\partial \overline{wv}}{\partial z}}_{advection\ term} = \underbrace{-\frac{1}{\rho}\frac{\partial p}{\partial y}}_{pressure\ gradient} + \underbrace{\frac{\partial}{\partial x}\left(\nu\frac{\partial \overline{v}}{\partial x}\right) + \frac{\partial}{\partial y}\left(\nu\frac{\partial \overline{v}}{\partial y}\right) + \frac{\partial}{\partial z}\left(\nu\frac{\partial \overline{v}}{\partial z}\right)}_{diffusion\ term} -$$

$$\underbrace{\left[\frac{\partial(\overline{v'u'})}{\partial x} + \frac{\partial(\overline{v'v'})}{\partial y} + \frac{\partial(\overline{v'w'})}{\partial z}\right]}_{gradients\ of\ Reynolds\ stresses} \tag{49}$$

$$\underbrace{\frac{\partial \overline{w}}{\partial t}}_{local\ acceleration} + \underbrace{\frac{\partial \overline{uw}}{\partial x} + \frac{\partial \overline{vw}}{\partial y} + \frac{\partial \overline{ww}}{\partial z}}_{advection\ term} =$$

$$\underbrace{-\frac{1}{\rho}\frac{\partial p}{\partial z}}_{pressure\ gradient} + \underbrace{\frac{\partial}{\partial x}\left(\nu\frac{\partial \overline{w}}{\partial x}\right) + \frac{\partial}{\partial y}\left(\nu\frac{\partial \overline{w}}{\partial y}\right) + \frac{\partial}{\partial z}\left(\nu\frac{\partial \overline{w}}{\partial z}\right)}_{diffusion\ term} - \underbrace{\left[\frac{\partial(\overline{w'u'})}{\partial x} + \frac{\partial(\overline{w'v'})}{\partial y} + \frac{\partial(\overline{w'w'})}{\partial z}\right]}_{gradients\ of\ Reynolds\ stresses} \tag{50}$$

$$\underbrace{\frac{\partial \overline{T}}{\partial t}}_{unsteady\ term} + \underbrace{\frac{\partial \overline{uT}}{\partial x} + \frac{\partial \overline{vT}}{\partial y} + \frac{\partial \overline{wT}}{\partial z}}_{advection\ term} =$$

$$\underbrace{\frac{\partial}{\partial x}\left(\frac{k}{\rho c_p}\frac{\partial \overline{T}}{\partial x}\right) + \frac{\partial}{\partial y}\left(\frac{k}{\rho c_p}\frac{\partial \overline{T}}{\partial y}\right) + \frac{\partial}{\partial z}\left(\frac{k}{\rho c_p}\frac{\partial \overline{T}}{\partial z}\right)}_{molecular\ diffusion\ term} - \underbrace{\left[\frac{\partial(\overline{T'u'})}{\partial x} + \frac{\partial(\overline{T'v'})}{\partial y} + \frac{\partial(\overline{T'w'})}{\partial z}\right]}_{gradients\ of\ turbulent\ heat\ fluxes} \tag{51}$$

$$-\rho\overline{u'u'} = 2\mu_t \frac{\partial(\overline{u})}{\partial x} - \frac{2}{3}\rho k \tag{52}$$

$$-\rho\overline{u'v'} = \mu_t \left(\frac{\partial(\overline{v})}{\partial x} + \frac{\partial(\overline{u})}{\partial y}\right) \tag{53}$$

$$-\rho\overline{u'w'} = \mu_t \left(\frac{\partial(\overline{w})}{\partial x} + \frac{\partial(\overline{u})}{\partial z}\right) \tag{54}$$

$$-\rho\overline{v'v'} = 2\mu_t \frac{\partial(\overline{v})}{\partial y} - \frac{2}{3}\rho k \tag{55}$$

$$-\rho\overline{v'w'} = \mu_t \left(\frac{\partial(\overline{w})}{\partial y} + \frac{\partial(\overline{v})}{\partial z}\right) \tag{56}$$

$$-\rho\overline{w'w'} = 2\mu_t \frac{\partial(\overline{w})}{\partial z} - \frac{2}{3}\rho k \tag{57}$$

The right-hand side of the above equations are analogous to Newton's law of viscosity, except for the appearance of turbulent or eddy viscosity, μ_t, and turbulent kinetic energy, k.

The turbulent transport energy can also be related to mean temperature as follows:

$$-\rho\overline{u'T'} = \Gamma_T \frac{\partial(\overline{T})}{\partial x} \tag{58}$$

$$-\rho\overline{v'T'} = \Gamma_T \frac{\partial(\overline{T})}{\partial y} \tag{59}$$

$$-\rho\overline{w'T'} = \Gamma_T \frac{\partial(\overline{T})}{\partial z} \tag{60}$$

where, Γ_T is turbulent thermal diffusivity.

The turbulent Prandtl number, Pr_T, is defined as the ratio of turbulent viscosity and turbulent diffusivity.

$$Pr_T = \frac{\mu_T}{\Gamma_T} \tag{61}$$

The values of turbulent diffusivity and turbulent viscosity are not too different, since the turbulent transports of momentum and thermal energy are due to the same mechanism: eddy mixing. As such, the value of turbulent Prandtl number is taken as close to unity.

4.3   Turbulence model

There is no single universally accepted turbulence model for all turbulent fluid flow. A model can be chosen depending on the flow region, the physics included of the flow, the level of accuracy needed, desired results from the problem, computational resources, and computational time.

For this work, the standard k-ε turbulence model is used.

4.3.1   The standard k-ε model

In the standard k-ε model, the turbulent viscosity is calculated as a algebraic function of turbulent kinetic energy, k, and turbulent dissipation rate, ε. Two additional governing transport equations, one for turbulent kinetic energy and one for turbulence dissipation rate, are prescribed. This model is valid for only fully turbulent flow with negligible molecular viscosity effects.

The transport equation for k is derived from the exact equation, while the transport equation for ε is obtained using physical reasoning and bears little resemblance to its mathematically exact counterpart. This model assumes that μ_T is an isotropic scalar quantity, meaning that the ratio between Reynolds stress and mean rate of deformation are the same in all directions.

63

The velocity scale, ϑ, and length scale, l, are determined from turbulent kinetic energy and turbulent dissipation rate. The eddy viscosity is then defined in terms of these two scales as follows:

$$\mu_t = \rho C_\mu \vartheta l = \rho C_\mu \frac{k^2}{\varepsilon} \quad ; \quad \vartheta = k^{1/2} \quad ; \quad l = \frac{k^{3/2}}{\varepsilon} \tag{62}$$

The transport equations for k and ε are:

Turbulent kinetic energy:

$$\frac{\partial k}{\partial t} + u\frac{\partial k}{\partial x} + v\frac{\partial k}{\partial y} + w\frac{\partial k}{\partial z} = \frac{\partial}{\partial x}\left(\frac{v_T}{\sigma_k}\frac{\partial k}{\partial x}\right) + \frac{\partial}{\partial y}\left(\frac{v_T}{\sigma_k}\frac{\partial k}{\partial y}\right) + \frac{\partial}{\partial z}\left(\frac{v_T}{\sigma_k}\frac{\partial k}{\partial z}\right)$$

$$+P - D \tag{63}$$

Viscous dissipation rate:

$$\frac{\partial \epsilon}{\partial t} + u\frac{\partial \epsilon}{\partial x} + v\frac{\partial \epsilon}{\partial y} + w\frac{\partial \epsilon}{\partial z} = \frac{\partial}{\partial x}\left(\frac{v_T}{\sigma_\epsilon}\frac{\partial \epsilon}{\partial x}\right) + \frac{\partial}{\partial y}\left(\frac{v_T}{\sigma_\epsilon}\frac{\partial \epsilon}{\partial y}\right) + \frac{\partial}{\partial z}\left(\frac{v_T}{\sigma_\epsilon}\frac{\partial \epsilon}{\partial z}\right)$$

$$+\frac{\epsilon}{k}(C_{\varepsilon 1}P - C_{\varepsilon 2}D) \tag{64}$$

Here, the destruction term, D, and the production term, P, are:

$$D = \epsilon \tag{65}$$

$$P = 2v_T\left[\left(\frac{\partial u}{\partial x}\right)^2 + \left(\frac{\partial v}{\partial y}\right)^2 + \left(\frac{\partial w}{\partial z}\right)^2\right] +$$

$$v_T\left[\left(\frac{\partial u}{\partial y} + \frac{\partial v}{\partial x}\right)^2 + \left(\frac{\partial v}{\partial z} + \frac{\partial w}{\partial y}\right)^2 + \left(\frac{\partial w}{\partial x} + \frac{\partial u}{z}\right)^2\right] \tag{66}$$

The five empirical constraints have been estimated from experimental results for a wide range of turbulent flows:

$$C_\mu = 0.09; \quad \sigma_k = 1.00; \quad \sigma_\varepsilon = 1.30; \quad C_{1\varepsilon} = 1.44; \quad C_{2\varepsilon} = 1.92 \tag{67}$$

The final form of the governing conservation equations in Cartesian coordinates, after removing the average sign, are shown in equations (68) to (72).

Continuity equation

$$\frac{\partial \rho}{\partial t} + \frac{\partial \rho u}{\partial x} + \frac{\partial \rho v}{\partial y} + \frac{\partial \rho w}{\partial z} = 0 \tag{68}$$

Momentum equations

$$\underbrace{\frac{\partial u}{\partial t}}_{local\ acceleration} + \underbrace{\frac{\partial uu}{\partial x} + \frac{\partial vu}{\partial y} + \frac{\partial wu}{\partial z}}_{advection\ term} = \underbrace{-\frac{1}{\rho}\frac{\partial p}{\partial x}}_{pressure\ gradient}$$

$$+ \underbrace{\frac{\partial}{\partial x}\left[(v + v_T)\frac{\partial u}{\partial x}\right] + \frac{\partial}{\partial y}\left[(v + v_T)\frac{\partial u}{\partial y}\right] + \frac{\partial}{\partial z}\left[(v + v_T)\frac{\partial u}{\partial z}\right]}_{diffusion\ term} + \underbrace{S_u'}_{Source\ term} \tag{69}$$

$$\underbrace{\frac{\partial v}{\partial t}}_{local\ acceleration} + \underbrace{\frac{\partial uv}{\partial x} + \frac{\partial vv}{\partial y} + \frac{\partial wv}{\partial z}}_{advection\ term} = \underbrace{-\frac{1}{\rho}\frac{\partial p}{\partial y}}_{pressure\ gradient}$$

$$+ \underbrace{\frac{\partial}{\partial x}\left[(v + v_T)\frac{\partial v}{\partial x}\right] + \frac{\partial}{\partial y}\left[(v + v_T)\frac{\partial v}{\partial y}\right] + \frac{\partial}{\partial z}\left[(v + v_T)\frac{\partial v}{\partial z}\right]}_{diffusion\ term} + \underbrace{S_v'}_{Source\ term} \tag{70}$$

$$\underbrace{\frac{\partial w}{\partial t}}_{local\ acceleration} + \underbrace{\frac{\partial uw}{\partial x} + \frac{\partial vw}{\partial y} + \frac{\partial ww}{\partial z}}_{advection\ term} = \underbrace{-\frac{1}{\rho}\frac{\partial p}{\partial z}}_{pressure\ gradient}$$

$$+ \underbrace{\frac{\partial}{\partial x}\left[(v + v_T)\frac{\partial w}{\partial x}\right] + \frac{\partial}{\partial y}\left[(v + v_T)\frac{\partial w}{\partial y}\right] + \frac{\partial}{\partial z}\left[(v + v_T)\frac{\partial w}{\partial z}\right]}_{diffusion\ term} + \underbrace{S_w'}_{Source\ term} \tag{71}$$

Thermal energy equation

$$\underbrace{\frac{\partial T}{\partial t}}_{unsteady\ term} + \underbrace{\frac{\partial uT}{\partial x} + \frac{\partial vT}{\partial y} + \frac{\partial wT}{\partial z}}_{advection\ term} =$$

$$\underbrace{\frac{\partial}{\partial x}\left[\left(\frac{v}{Pr} + \frac{v_T}{P_T}\right)\frac{\partial T}{\partial x}\right] + \frac{\partial}{\partial y}\left[\left(\frac{v}{Pr} + \frac{v_T}{Pr_T}\right)\frac{\partial T}{\partial y}\right] + \frac{\partial}{\partial z}\left[\left(\frac{v}{Pr} + \frac{v_T}{Pr_T}\right)\frac{\partial T}{\partial z}\right]}_{diffusion\ term} + \underbrace{S_T}_{Source\ term} \tag{72}$$

where, $v_T = \frac{\mu_T}{\rho}$; and $Pr_T = 0.85$. $\tag{73}$

S_u', S_v', and S_w' are momentum source terms for fluid in x, y, and z

direction. S_T is heat source term.

4.3.2 Near-wall model

The presence of wall plays an important role in wall-bounded turbulent flows. It is very important to accurately solve for flow in the near-wall region to get an accurate flow solution in a fluid region.

With no-slip boundary condition at the wall, the all components of velocity are zero. Flow is essentially laminar very near a wall, as viscous damping reduces the velocity fluctuations.
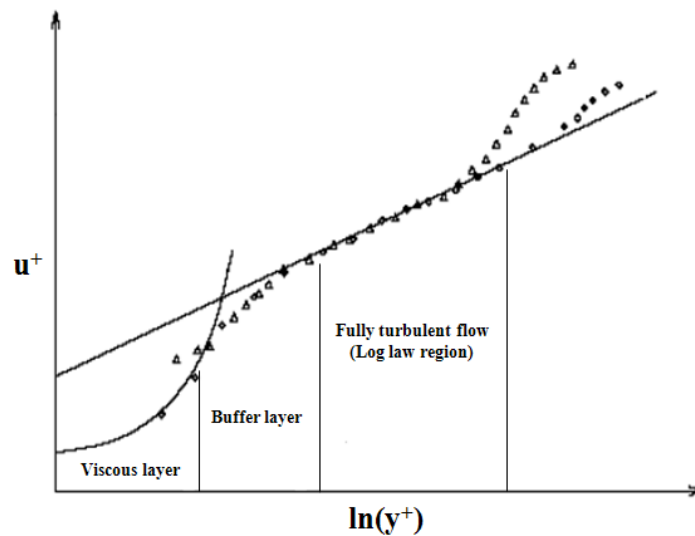
The near wall region can be divided into three layers, figure 4.1 [12].

Figure 4.1 Near-wall region for turbulent flow

In this figure, u^+ and y^+ are dimensionless velocity and distance from the wall, respectively:

$$u^+ = \frac{u}{u_\tau} \tag{74}$$

$$y^+ = \frac{y*u_\tau*\rho}{\mu} \tag{75}$$

where, $u_\tau = \sqrt{\frac{\tau_w}{\rho}}$ is frictional velocity, and τ_w is wall shear stress.

Very near the wall is viscous layer (0<y$^+$<5). In this layer, flow is essentially laminar, and molecular viscosity plays an important role. Next is the buffer layer (5<y$^+$<30). In this layer, viscous and turbulent mechanisms are equally important. This layer represents a transition from the viscous layer to the third region, the outer fully turbulent region, which is also called the "log-layer region". In this region (y$^+$>30), turbulence plays a major role; the y$^+$ upper limit depends on the flow Reynolds number.

For viscous layer: $u^+ = y^+$ $\hspace{4cm}$ (76)

For log layer region: $u^+ = \frac{1}{k} \ln(y^+) + C$ $\hspace{3cm}$ (77)

k is *von Kármán* constant (≈0.42), and C is a constant = 0.50.

The near-wall region can be modeled by two approaches. The first approach is to solve for the molecular viscosity-affected region with meshes inside the viscous and buffer layer regions, termed "near-wall modeling". This approach is expensive and requires a very refined mesh close to the wall. The second approach is not to resolve the viscosity-affected region. This method calls for the use of a semi-empirical formula, "wall function", to bridge the viscosity-affected region and the fully turbulent region. The use of wall function obviates the need to modify turbulence models to account for the presence of the wall [12].

In this work, standard wall function is used for near-wall modeling.

The standard wall function

It is necessary to use semi-empirical formulae to link solution variables close to a wall cell (the first near wall node) to the wall surface. The law of the wall for mean velocity is of the form:

$$u^* = \frac{1}{k}\ln(Ey^*) \tag{78}$$

where, u* and y* are non-dimensionalized velocity and distance from the wall, respectively:

$$u^* = \frac{u_p C_\mu^{1/4} k_p^{1/2}}{\tau_w/\rho}\ln(Ey^*) \tag{79}$$

$$y^* = \frac{\rho C_\mu^{1/4} k_p^{1/2} y_p}{\mu} \tag{80}$$

E is a function of wall roughness, and equal to 9.73 for smooth walls; u_p is the mean velocity of fluid at node P, k_p is turbulent kinetic energy at node P, and y_p is distance of P from the wall.

The law of the wall is applied to determine wall temperature (T_w).

$$T^* \equiv \frac{(T_w - T_p)\rho c_p k_p^{1/2}}{\dot{q}} \tag{80}$$

where, $\dot{q}$ is wall heat flux, T_p is temperature at node P; and T_w is wall temperature.

It has to be noted that in ANSYS-Fluent, laws-of-the-wall are based upon y^* and u^* rather that y^+ and u^+ [12].

4.4   Flow solver

ANSYS-Fluent has two numerical method approaches for solving the governing equations. The first is the pressure-based solver, and the second the density based solver. Originally, the pressure-based solver was meant for low speed incompressible flow and the density-based solver was meant for high speed compressible flow. In recent years, both methods have been extended to a wider range of flow conditions.

ANSYS-Fluent uses the control volume-based technique with a co-located scheme in both the approaches. The main steps for both solvers include [12]:

- dividing the computational domain into discrete control volumes using a mesh generation tool.

- integrating the governing equations over individual control volumes to construct algebraic equations for the discrete dependent variables ("unknowns") such as velocity, pressure, temperature, and conserved scalars.

- linearizing the discretized algebraic equations and solving them to obtain updated values of the dependent variables.

The discretization process is similar for the two solvers, however the approach for linearizing and solving the discretized equations differs [12].

In both methods, the velocity field is obtained from the momentum equations. In the density-based solver, the pressure field is obtained from the equation of state. However, due to the assumption of incompressible flow in the

pressure-based solver, the equation of state does not solve for the pressure field. Instead the pressure field is solved from a pressure correction equation which is obtained by manipulating the continuity and momentum equations.

In the present work, the pressure-based solver is used.

4.4.1 Pressure-based solver

In the pressure-based solver, there are four equations (47) – (50) and four unknowns (u, v, w, P). The solver employs a projection method algorithm. In the projection method, the constraint of mass conservation is achieved by solving the pressure correction equation which is derived from continuity and momentum equations in such a way that the velocity field, corrected by the pressure, satisfies the continuity equation. The solution process involves iterations, as the governing equations are non-linear and coupled.

ANSYS-Fluent has two pressure-based solver algorithms: segregated and coupled. In the segregated algorithm, the governing equations are solved sequentially. The coupled algorithm solves a coupled system of equations comprised of the pressure correction and momentum equations.

The remaining governing equations of temperature, species, turbulence, and other scalars are solved in a de-coupled fashion in both algorithms. The segregated algorithm is memory-efficient since the discretized equations need to be stored in the memory only once at a time during calculations [12].

In the present work, the segregated algorithm is used for the pressure based solver.

ANSYS-Fluent has four velocity-pressure coupling schemes for segregated pressure-based solver algorithm: SIMPLE, SIMPLEC, PISO, and Fractional Step (FSM).

In the present work, the SIMPLE (Semi-Implicit Method for Pressure-Linkage equations) algorithm is used for velocity-pressure coupling. The steps involved in the SIMPLE algorithm are as follows.

1)   momentum equations are solved using guessed pressure field p* and velocity components u*, v*, and w*. The solution of discretized momentum equations yields updated velocity components u*, v*, and w*.

2)   the correction is defined as the difference between the correct value and the guessed value for pressure and velocity;

$$p = p^* + p' \qquad u = u^* + u' \qquad v = v^* + v' \qquad w = w^* + w' \tag{81}$$

3)   solve for pressure correction, p', using the pressure correction equation and then calculate the correct pressure value from p^* and p'.

4)   next, solve for correct velocity components using correct pressure value p.

5)   the discretized transport equations such as thermal energy are solved using the correct pressure (ϕ) and velocity components, and are checked for convergence.

6)   the correct pressure and velocity components are treated as guessed values for the next iteration.

The above process continues until convergence is achieved. The SIMPLE scheme is illustrated in a flow chart, figure 4.2.
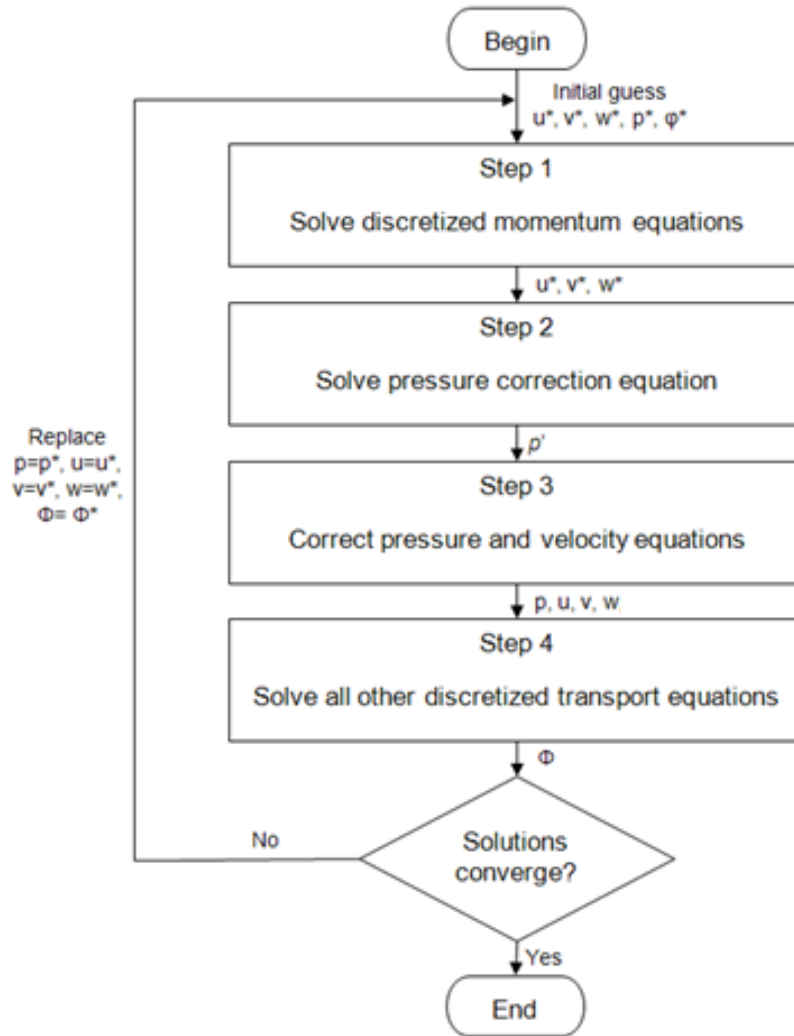
Figure 4.2 The SIMPLE algorithm

4.5   Boundary conditions for the computational domain

ANSYS-Fluent prescribes boundary conditions that specify the flow and thermal variables on the boundaries of the computational domain [12]. The following boundary conditions are used in this work.

- inlet mass flow rate

- pressure outlet

- radiator

- wall

4.5.1 Inlet mass flow rate

An inlet mass flow rate boundary condition is used to prescribe mass flow rate at the inlet plane of the fluid computational domain. Information pertaining to temperature, flow direction, and turbulence parameters of the fluid at the inlet plane are also provided in this boundary condition.

Since the standard k-ε model is used for turbulence modeling, turbulent kinetic energy and turbulent dissipation rate at the inlet plane are specified in terms of turbulence intensity and hydraulic diameter. The turbulent intensity is defined as the ratio of the root-mean-square of velocity fluctuations and average flow velocity. Turbulent intensity at the core of a fully developed flow is estimated using formula derived from an empirical correlation as:

$$I \equiv \frac{v'}{\bar{v}} = 0.16(Re_{Dh})^{1/8} \tag{82}$$

Hydraulic diameter is a physical quantity and equal to the characteristic length of the plane. For circular inlets, the diameter of the inlet plane is hydraulic diameter.

4.5.2 Outlet pressure

The outlet pressure boundary condition prescribes the pressure of fluid at the outlet plane of the domain. A pressure distribution in the plane can be defined using UDF.

4.5.3 Radiator

A radiator is an infinitely thin plane that causes a pressure drop in the fluid flowing through it. The pressure drop is proportional to the dynamic head of the fluid upstream:

$$\Delta P = K_L * \left(\frac{1}{2}\rho v^2\right) \tag{83}$$

where, K_L is the loss coefficient for radiator, ρ is density of the fluid, v is the streamwise velocity of fluid upstream of the radiator, and ΔP is the pressure drop across the radiator.

The loss coefficient is an input for ANSYS-Fluent and defines the pressure drop through the radiator.

4.5.4 Wall

A wall boundary condition is used to bind the fluid and solid domains. The wall boundary condition requires a wall motion condition, a shear condition, and a thermal boundary condition. The wall motion can be either stationary or moving. The shear stress condition for a wall can be specified as four kinds: no-slip, specified shear, and Marangoni stress. The no-slip condition indicates that the fluid adjacent to the wall sticks to the wall.

There are five thermal boundary conditions available for the wall: fixed heat flux, fixed temperature, convective heat transfer, external radiation heat transfer, and combined external radiation and convection heat transfer. The adiabatic wall can be defined by setting the heat flux equal to zero.

For a two-sided wall with, fluid or solid zones on both sides of the wall, a shadow zone is created in ANSYS-Fluent to treat each side of the wall as a different wall zone. These wall zones can be defined as coupled or uncoupled with each other. For coupled wall zones, the thermal boundary condition is not required, as ANSYS-Fluent calculates the heat transfer directly from the solution in the adjacent cells. For uncoupled wall zones, both zones are treated independently and different thermal boundary conditions can be given to them.

CHAPTER 5

THERMAL-FLUID AND STRUCTURAL RESULTS FOR STEADY STATE

This chapter contains the thermal-fluid and structural analyses results of the HPSH1 at full-load steady state operating condition. Flue gas velocity and pressure distributions in the HRSG are calculated prior to performing thermal-fluid analysis of the HPSH1.

5.1 Flue gas velocity and pressure distributions inside the HRSG

Flue gas pressure distribution at the HRSG outlet plane is calculated from the stack model. This calculated pressure distribution, figure 5.1, is used as the outlet boundary condition for the flue gas flow.
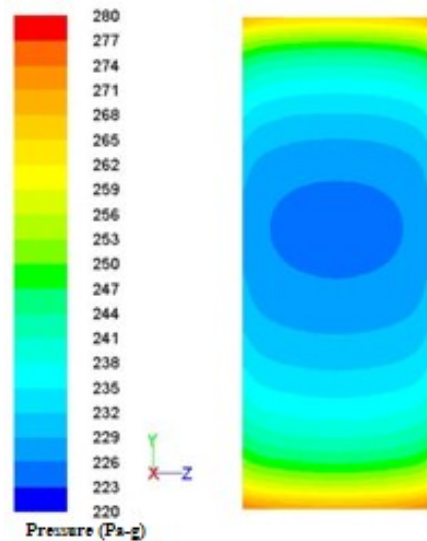
Figure 5.1 Flue gas pressure distribution at the HRSG outlet plane

The computed distribution of flue gas U-velocity (x-direction) component in the y-z plane 2.3 inches upstream of the HPSH1 is shown in figure 5.2.
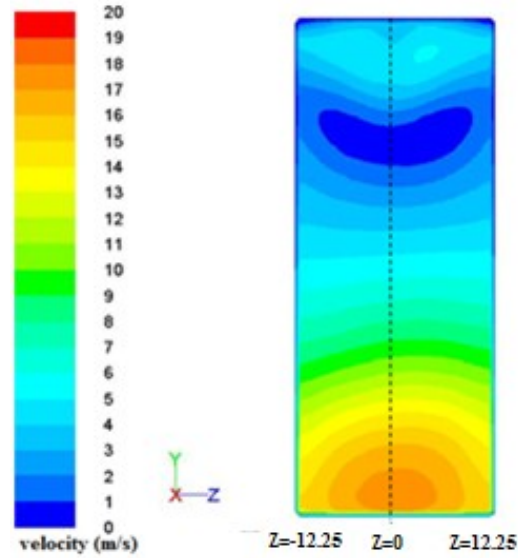
Figure 5.2 Computed flue gas U-velocity distribution just upstream of HPSH1

The y-profiles of U-velocity component at the HRSG middle, z=0 ft., and quarter, z=6 ft., in the upstream plane are shown in figure 5.3. It is observed that the velocity is non-uniform in the y-direction but uniform in the z-direction.
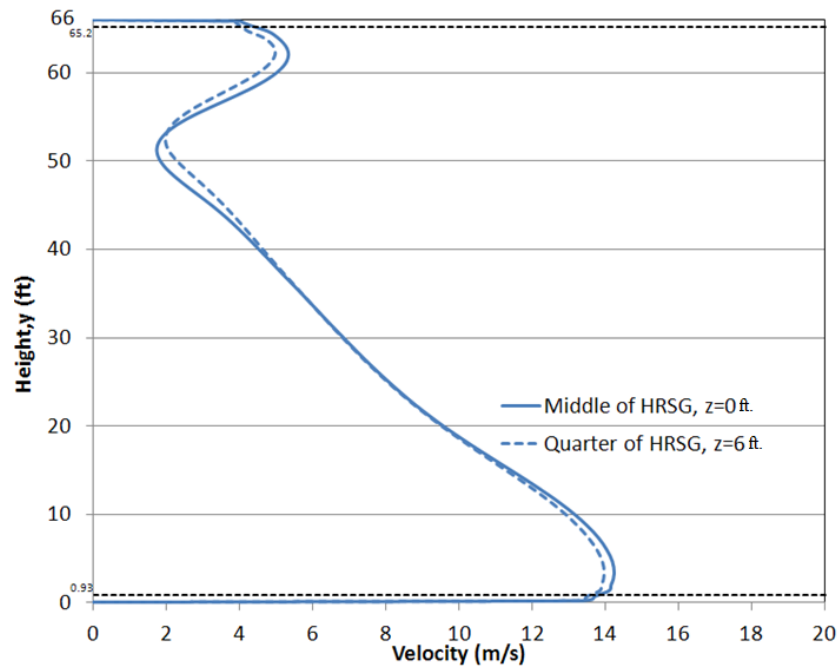
Figure 5.3 Flue gas U-velocity profiles just upstream of HPSH1

77

The horizontal dashed lines in figure 5.3, at y=0.93 ft. and y=65.20 ft., correspond to the locations of the partition planes for HPSH1 section model. The velocity values at y=65.5 ft. and y=0.5 ft. are used, respectively, as inlet boundary conditions for the inlet section and the outlet section. The velocity profile from y=0.93 ft. to 65.2 ft. is employed to calculate the outside (flue gas side) heat transfer coefficient for the harp tube section.

The flue gas pressure distribution in the y-z plane 2.3 inches downstream of the HPSH1 is shown in figure 5.4. The pressure y-profiles at the HRSG middle, z=0 ft., and quarter, z=6 ft., in the downstream plane are shown in figure 5.5. The pressure values at y=65.5 ft. and y=0.5 ft. are used, respectively, as outlet boundary conditions for the inlet section and the outlet section.
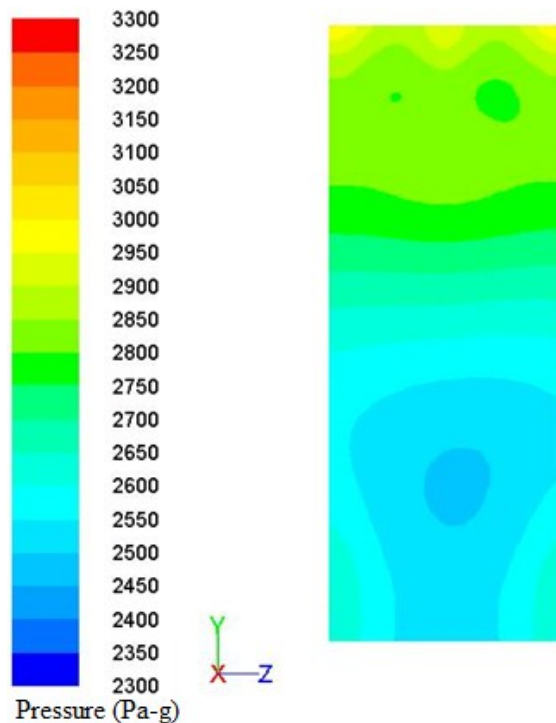
Figure 5.4 Flue gas pressure distribution just downstream of HPSH1

78
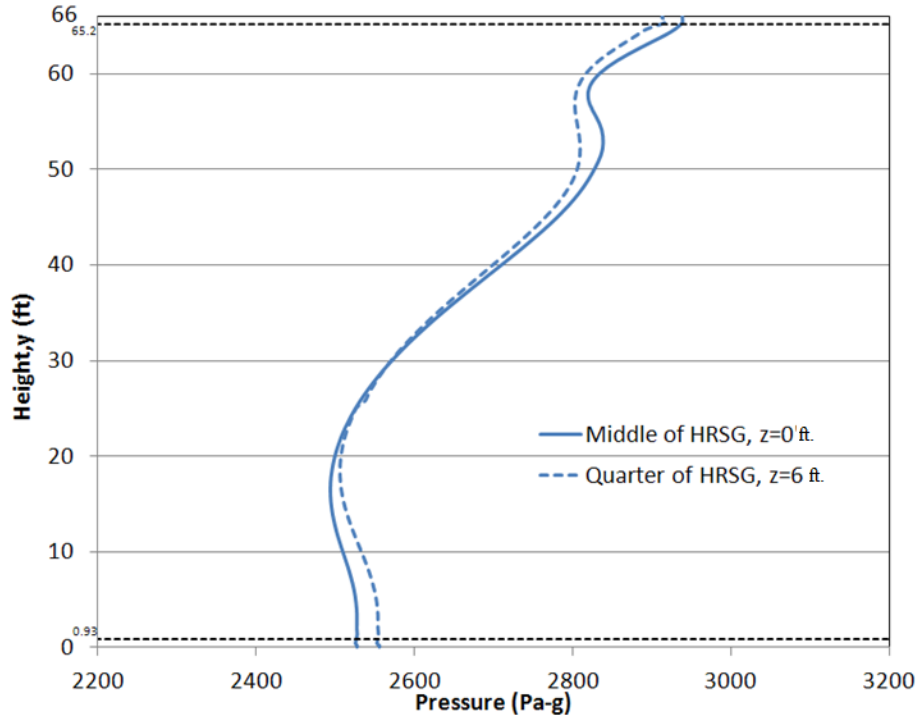
Figure 5.5 Flue gas pressure profiles just downstream of HPSH1

5.2 Thermal-fluid results of steam and flue gas for HPSH1

Thermal-fluid results of steam and flue gas for HPSH1 are obtained by solving the inlet section, harp tube section, and outlet section models. Results for each section are presented next.

5.2.1 Inlet section

The inlet section model contains fluid domains for steam and flue gas, and a solid domain for P-91 steel pipes. The steam velocity magnitude and pressure distributions in the section are shown in figures 5.6 and 5.7, respectively. The mass-weighted-average steam pressure for the section is calculated to be 7604917 Pa (g).

79

Flue gas velocity and temperature distributions for the inlet section are shown in figures 5.8 and figure 5.9, respectively. It is observed from these results that flue gas has lower velocity and temperature in the region above the baffles as compared to under the baffles.
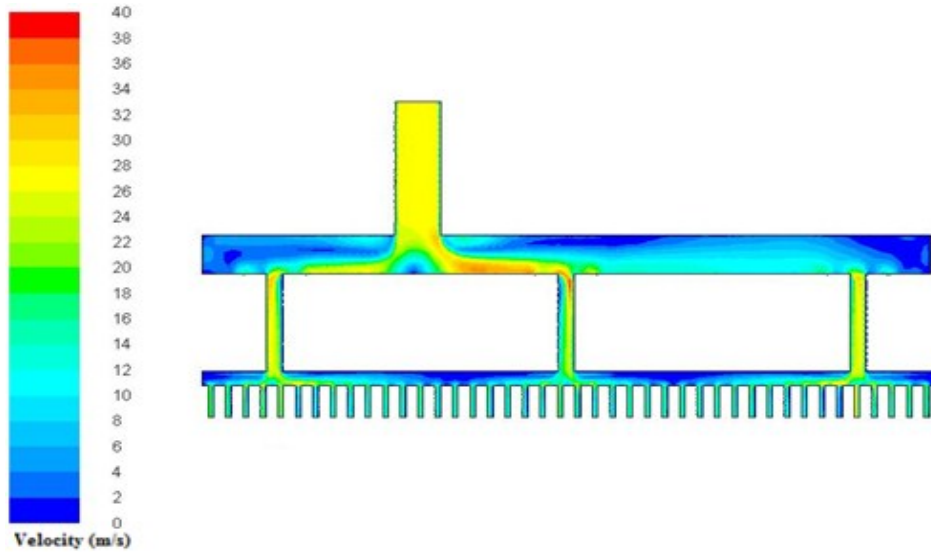
Figure 5.6 Steam velocity magnitude distribution in the inlet section
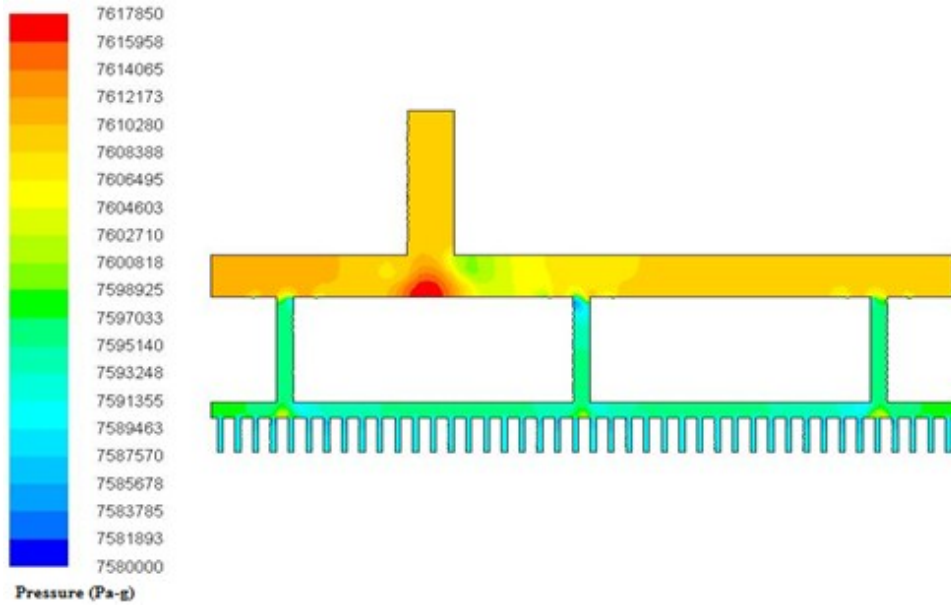
Figure 5.7 Steam pressure distribution in the inlet section

80
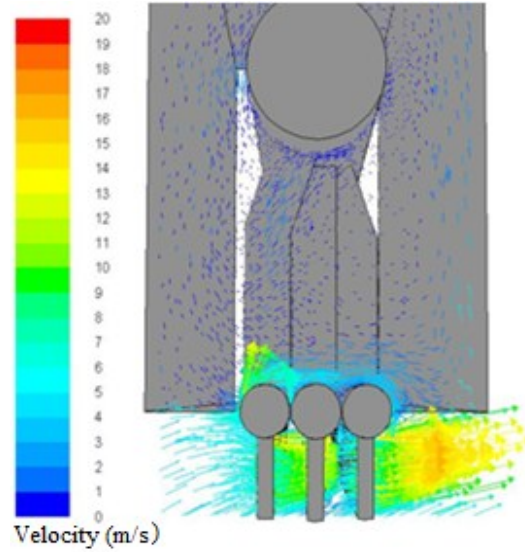
Figure 5.8 Flue gas velocity vectors for the inlet section
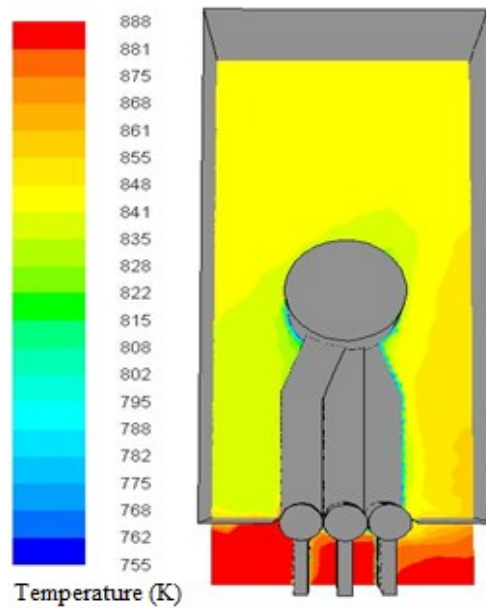
Figure 5.9 Flue gas temperature distribution for the inlet section

The inlet section results also contain steam mass flow rates through the unfinned length of harp tubes, figures 5.10 - 5.12. In these figures, the 1st tube is adjacent to the HRSG transverse (z) wall and the 42nd tube is in the middle of

HRSG (z=0 ft.), for each harp tube row. These mass flow rates are employed as inlet boundary conditions for the harp tube section model.
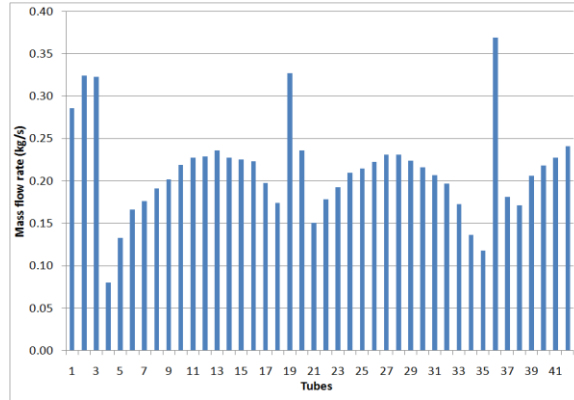
Figure 5.10 Steam mass flow rates through first row harp tubes
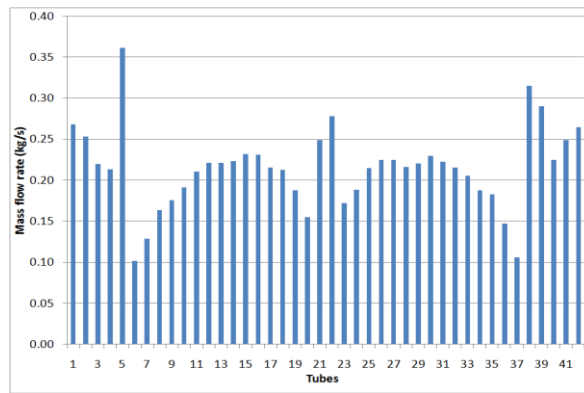
Figure 5.11 Steam mass flow rates through second row harp tubes
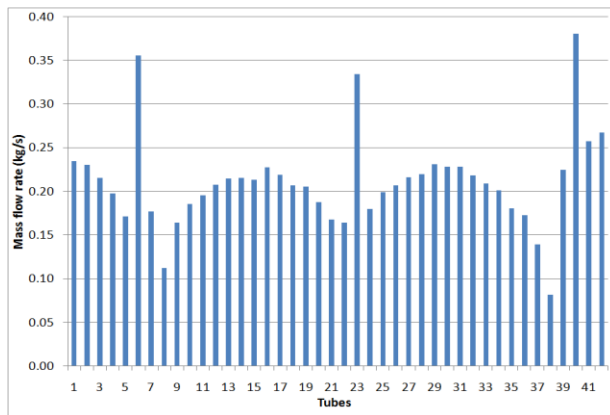
Figure 5.12 Steam mass flow rates through third row harp tubes

The inside and outside wall temperature distributions for the inlet section components are shown in figure 5.13. The headers are observed to be hotter compared to other components. This is because of higher flue gas temperature and velocity around the headers. These temperature distributions are to be the main inputs for the subsequent structural analysis.
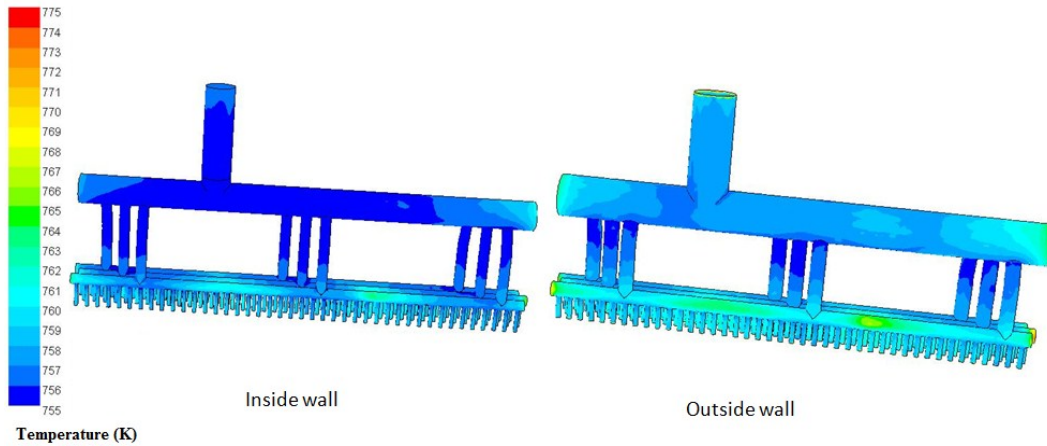
Figure 5.13 Inside and outside wall temperature distributions for the inlet section

The mass-weighted-average steam temperature at the exit of the inlet section is calculated to be 755.5 K.

5.2.2 Harp tube section

The harp tube section model has a fluid domain for steam and a solid domain for P-91 steel. The equivalent outside heat transfer coefficient for the harp tubes is calculated from the flue gas velocity distribution upstream of HPSH1, as obtained from the HRSG model solution. A polynomial fit to the heat transfer coefficient along the tube length (y-direction) is used, figure 5.14.
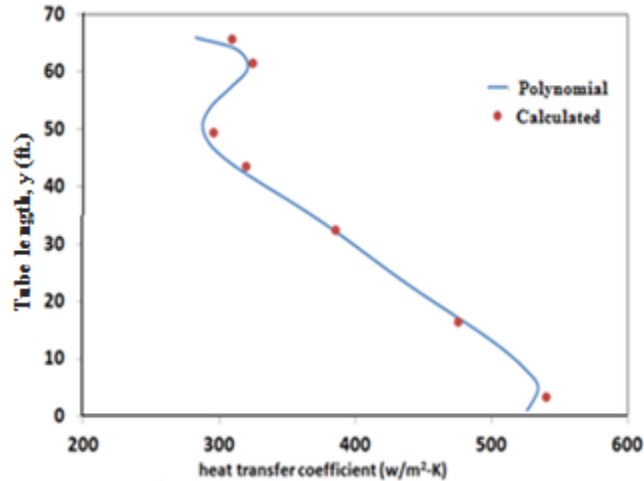
Figure 5.14 Equivalent outside heat transfer coefficient for the harp tubes

Harp tubes are solved for two different cases: uniform flue gas temperature along the tube length and non-uniform flue gas temperature along the tube length. Results for these two cases are presented in following sections.

5.2.2.1 Uniform flue gas temperature along tube length

The uniform, along the tube length, flue gas temperature for each harp tube row is calculated from an overall heat balance between the steam and flue gas. The calculated flue gas temperature values are provided in table 5.1.

Row	Flue gas temperature (K)
1	883.00
2	876.30
3	868.00

Table 5.1 Uniform flue gas temperature for harp tube rows

Using these uniform flue gas temperature values, thermal-fluid results are obtained by solving the harp tube section model. The mass-weighted-average

84

steam temperature profiles, and the inside and outside tube wall temperature profiles along the length (y) for the 42nd tube of each harp tube row are shown in figures 5.15 - 5.17.
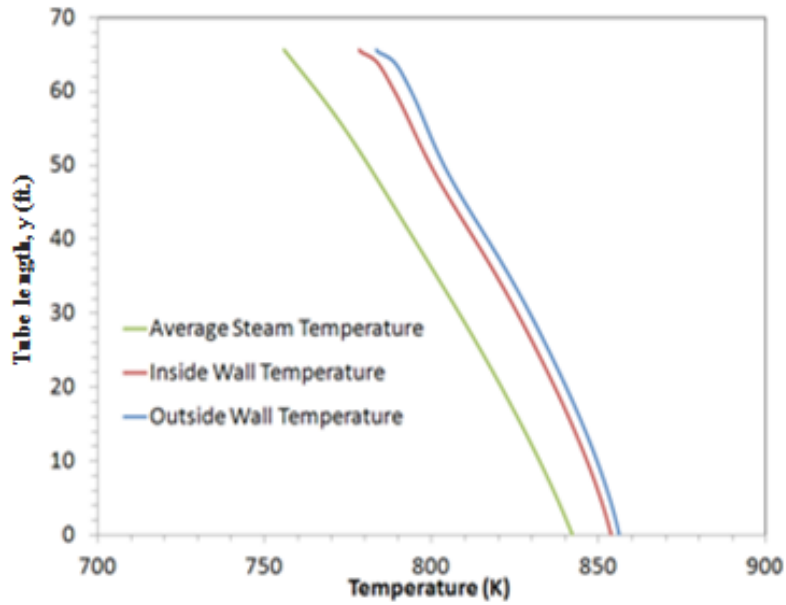
Figure 5.15 Results for the 42nd tube of row 1 with uniform flue gas temperature
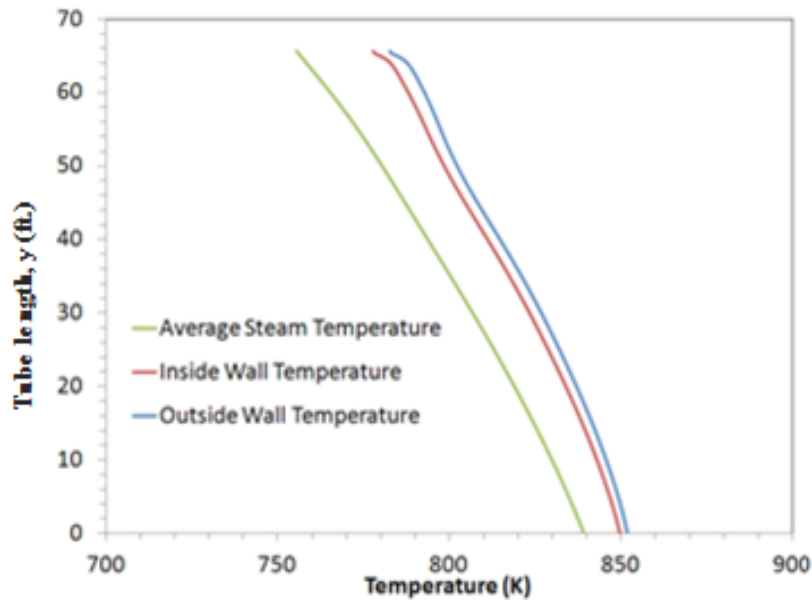
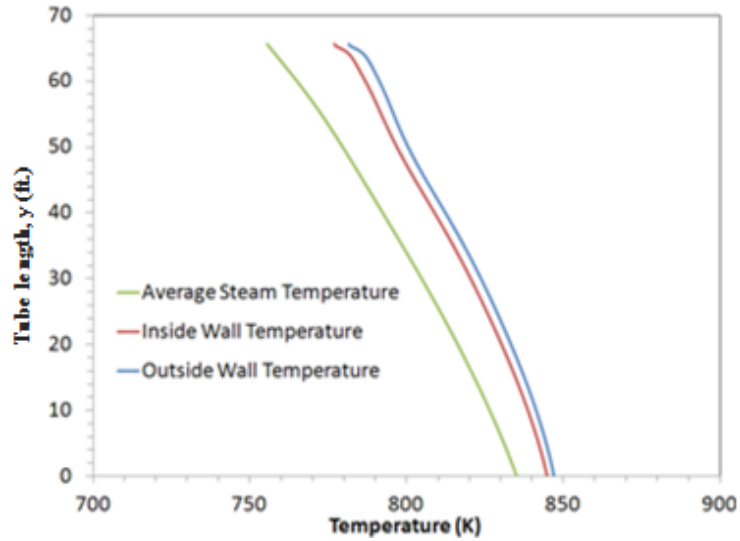Figure 5.16 Results for the 42nd tube of row 2 with uniform flue gas temperature

Figure 5.17 Results for the 42nd tube of row 3 with uniform flue gas temperature

Mass-weighted-average steam temperatures at the exit of the tubes for each row are shown in figures 5.18 - 5.20. These temperatures serve as inlet boundary conditions for the HPSH1 outlet section model.

The mass-weighted-average steam temperature at the tubes (42x3) exit of the harp tube section obtained with uniform flue gas temperature along the tube length is calculated to be 841.0 K.
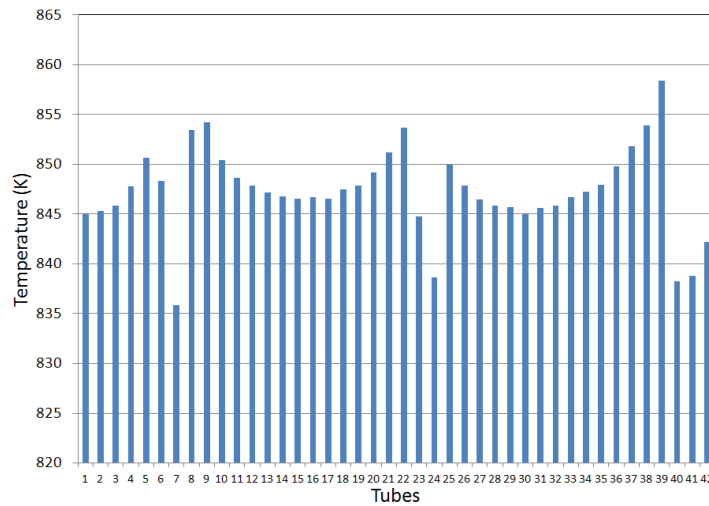
Figure 5.18 Average steam temperatures at the exit of row 1 harp tubes
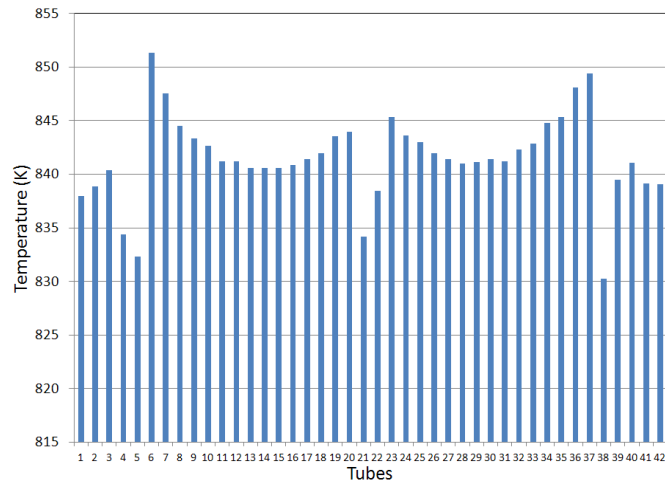
Figure 5.19 Average steam temperatures at the exit of row 2 harp tubes
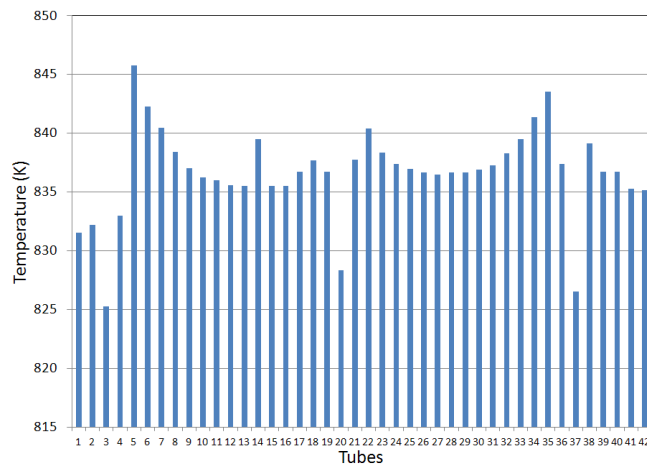
Figure 5.20 Average steam temperatures at the exit of row 3 harp tubes

5.2.2.2 Non-uniform flue gas temperature along tube length

The non-uniform flue gas temperature distribution in the HPSH1 region is calculated using the Fluent-NTU model.

Four y-z planes, one each upstream of row 1, 2, 3, and one downstream of row 3, are shown in figure 5.21. The flue gas temperature distributions on these four planes are depicted in figure 5.22.
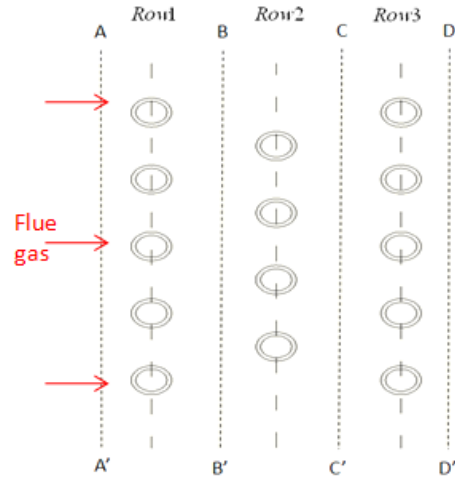
Figure 5.21 Four y-z planes in the HPSH1 region
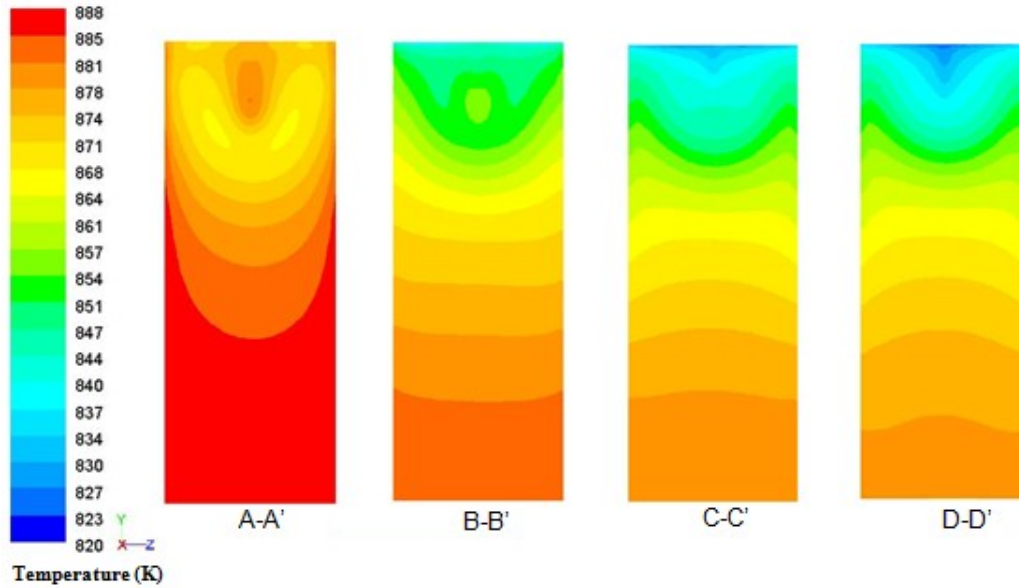
Figure 5.22 Flue gas temperature distributions in the HPSH1 region

Flue gas temperature profiles along y-direction, i.e. the tube length, for the 42nd harp tube of each row are shown in figure 5.23.

Using these non-uniform gas temperature profiles, thermal-fluid results for steam are obtained by solving the harp tube section model.
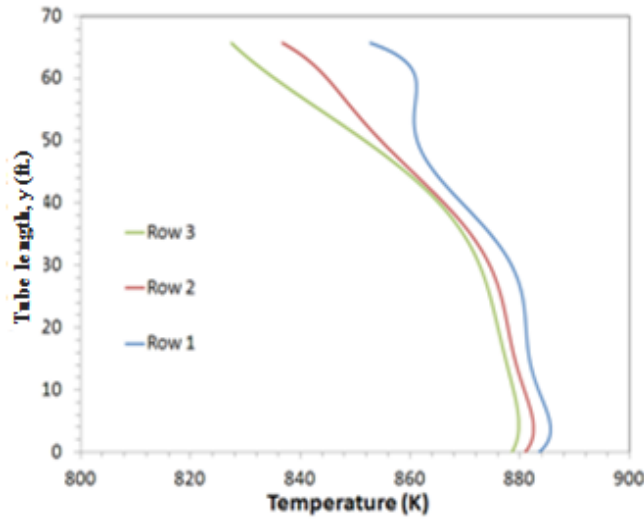
88

Figure 5.23 Flue gas temperature profiles for the 42nd harp tube of each row

The mass-weighted-average steam temperature profiles, and the inside and outside tube wall temperature profiles along the length for the 42nd harp tube of each row are shown in figures 5.24 – 5.26.

The mass-weighted-average steam temperature at tubes (42x3) exit of the harp tube section obtained with non-uniform flue gas temperature along the tube length is calculated to be 841.7 K.
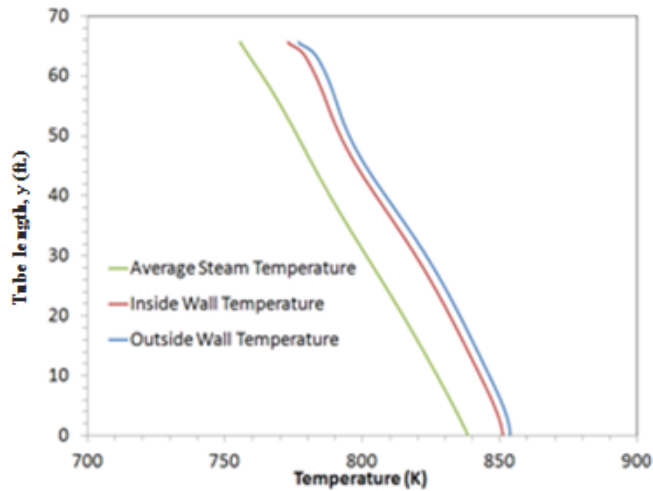

Figure 5.24 Results for the 42nd tube-row 1 with non-uniform flue gas temperature
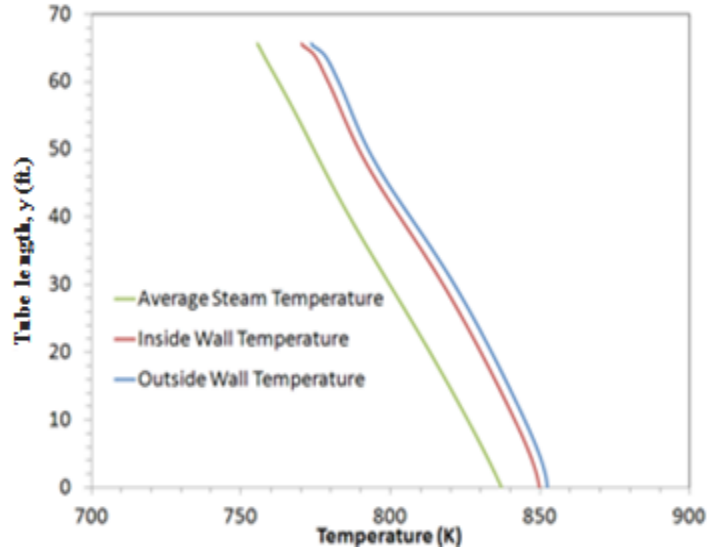
89

Figure 5.25 Results for the 42nd tube-row 2 with non-uniform flue gas temperature
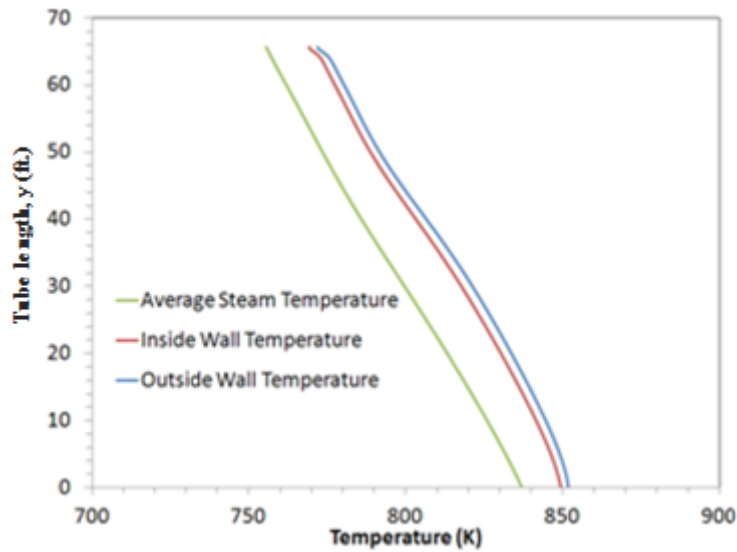

Figure 5.26 Results of the 42nd tube-row 3 with non-uniform flue gas temperature

It is seen from the results that the mass-weighted-average steam temperatures at the exit of harp tubes (42x3) obtained from two cases differ by ±1 percent. The results also confirm that the mass-weighted-average steam temperature at the exit of harp tubes is highest for the first tube row and lowest for

the third tube row. This is due to a gradual temperature drop in flue gas as it flows over the rows.

The mass-weighted-average steam pressure profile along the tube length for the 42nd tube of row 1 is shown in figure 5.27. The mass-weighted-average steam pressure for all tubes (42x3) of the harp tube section is calculated to be 7580 kPa (g).
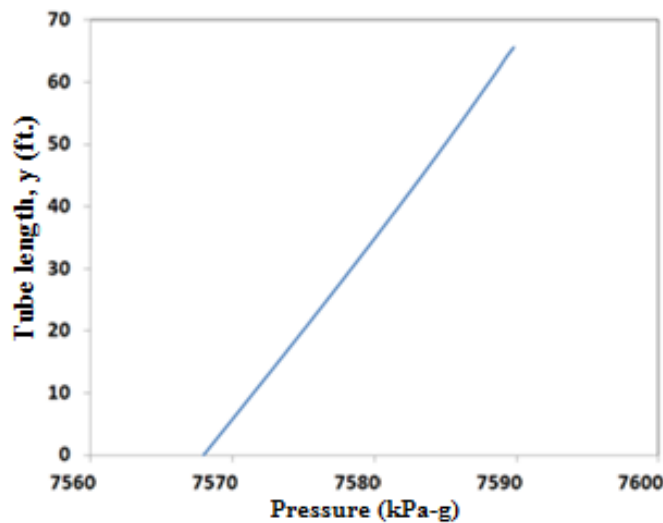

Figure 5.27 Steam pressure for the 42nd tube of harp tube row 1

5.2.1 Outlet section

The outlet section model has fluid domains for steam and flue gas, and a solid domain for P-91 steel. Results obtained from the harp tube section solution with uniform flue gas temperature approach were used as inlet boundary conditions for the outlet section.

Steam velocity magnitude and pressure distributions in the outlet section are shown in figures 5.28 and 5.29, respectively. The mass-weighted-average steam pressure for the section is calculated to be 7652 kPa (g).
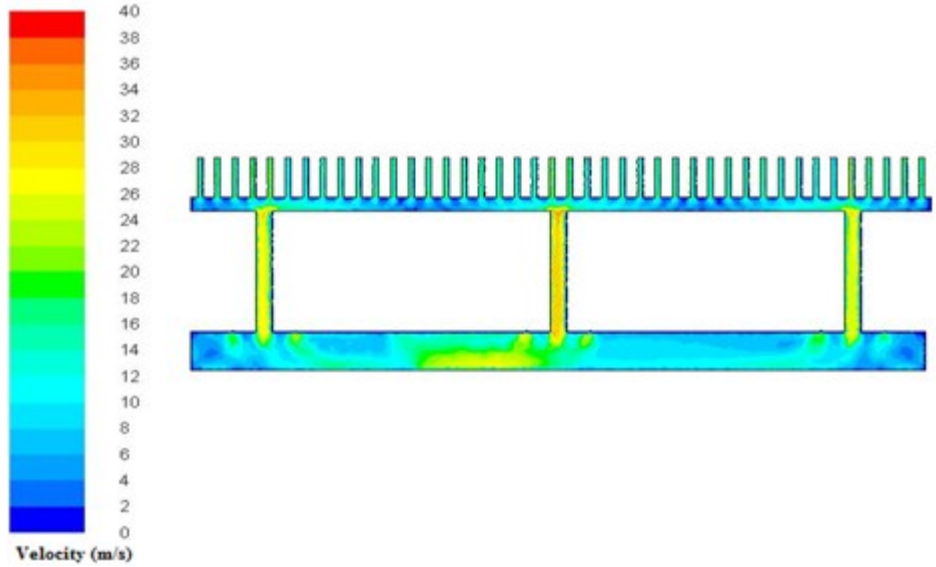
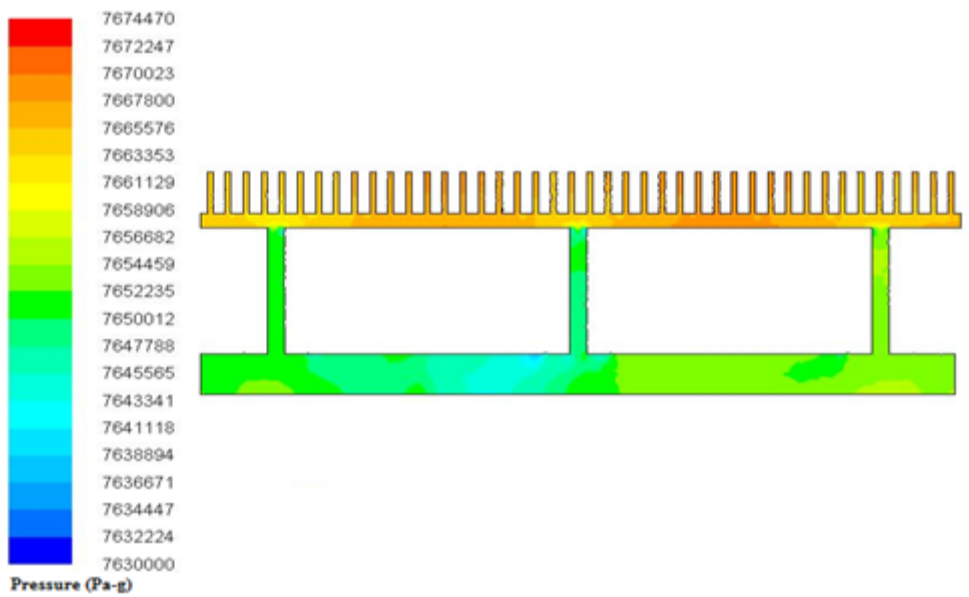Figure 5.28 Steam velocity magnitude distribution in the outlet section

Figure 5.29 Steam pressure distribution in the outlet section

Flue gas velocity and temperature distributions for the outlet section are shown in figures 5.30 and 5.31, respectively. It is observed that flue gas is cooler in the region below the section baffles.
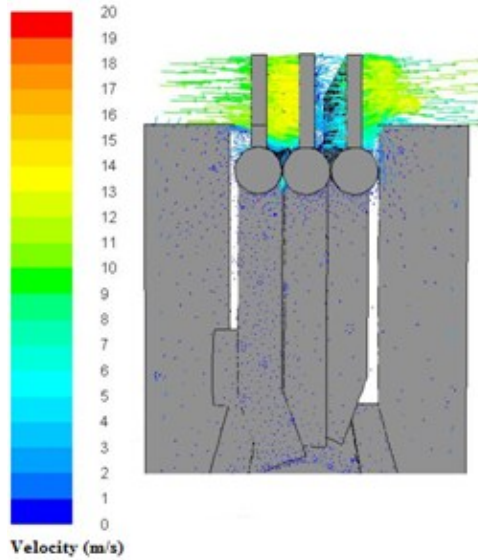
92

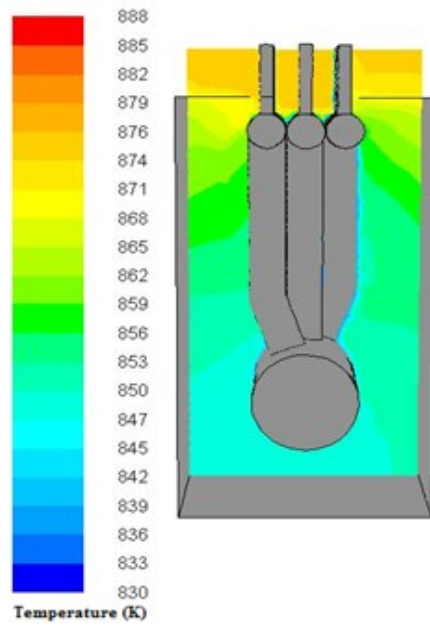Figure 5.30 Flue gas velocity distribution for the outlet section

Figure 5.31 Flue gas temperature distribution for the outlet section

The inside and outside wall temperature distributions for the outlet section

components are shown in figure 5.32. It is observed that the header and links of

the first row are hotter compared to the second and third row headers and links.

This is due to the higher steam temperature at the exit of the first tube row. These

temperature distributions are to be the main inputs for the subsequent structural analysis.
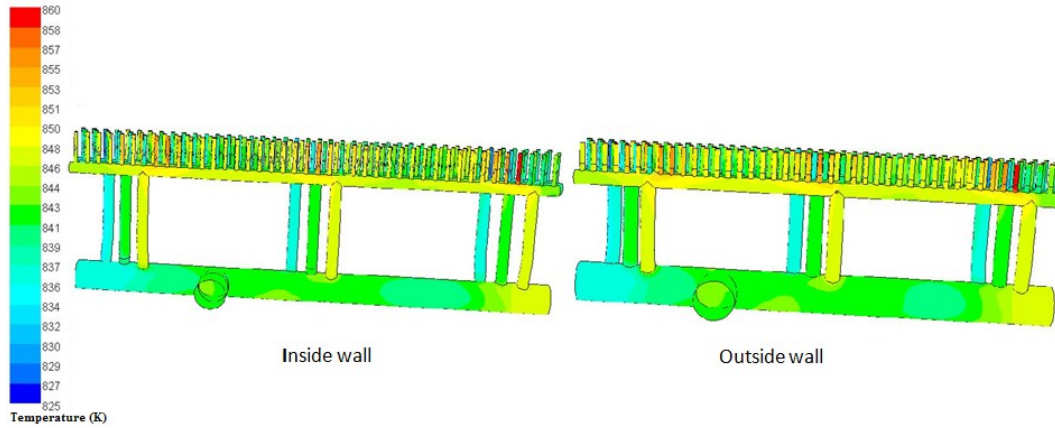

Figure 5.32 Inside and outside wall temperature distributions for the outlet section

The mass-weighted-average steam temperature at the exit of the outlet section is calculated to be 841.5 K; this is in good agreement with the plant-measured value of 840 K.

The calculated outside wall temperature values at the specific locations of the inlet links and outlet manifold are found in good agreement with the plant-measured temperature values, figures 5.33 – 5.34.
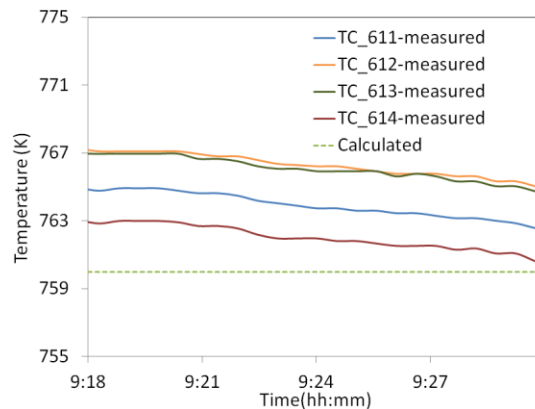

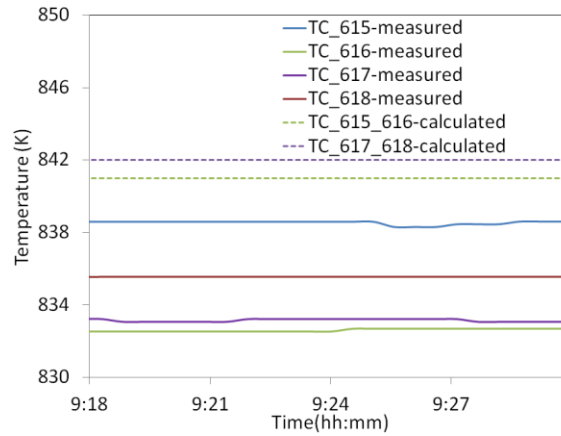Figure 5.33 Outside wall temperature values of the inlet links

Figure 5.34 Outside wall temperature values of the outlet manifold

5.3 Structural results for HPSH1

Structural analysis is carried out for one symmetrical half of the HPSH1 assembly using the NX/Nastran FEA tool. The manifolds, links, headers, and the unfinned portion of the harp tubes are discretized using tetrahedral elements, and the finned harp tubes are discretized using one-dimensional beam elements. The HPSH1 structure is considered to expand freely in x- and z-directions, and fixed in the y-direction. The plant structure hangs by two supports on the inlet manifold.

First, a thermal conduction analysis is performed based on the inside and outside wall temperature distributions obtained from the thermal-fluid analysis. Next, structural analysis is carried out using the thermal conduction analysis results and steam pressure. The mass-weighted-average steam pressure values, obtained from the thermal-fluid analysis, and are different but uniform for the inlet section, harp tube section and outlet section of HPSH1.

The von-Mises (effective) stress distributions for the inlet and outlet section components are shown in figure 5.35 and 5.36, respectively.
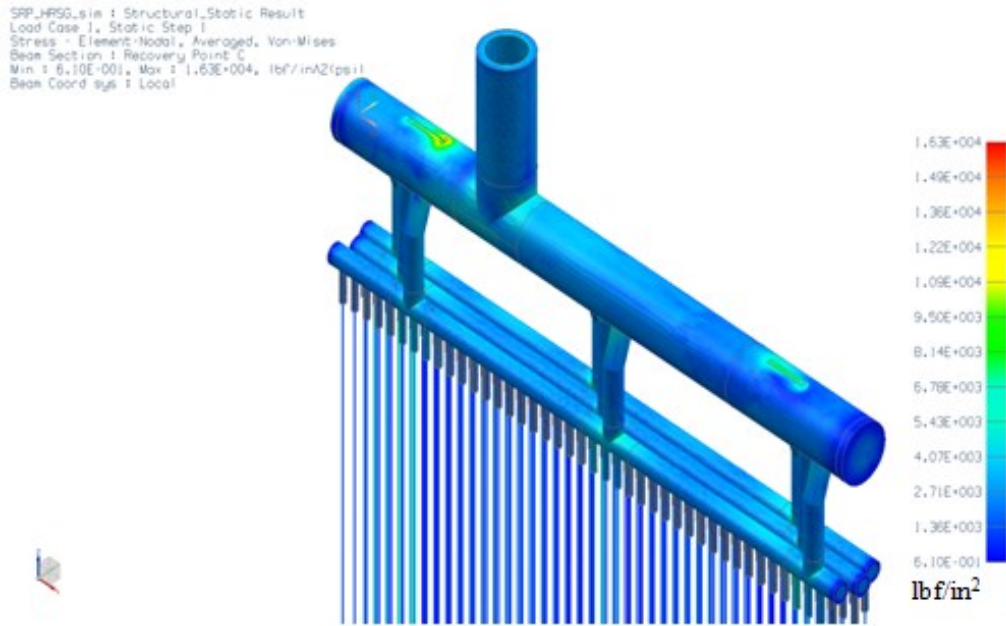

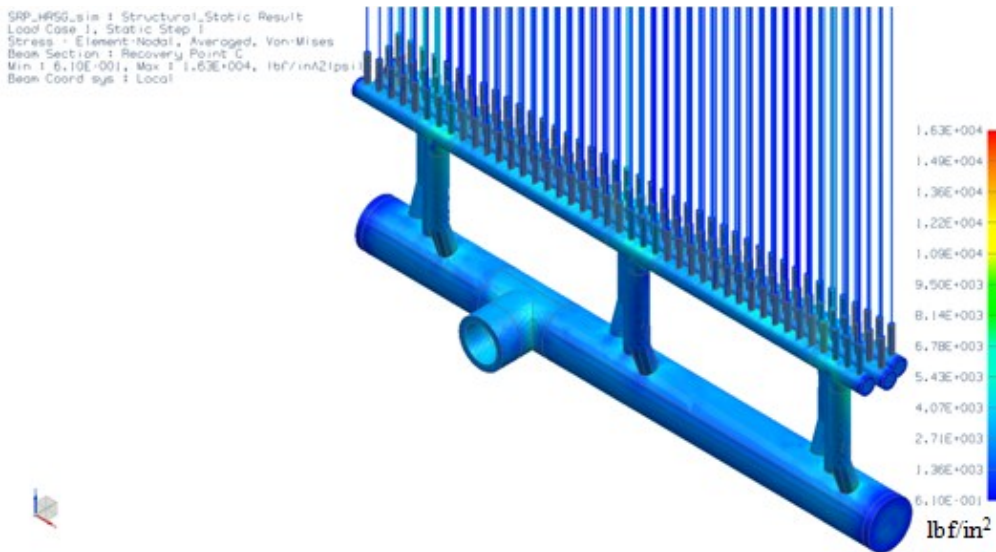Figure 5.35 Structural von-Mises stress distribution for the inlet section

Figure 5.36 Structural von-Mises stress distribution for the outlet section

The peak effective stress for the inlet section is located at the connecting region between the manifold and the links, and is calculated to be 12.47 ksi (klbf/in2), figure 5.37. For the outlet section, peak effective stress is located at the connecting region between the first header and the 3rd harp tube, and is calculated to be 12.49 ksi, figure 5.38.
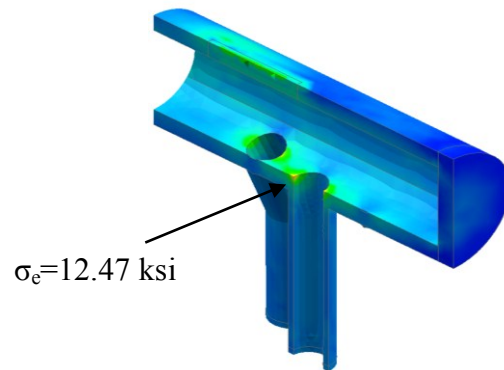

σ_e=12.47 ksi

Figure 5.37 Peak effective stress location and value for the inlet section
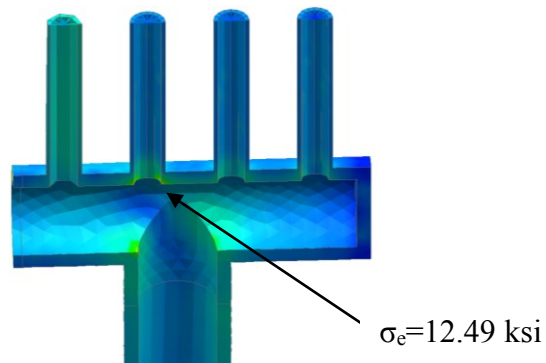

σ_e=12.49 ksi

Figure 5.38 Peak effective stress location and value for the outlet section

Factors of safety for the HPSH1 assembly are calculated to be 4.8 and 6.8 based on the yield and tensile strength, respectively. These are well above their minimum values.

CHAPTER 6

THERMAL-FLUID RESULTS FOR COLD START-UP TRANSIENT

This chapter presents HPSH1 transient thermal-fluid analysis results for the cold start-up operating condition. The transient solution is calculated for a time interval of 9930 seconds with one second time step. Flue gas velocity and pressure distributions in the HRSG are calculated prior to performing steam-side thermal-fluid analysis.

6.1 Flue gas velocity and pressure distributions inside the HRSG

Flue gas mass flow rate at the HRSG inlet is maintained at 240 kg/s for the initial 7800 seconds of the transient and gradually rises to the value of 395 kg/s (the eventual steady state) during the interval t=7800 second to t= 9540 second (points 1 and 2 in figure 6.1).
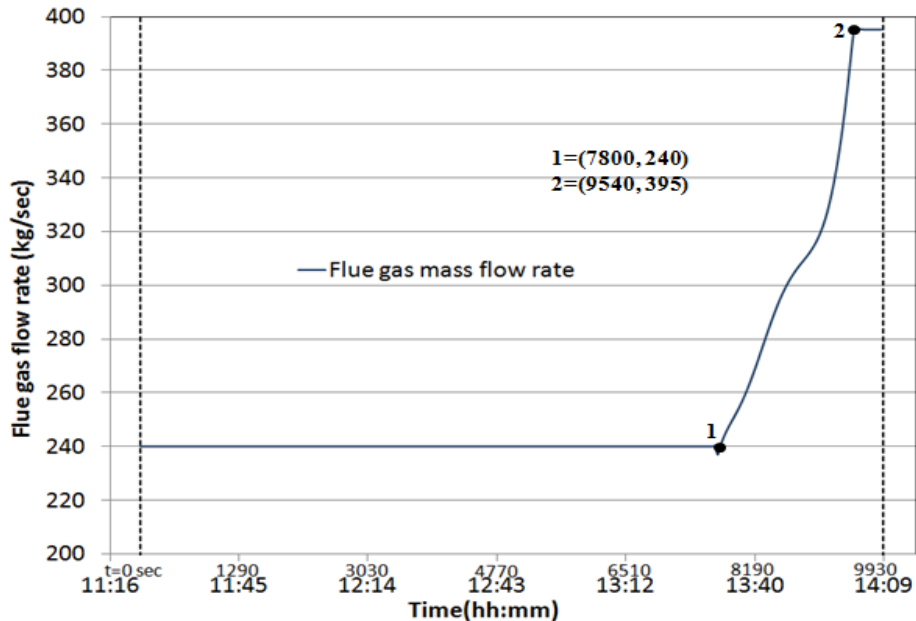

Figure 6.1 Flue gas mass flow rate at HRSG inlet for cold start-up operating condition

Flue gas velocity and pressure distributions for the initial 7800 seconds are calculated as the steady state solution of the HRSG and stack models with the flue gas mass flow rate of 240 kg/s. This solution is used as the initial condition for the transient calculations from t = 7800 second to t = 9930 second.

The calculated flue gas pressure distributions at the HRSG outlet plane corresponding to points 1 and 2 are shown as profiles 1 and 2, figure 6.2.
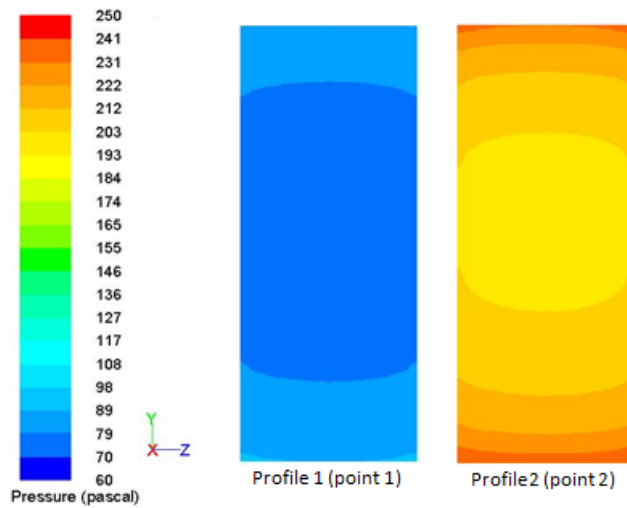

Figure 6.2 Flue gas pressure distributions at the HRSG outlet plane

Figures 6.3 and 6.4 show y-profiles of flue gas U-velocity component 2.3 inches upstream and pressure 2.3 inches downstream of the HPSH1 , respectively, as obtained from steady state solution using the pressure profiles 1 and 2 at the HRSG outlet plane at 395 kg/s mass flow rate. The velocity distribution in the HPSH1 region remains essentially the same for the two outlet plane pressure profiles but the pressure distribution does vary. It is further observed from the steady state analysis of the HPSH1 section models that the variation in the flue gas pressure downstream of the HPSH1, which is input to the section models,

does not make difference to the components wall temperature distributions. As such, the flue gas pressure distribution at the HRSG outlet is assumed to be invariant for the transient calculations. A user defined function is used to describe the time dependence of flue gas mass flow rate at the HRSG inlet.
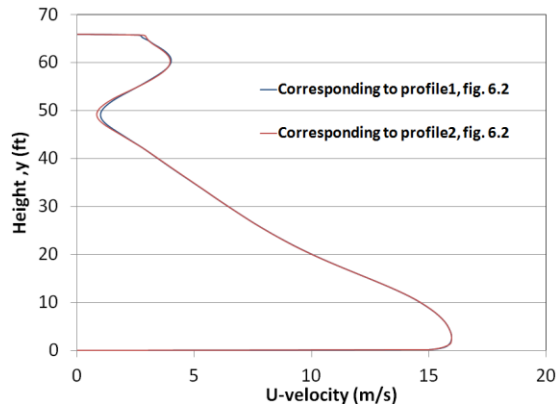
Figure 6.3 Flue gas U-velocity profiles just upstream of HPSH1

Figure 6.4 Flue gas pressure profiles just downstream of HPSH1

The computed y-profiles of flue gas U-velocity component at 2.3 inches upstream of HPSH1 at the HRSG mid-plane, z=0 ft., and quarter-plane, z=6.1 ft., for different time instants are shown in figure 6.5. The horizontal dotted lines in figure 6.4, at y=65.5 ft. and y=0.93 ft., correspond to the locations of partition

planes for the HPSH1 section model. It is observed that the U-velocity is uniform in the z-direction but non-uniform in the y-direction.

The flue gas velocity profiles upstream of the HPSH1 inlet and outlet sections are shown in figures 6.6 and 6.7, respectively. The velocity values at y=65.5 ft. and y=0.5 ft. are used, respectively, as inlet boundary conditions for the transient analysis of the inlet and outlet sections. The velocity profiles from y=0.93 ft. to y=65.2 ft. are used to calculate the flue gas side heat transfer coefficient for the harp tube section transient analysis.
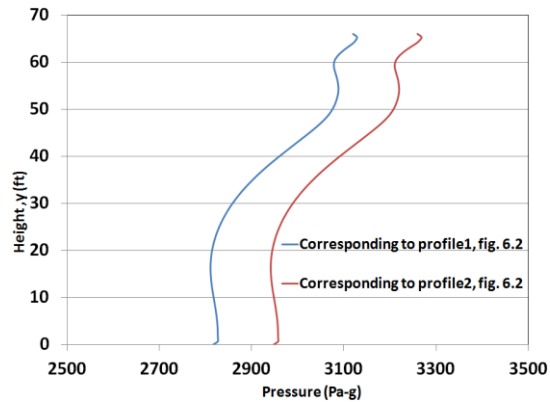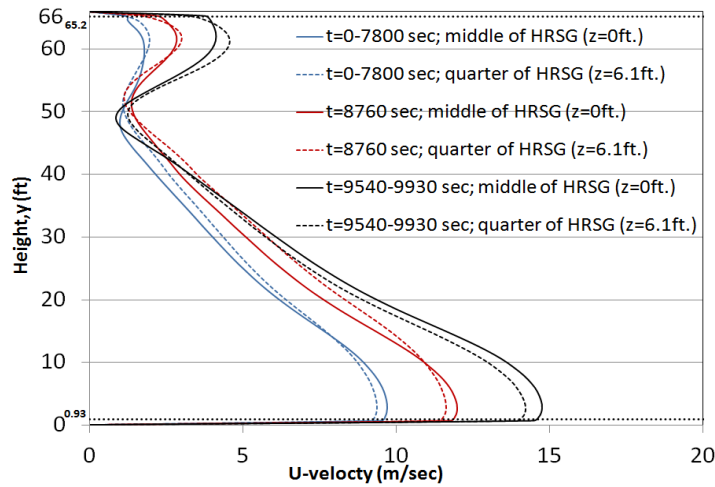
Figure 6.5 Flue gas U-velocity profiles just upstream of HPSH1
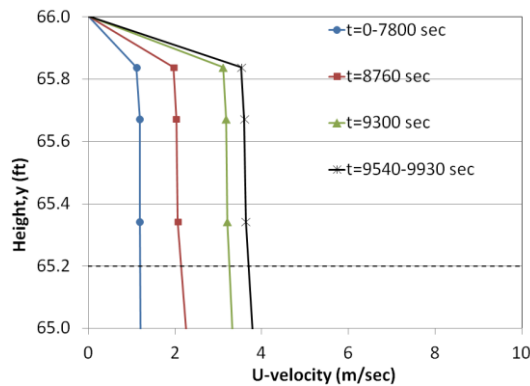
Figure 6.6 Flue gas U-velocity profiles just upstream of the HPSH1 inlet section

101
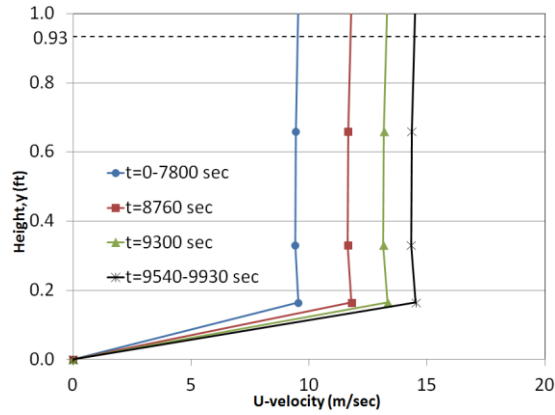
Figure 6.7 Flue gas U-velocity profiles just upstream of the HPSH1 outlet section

The flue gas pressure y-profiles at 2.3 inches downstream of HPSH1 at the HRSG mid-plane, z=0 ft., and quarter-plane, z=6.1 ft., for different time instants are shown in figure 6.8.

Figure 6.8 Flue gas pressure y-profiles 2.3 inches downstream of HPSH1

The pressure profiles 2.3 inches downstream of the inlet and outlet sections are shown in figures 6.9 and 6.10, respectively. The pressure values at y = 65.5 ft. and y = 0.5 ft. are used, respectively, as outlet boundary conditions for the transient analysis of the HPSH1 inlet and outlet sections.
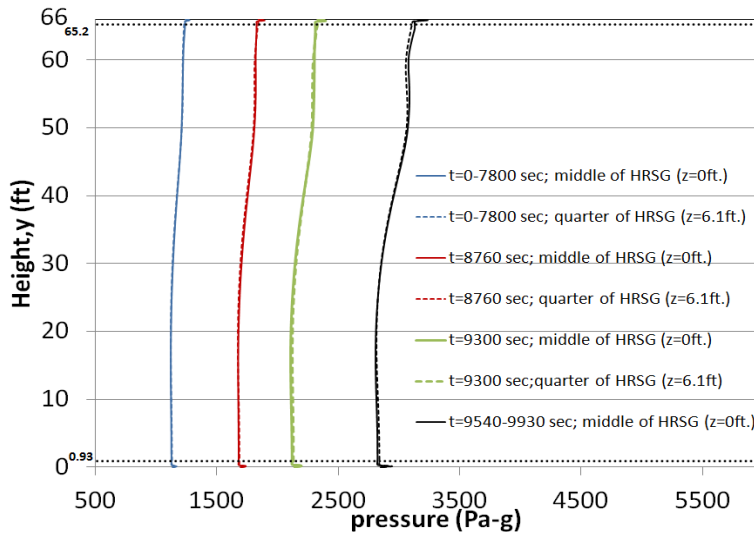
102
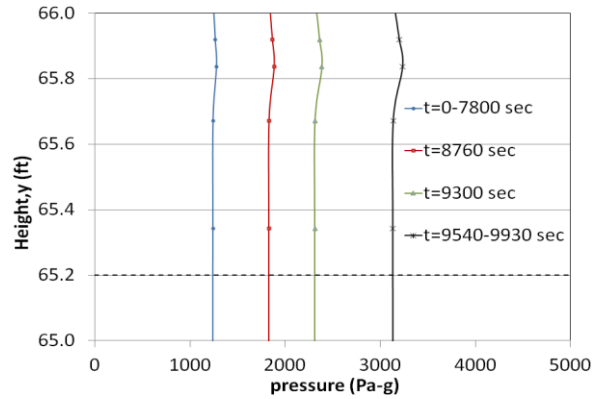
Figure 6.9 Flue gas pressure profiles 2.3 inches downstream of the inlet section
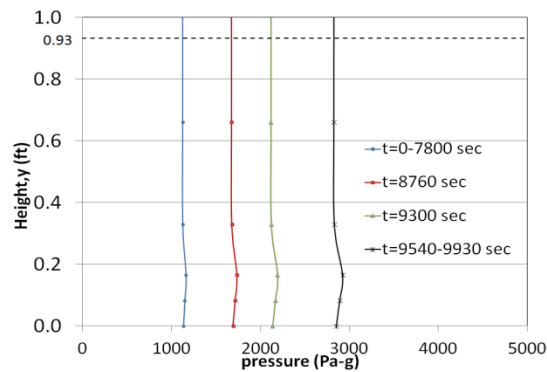
Figure 6.10 Flue gas pressure profiles 2.3 inches downstream of the outlet section

6.2 Thermal-fluid results of flue gas and steam for HPSH1

Thermal-fluid results of flue gas and steam are obtained by solving the HPSH1 inlet section, harp tube section, and outlet section models for the cold start-up condition. The results for each section are presented next.

6.2.1 Inlet section

As stated earlier, the initial condition for the inlet section is obtained from steady state solution corresponding to the operating condition at t=0 second. The steam temperature, and wall inside and outside temperature distributions for the components at t = 0 second are shown in figures 6.11 and 6.12, respectively.

103
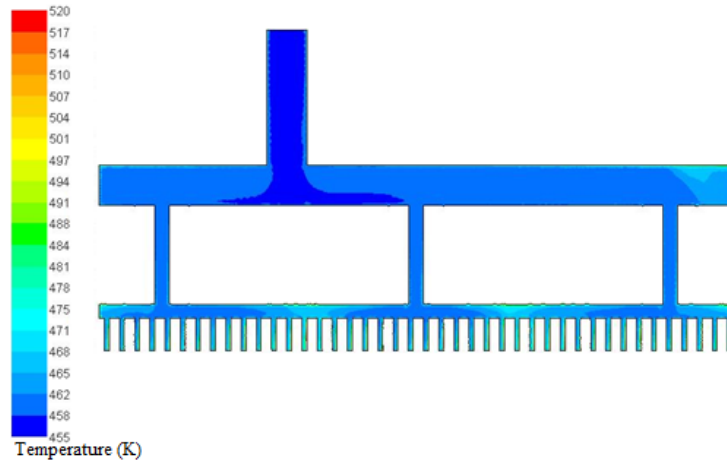
Figure 6.11 Steam temperature distribution in the inlet section at t=0 second
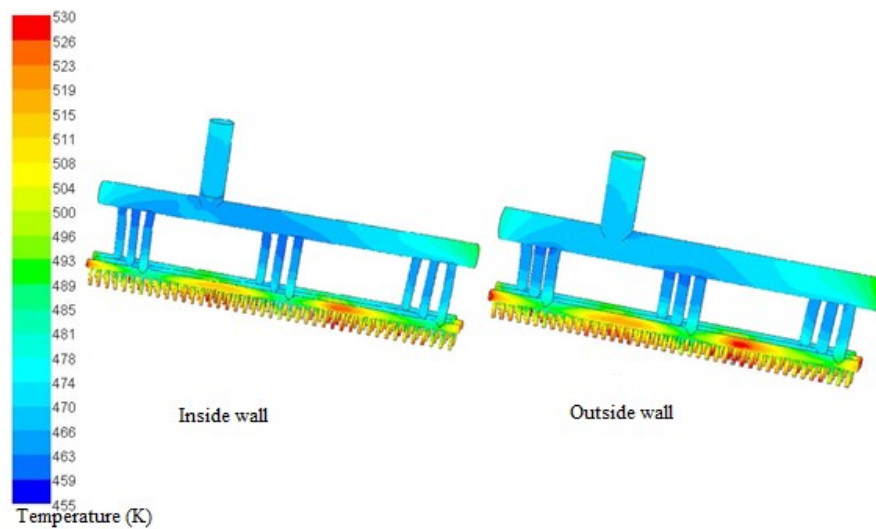
Figure 6.12 Inlet section components wall temperature distributions at t=0 second

User-defined functions are constructed to define the time-dependent boundary conditions for the inlet section during transient analysis.

The computed steam mass flow rates at the exit of unfinned length of rows 1, 2, and 3 tubes of the inlet section are shown in figures 6.13 – 6.15.

The mass-weighted-average steam temperatures at the exit of unfinned length of tubes of the inlet section are shown in figure 6.16. These time series

104

plots are employed as inlet boundary conditions for solving the harp tube section model.
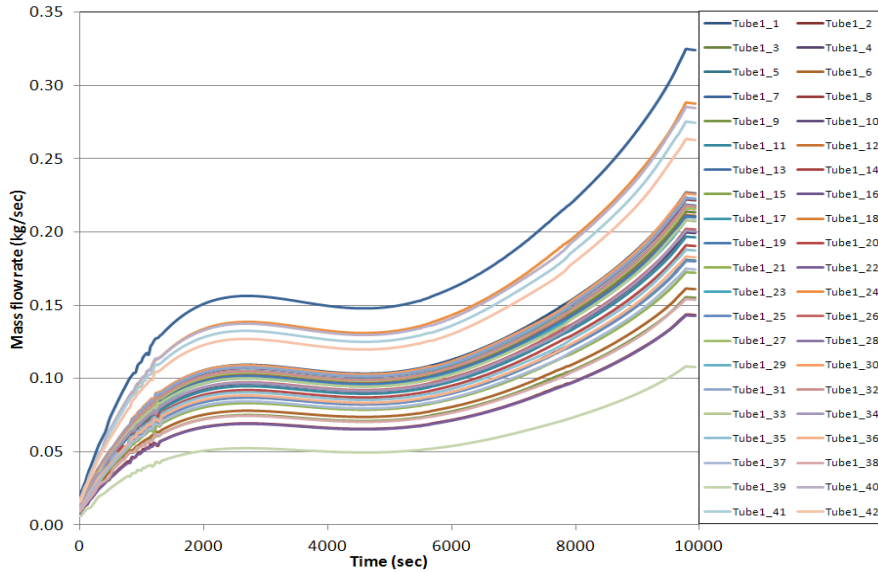
Figure 6.13 Steam mass flow rates at the exit of unfinned length of row 1 tubes – inlet section
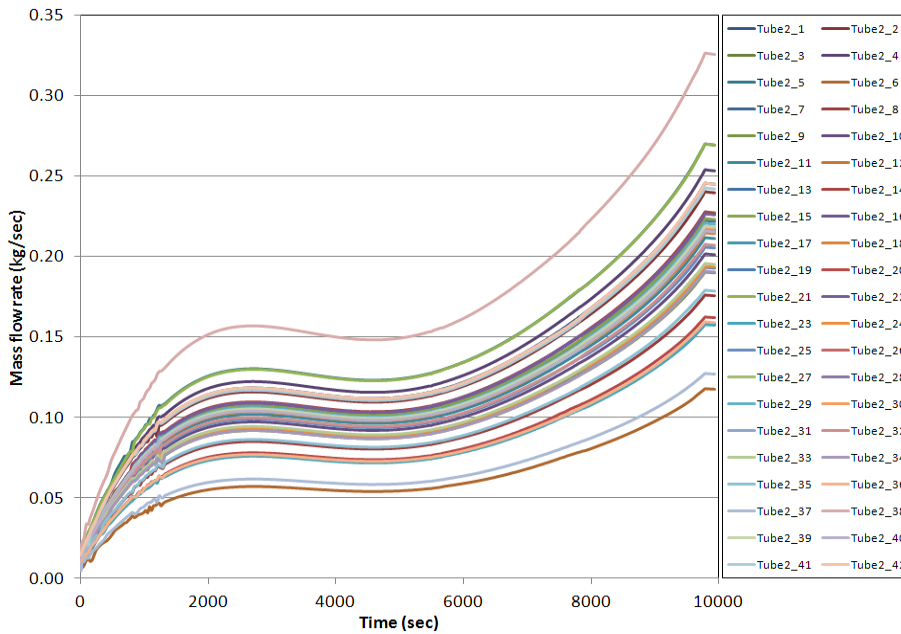
Figure 6.14 Steam mass flow rates at the exit of unfinned length of row 2 tubes – inlet section
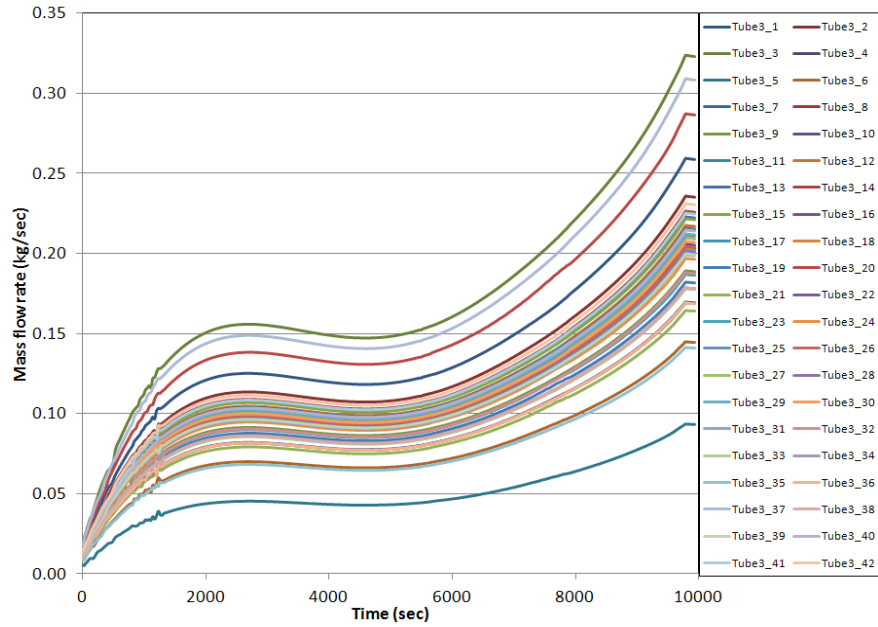
Figure 6.15 Steam mass flow rates at the exit of unfinned length of row 3 tubes – inlet section
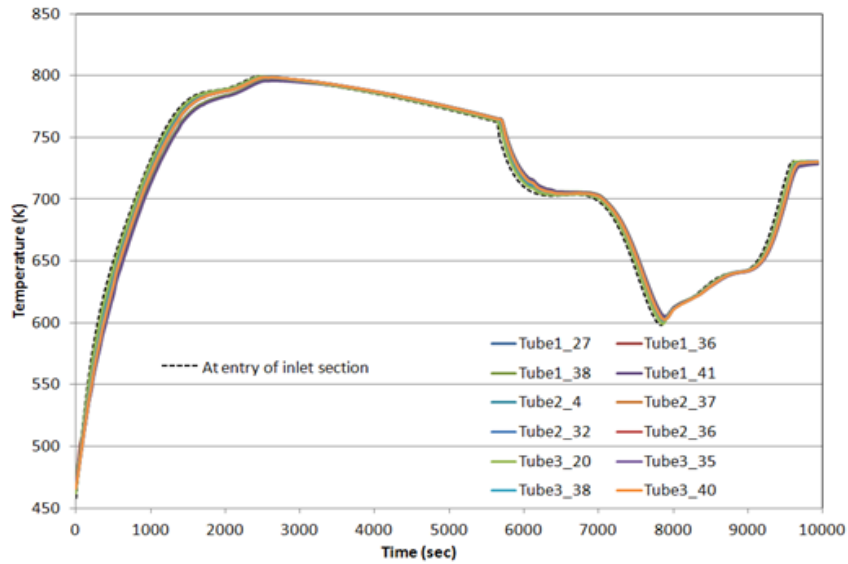
Figure 6.16 Mass-weighted-average steam temperatures at the exit of unfinned length of tubes – inlet section

Flue gas velocity and temperature distributions for the inlet section at different times are shown in figures 6.17 and 6.18, respectively.

106
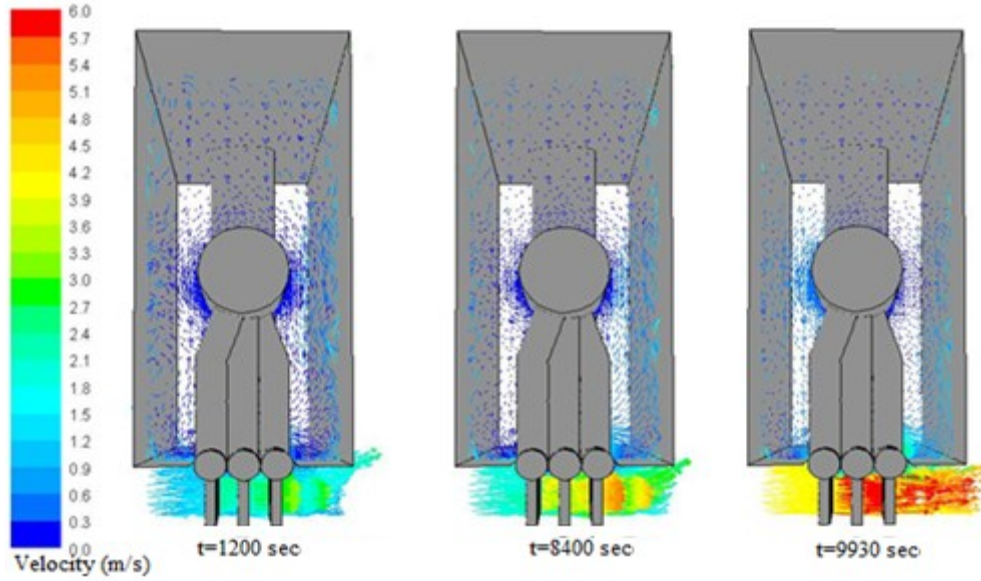
Figure 6.17 Flue gas velocity distribution for the inlet section
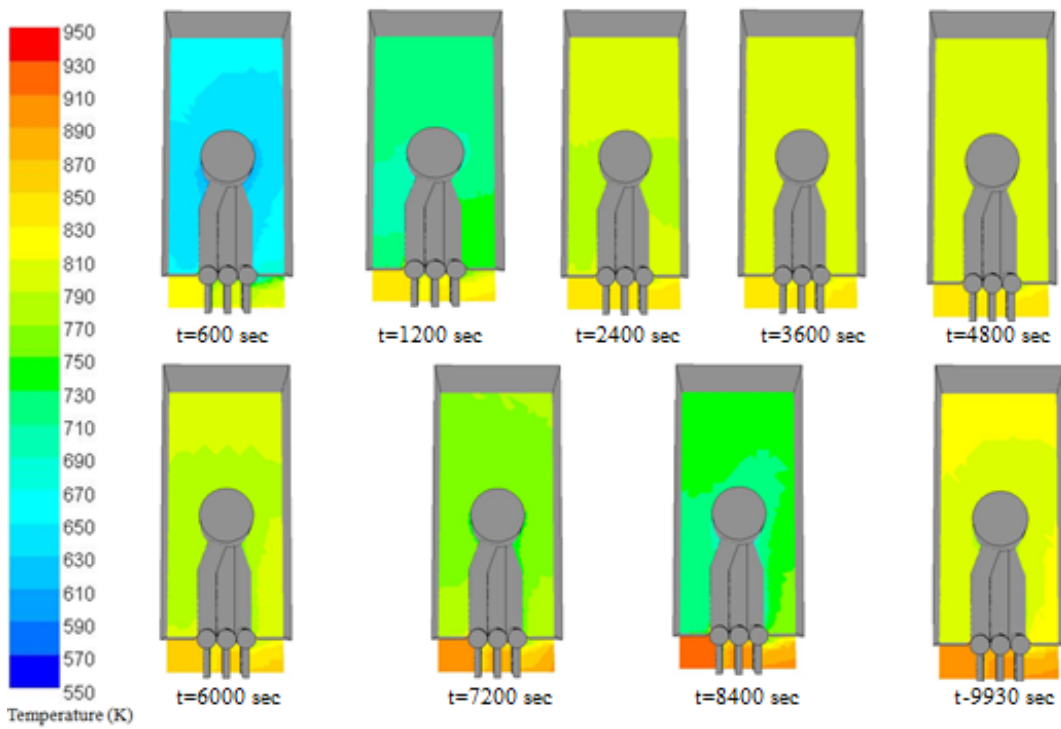
Figure 6.18 Flue gas temperature distribution for the inlet section

The pressure drop in steam across the inlet section, ΔP_1 (t), and the difference between the steam inlet and outlet mass flow rates, Δm (t), for the inlet

107

section at different times are listed in tables 6.1 and 6.2, respectively. It is observed that Δm (t) is negligible compared to the steam mass flow rate.

Time (sec)	Steam inlet pressure(Pa-g)	Steam outlet pressure(Pa-g)	Pressure drop (Pa)-ΔP₁(t)
0	1022948	1022692	248.2
300	2071780	2066905	4874.9
600	3269919	3267534	2385.0
1200	5870260	5866871	3388.2
1800	5919788	5914734	5054.0
3000	5760077	5754094	5983.0
3600	5712787	5707088	5699.0
4200	5687897	5682504	5393.5
4800	5678207	5672909	5298.5
5400	5675236	5669707	5529.0
6000	5671705	5665970	5734.5
6600	5664858	5658202	6655.5
7200	5654919	5647011	7908.0
7800	5644715	5636742	7973.5
8100	5643179	5636742	6437.0
8700	5649833	5636742	13091.5
9300	5673963	5636742	37221.5
9930	5776360	5692739	83621.5

Table 6.1 Pressure drop in steam across the inlet section

| Time (sec)	Steam inlet mass flow rate (kg/s)	Steam outlet mass flow rate (kg/s)	Δm(t)- (kg/s)
0	1.5500	1.5499	0.0001
300	4.3692	4.3662	0.0030
600	6.7094	6.7060	0.0034
1200	10.0214	10.0209	0.0005
1800	11.8238	11.8238	-0.0001
3000	12.5353	12.5350	0.0002
3600	12.2440	12.2438	0.0002
4200	11.9632	11.9631	0.0001
4800	11.9194	11.9193	0.0001
5400	12.2441	12.2438	0.0001
6000	12.9803	12.9800	0.0002
6600	14.1019	14.1021	-0.0001
7200	15.5457	15.5451	0.0007
7800	17.2570	17.2567	0.0004
8400	19.2483	19.2486	-0.0003
9000	21.6704	21.6706	-0.0002
9600	24.8977	24.8987	-0.0010
9930	26.0577	26.0577	0.0000

Table 6.2 Steam inlet and outlet mass flow rates for the inlet section

The flue gas side and steam side heat transfer rates to the inlet section components wall at different times are listed in table 6.3. A higher rate of convective heat transfer occurs on the steam side as compared to the flue gas side. It is also observed that the steam heats or cools the inlet section components wall depending on rate of change in steam temperature at the HPSH1 entry.

Time (sec)	Heat transfer rate from flue gas (w)	Heat transfer rate from steam (w)
300	28491.54	188489.18
600	21404.42	224348.48
900	16140.03	215416.13
1200	11604.82	184765.87
1800	7391.03	73519.09
2400	5648.04	42661.89
3000	5165.72	-577.10
3600	5421.53	-12757.29
4200	6196.03	-18765.66
4800	7605.46	-23670.19
5400	9676.37	-28645.74
6000	16971.02	-82004.89
6600	20582.23	-123553.02
7200	23583.97	-74327.51
7800	36279.11	-42859.63
8400	40604.10	-38719.73
9000	39842.41	-87627.45
9600	34451.06	-172153.80
9930	32227.16	-186127.49

Table 6.3 Heat transfer rates to the inlet section components wall

The inside and outside wall temperature distributions for the inlet section components at different times are shown in figures 6.19 and 6.20, respectively. A temperature difference is observed between the manifold and links of the section. This is because of the different rates of heating of these components, as the thicker-walled manifold takes longer to warm or cool as compared to the links.
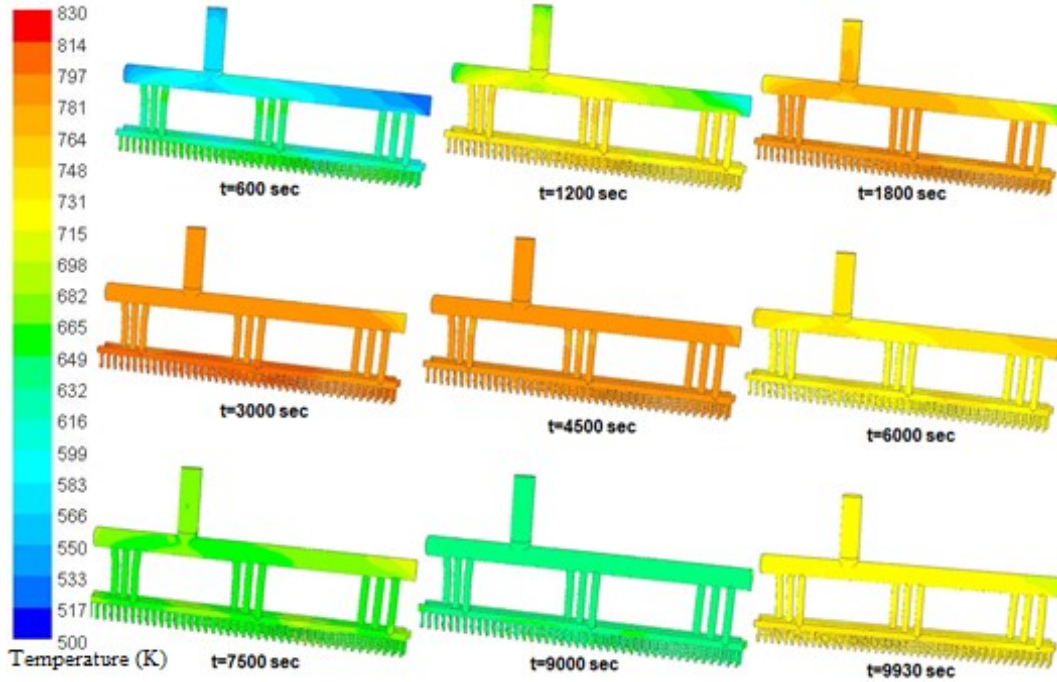
Figure 6.19 Inside wall temperature distribution for the inlet section at different
times
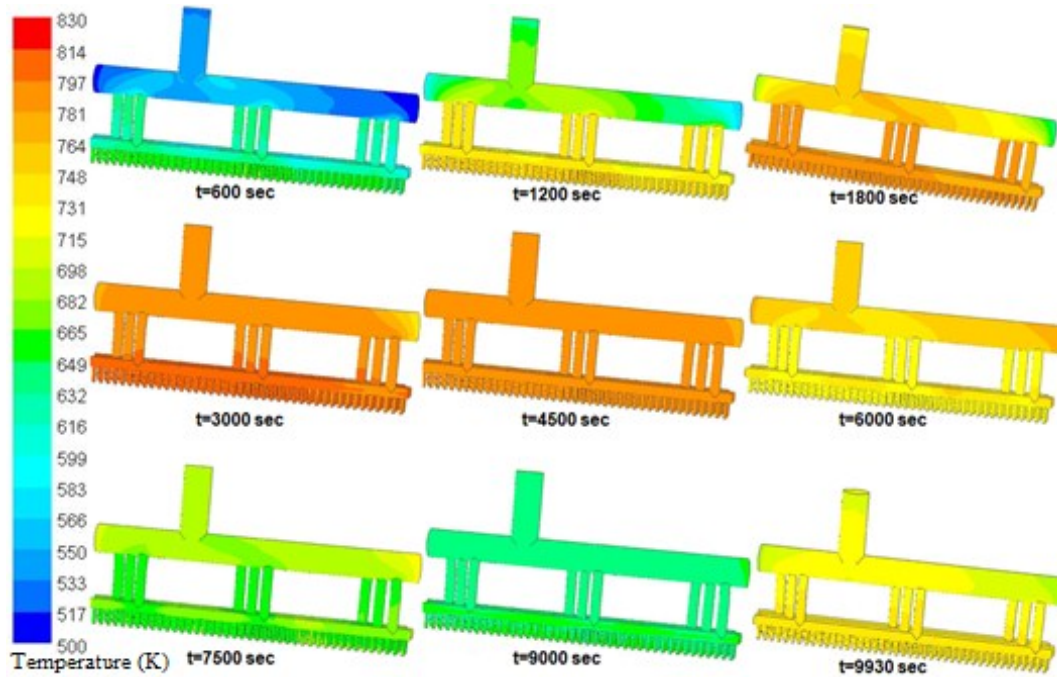
Figure 6.20 Outside wall temperature distribution for the inlet section at different
times

110

6.2.2 Harp tube section

Each row of the harp tubes are subdivided into four types based on the steam mass flow rate at their inlet. This is done to reduce computational cost of transient analysis. Shown in figures 6.21 – 6.23 are; type 1 tubes with the lowest steam mass flow rate, type 2 and 3 tubes with the next two higher flow rates, and type 4 tubes with the highest steam mass flow rate.

Figure 6.21 Subdivision of row 1 harp tubes into four types

Figure 6.22 Subdivision of row 2 harp tubes into four types
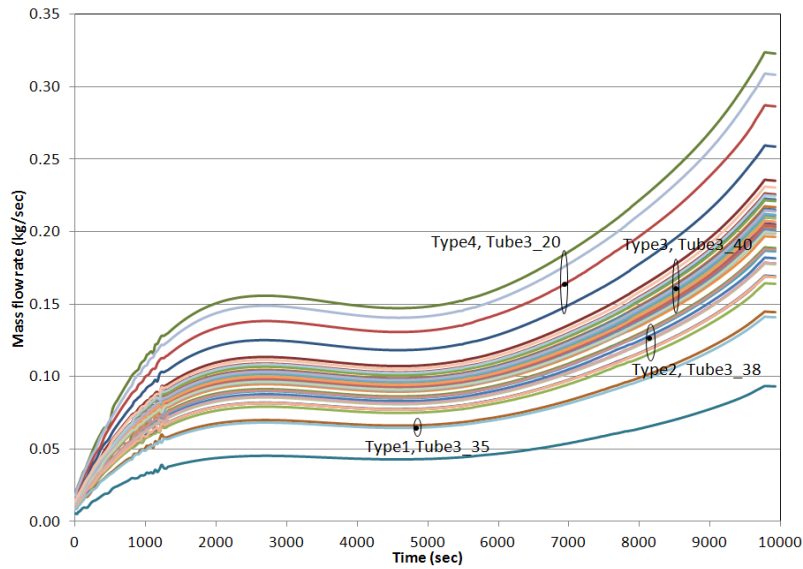
Figure 6.23 Subdivision of row 3 harp tubes into four types

Table 6.4 shows the set of tubes belonging to each type for the three rows. Only one harp tube from each type is solved for each of the three rows as highlighted in table 6.4.

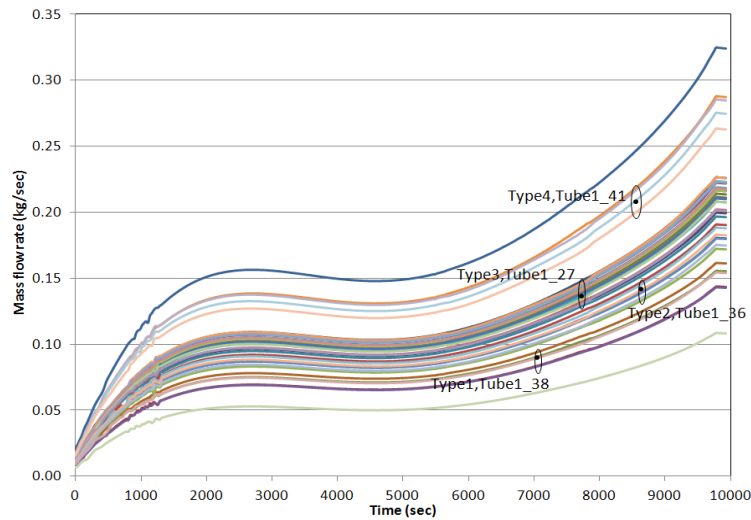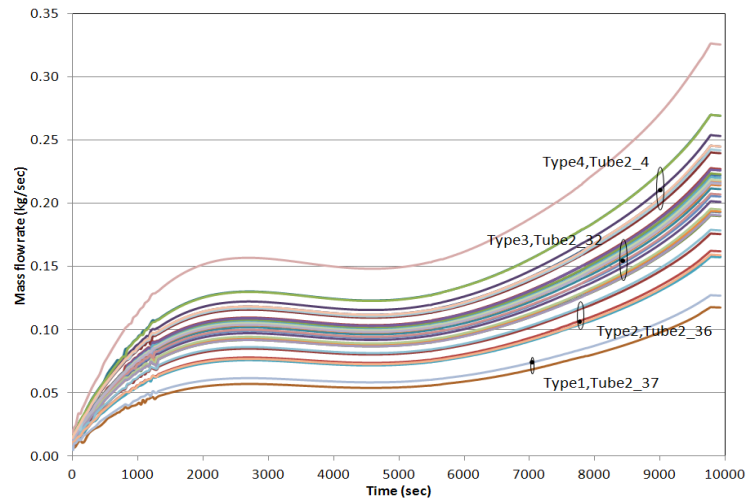| Row 1				Row2				Row3			
Type1	Type2	Type3	Type4	Type1	Type2	Type3	Type4	Type1	Type2	Type3	Type4
38	36	27	41	37	36	32	4	35	38	40	20
6	5	1	24	6	7	3	1	6	7	2	1
8	10	2	40		8	9	2		8	4	37
9	20	3	42		20	10	5		19	9	3
22	21	4			23	11	21		21	10	
	25	11			35	12	41		22	11	
	35	12				13	42		23	12	
	37	13				14			32	13	
		14				15			33	14	
		15				16			34	15	
		16				17			36	16	
		17				18				17	
		18				19				18	
		19				22				24	
		23				24				25	
		26				25				26	
		28				26				27	
		29				27				28	
		30				28				29	
		31				29				30	
		32				30				31	
		33				31				39	
		34				33				41	
						34				42	
						39					
						40					

Table 6.4 Set of harp tubes belonging to each type for the three rows

112

The temperature of flue gas for the harp tube section at every time instant is assumed to be uniform along the tube length, and calculated for each row from an overall heat balance between the steam and flue gas. Polynomial functions of time are fitted to represent the flue gas temperature for each row, figure 6.24.
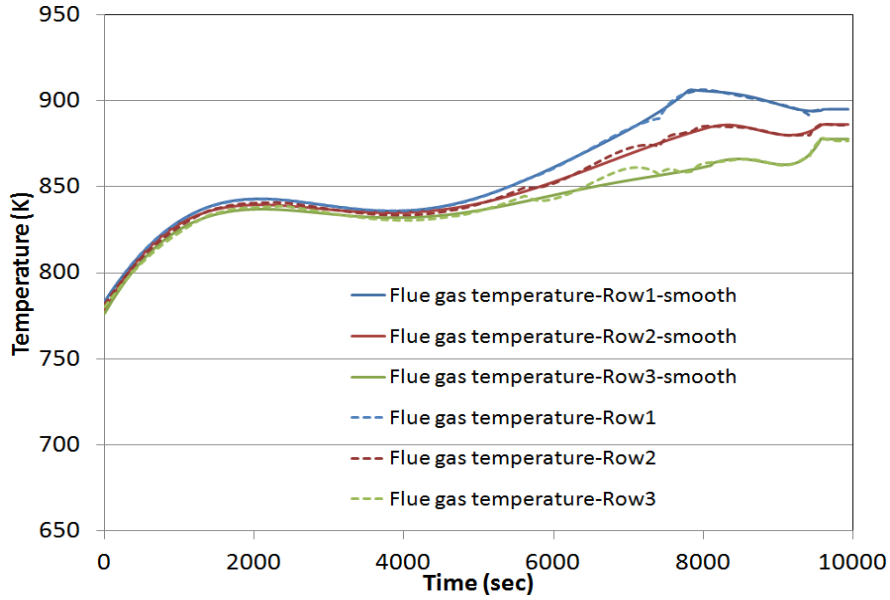
Figure 6.24 Flue gas temperatures for the three harp tube rows

The outside heat transfer coefficient, h_o, for the three rows of HPSH1 harp tubes at t=0 second is calculated analytically using equations (84), (85), (86), and (87) so as to match the steam temperature at harp tubes exit with the plant-measured temperature at the HPSH1 exit.

$$T_{stm,out} = T_f - (T_f - T_{stm,in}) exp^{\left(\frac{-l*U_O*\pi*d_o}{m*c_p}\right)} \tag{84}$$

$$\frac{1}{U_o} = \frac{1}{h_o} + \frac{A_o}{h_i*A_i} + \frac{t_w*A_o}{k*A_i} \tag{85}$$

$$T_f = \frac{Flue\ gas\ temperature\ for\ row\ 1 + Flue\ gas\ temperature\ for\ row\ 3}{2} \tag{86}$$

$$\dot{m} = \frac{Total\ steam\ mass\ flow\ rate\ through\ HPSH1\ harp\ tubes}{Total\ number\ of\ HPSH1\ harp\ tubes} \tag{87}$$

where,

$T_{stm,in}$=mass-weighted-average steam temperature at the inlet of harp tubes

$T_{stm,out}$=mass-weighted-average steam temperature at the outlet of harp tubes

T_f= average flue gas temperature for the HPSH1 harp tubes

l= length of finned harp tubes

$\dot{m}$= average steam mass flow rate through harp tube

d_o= outside harp tube diameter

U_o= overall heat transfer coefficient for harp tubes

h_o at t=0 second for the three harp tube rows is calculated to be equal to 15.6 W/m^2-K. The wall temperature distribution for each tube type for the three rows is provided by the steady state solution at t=0 second. This solution is calculated using h_o for the three tube rows, steam mass flow rate through each tube type for the three rows, and flue gas temperature for each of the three tube rows.

The mass-weighted-average steam temperature profile, inside and outside tube wall temperature profiles along the tube length for type 3 harp tube of row 1 at t= 0 second are shown in figure 6.25. The steam temperatures at the exit of each tube type for the three rows at t=0 second are listed in table 6.5.

	Type1	Type2	Type3	Type4
Row1	634.41	630.59	629.22	626.67
Row2	651.74	642.22	629.04	625.51
Row3	639.01	628.37	627.44	623.06

Table 6.5 Steam temperatures at the exit of each tube type at t=0 second
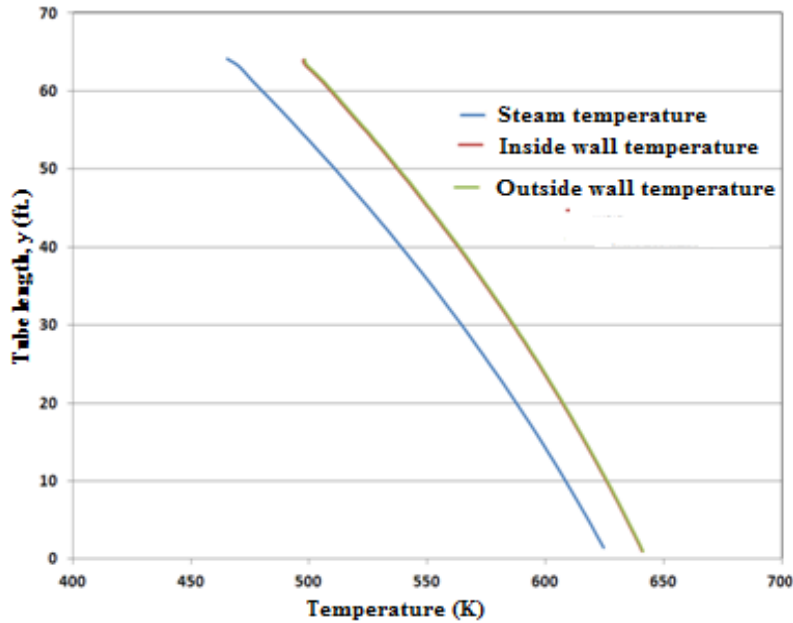
Figure 6.25 Results for type 3 harp tube of row 1 at t=0 second

The outside heat transfer coefficient profiles for the three harp tube rows along their length at different times are shown in figure 6.26. The profiles from t=1200 second to t=9930 second are calculated from the flue gas velocity distributions upstream of HPSH1 (obtained by solving the HRSG model). The profiles for time interval t=0 second to t=1200 second are obtained by linear interpolation between the profiles at t=0 second and t=1200 second. The interpolation is performed iteratively to match the mass-weighted-average steam temperature at the exit of harp tube section with the plant-measured steam temperature at the HPSH1 exit.
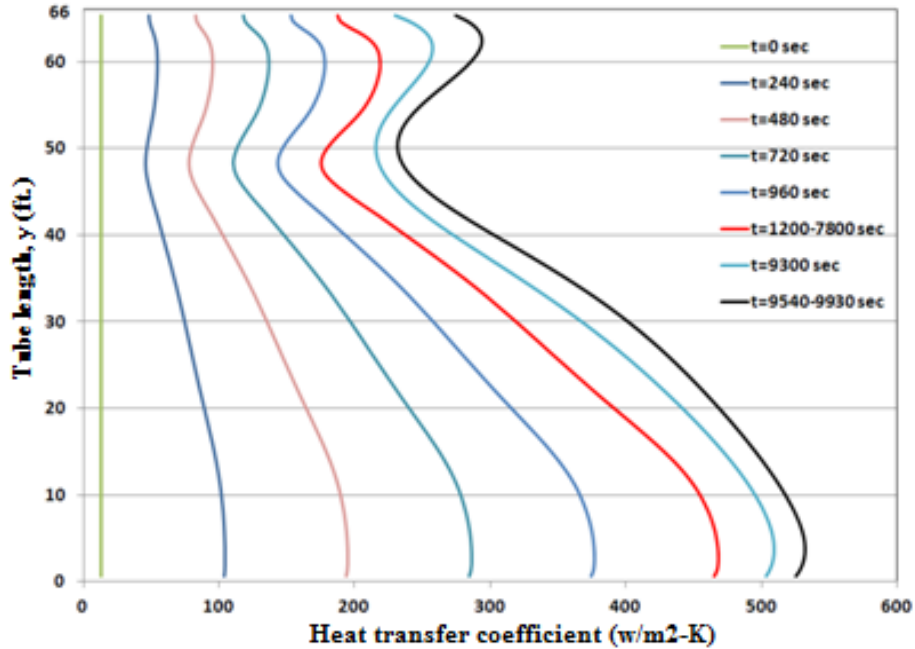
Figure 6.26 Outside heat transfer coefficient for the three harp tube rows

User-defined functions are used to define the time-dependent boundary conditions for transient analysis of the harp tube section. The computed time series plots of steam and flue gas temperature for each harp tube type are shown in figures 6.27 – 6.30.
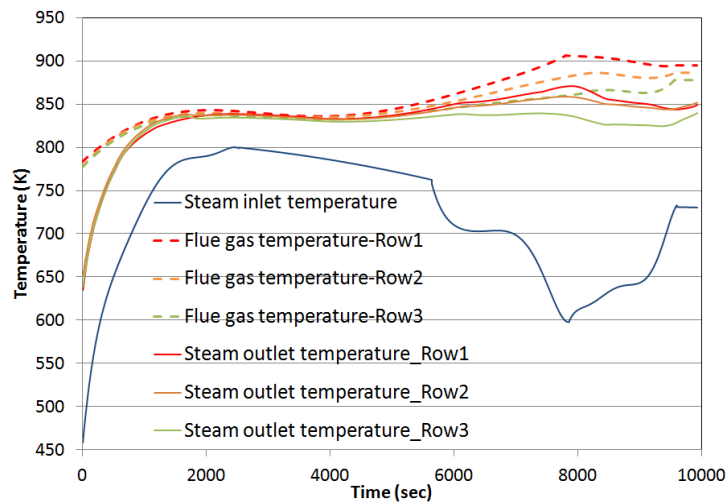
Figure 6.27 Steam and flue gas temperatures for type 1 harp tubes

116
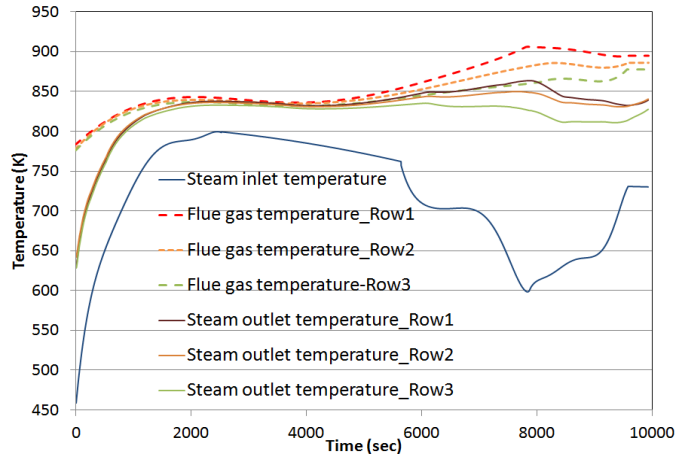
Figure 6.28 Steam and flue gas temperatures for type 2 harp tubes
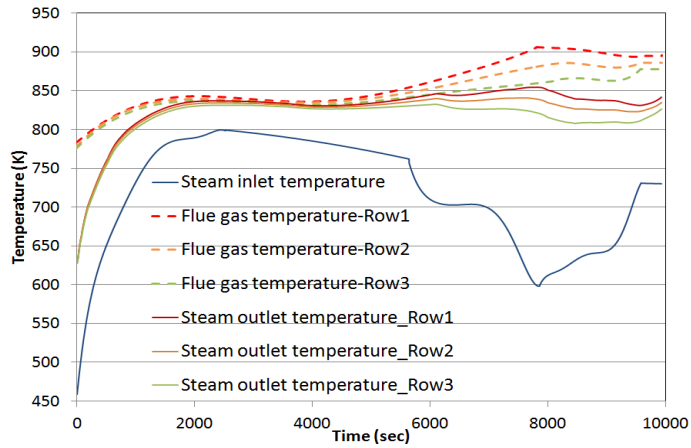
Figure 6.29 Steam and flue gas temperatures for type 3 harp tubes
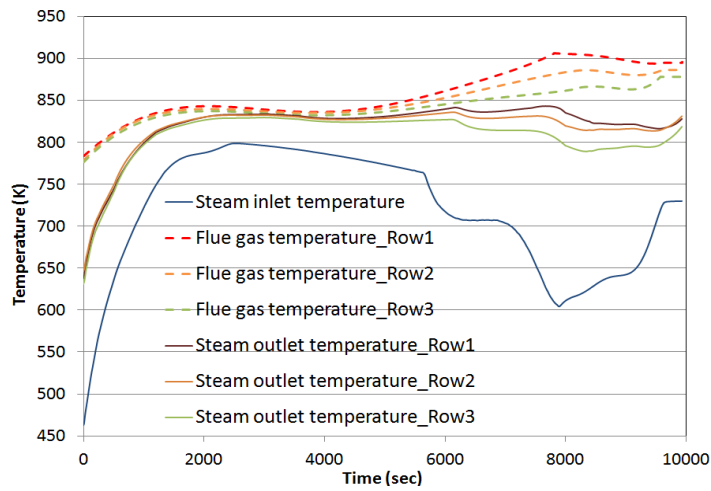
Figure 6.30 Steam and flue gas temperatures for type 4 harp tubes

117

The results show that steam temperature at the exit of first tube row is higher as compared to the two downstream rows. This is because of the gradual drop in flue gas temperature as it flows over the rows. Figure 6.31 shows the heat transfer rate to steam for each row of type 3 harp tube. Also, the mass-weighted-average steam temperature at the exit of the tubes is the lowest for type 4 tubes and the highest for type 1 tubes.
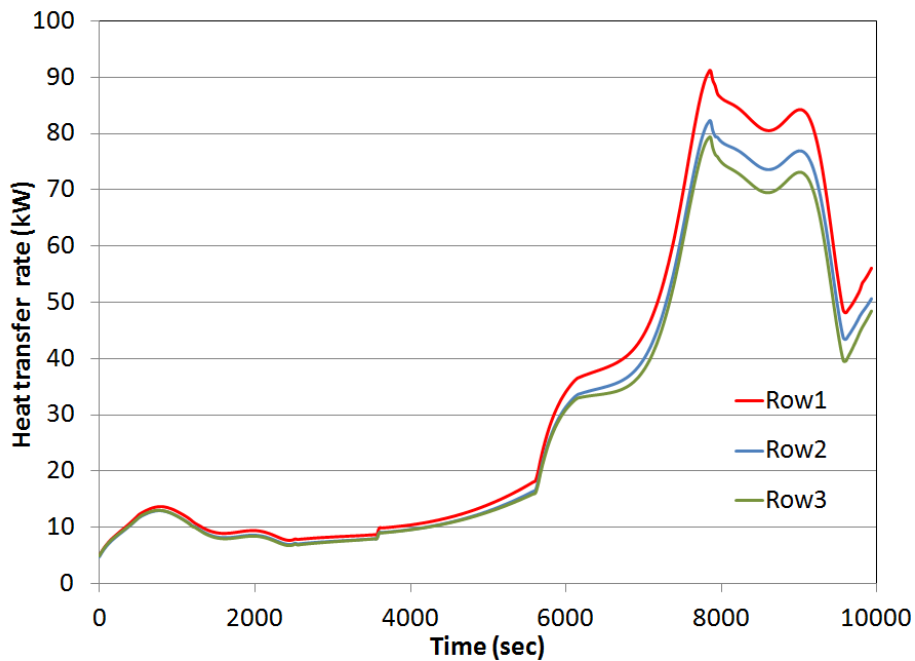

Figure 6.31 Heat transfer rate to steam for type 3 harp tubes

The maximum steam pressure drop across the harp tube section, ΔP_2 (t), at different times is listed in table 6.6. The difference between the inlet and outlet steam mass flow rates, Δm (t), for type 3 tube of row 1 at different times is given in table 6.7. Δm (t) is negligible as compared to the nominal mass flow rate through the tube.

Time (sec)	Max. steam inlet pressure (Pa)-calc.	Steam outlet pressure (Pa)-B.C	Max. pressure drop (Pa) - $\Delta P2(t)$
300	2071875	2070358	1516.8
600	3276664	3267494	9170.0
1200	5876264	5866818	9445.8
1800	5926389	5914736	11721.1
3000	5767809	5754089	13720.6
4200	5695001	5682452	12548.5
6000	5680315	5665974	14410.0
7500	5650529	5636740	13789.5
8100	5658252	5633982	24269.5
8700	5669145	5637498	31646.9
9300	5700516	5656873	43643.8
9930	5744160	5692725	51365.9

Table 6.6 Steam pressure drop across the harp tube section

Time (sec)	Steam inlet mass flow rate (kg/s)-B.C	Steam outlet mass flow rate (kg/s)-calc	$\Delta m(t)$- (kg/s)
30	0.0128	0.0133	-0.0005
600	0.0456	0.0455	0.0000
1200	0.0678	0.0680	-0.0001
1800	0.0801	0.0801	0.0000
3000	0.0851	0.0851	0.0000
4200	0.0812	0.0812	0.0000
6000	0.0881	0.0881	0.0000
7500	0.1111	0.1110	0.0000
8100	0.1234	0.1234	0.0000
8700	0.1380	0.1380	0.0000
9300	0.1571	0.1572	-0.0001
9930	0.1769	0.1770	-0.0001

Table 6.7 Steam inlet and outlet mass flow rates for type 3 tube of row 1

The inside and outside tube wall temperature profiles along the tube length for type 3 tubes at different times are shown in figures 6.32 – 6.37.
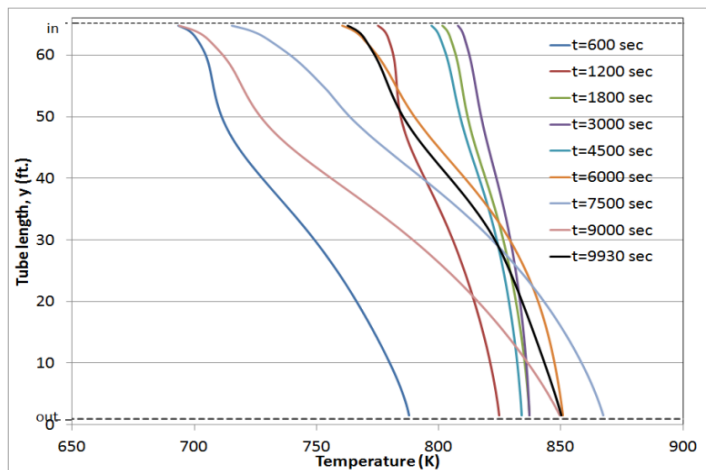
Figure 6.32 Inside wall temperature for type 3 harp tube of row 1
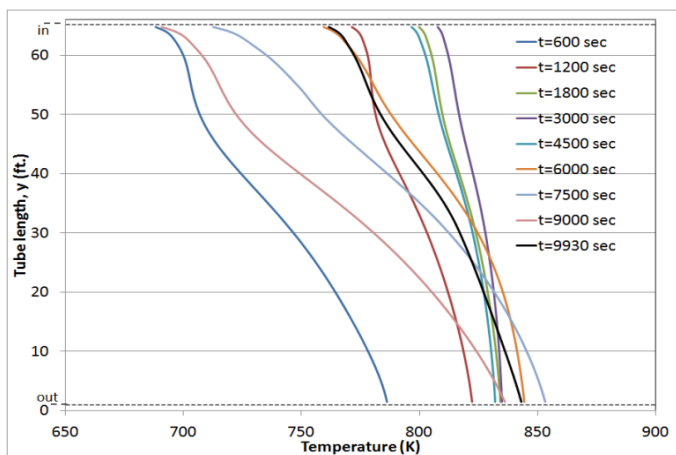
Figure 6.33 Inside wall temperature for type 3 harp tube of row 2
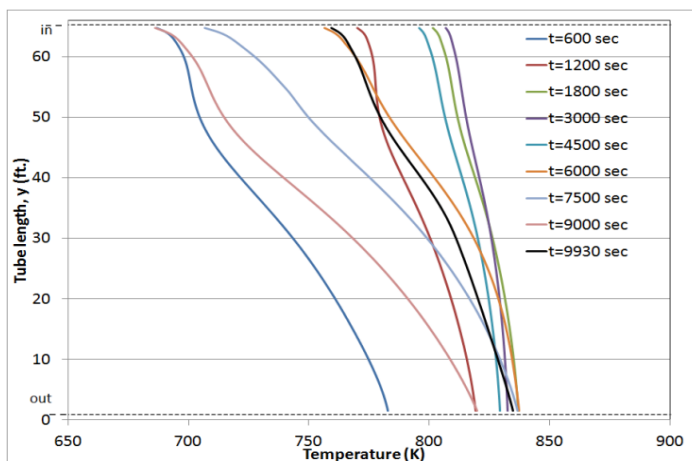

Figure 6.34 Inside wall temperature for type 3 harp tube of row 3

120
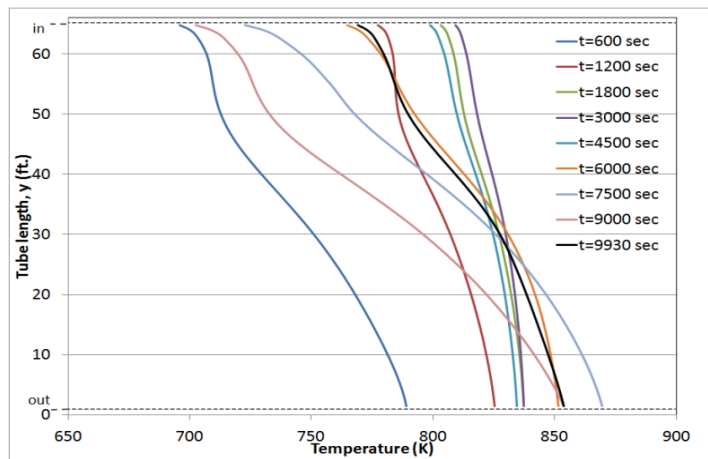
Figure 6.35 Outside wall temperature for type 3 harp tube of row 1
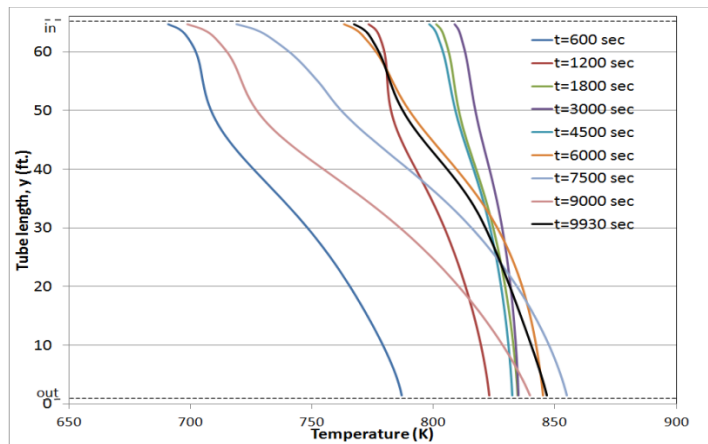
Figure 6.36 Outside wall temperature for type 3 harp tube of row 2
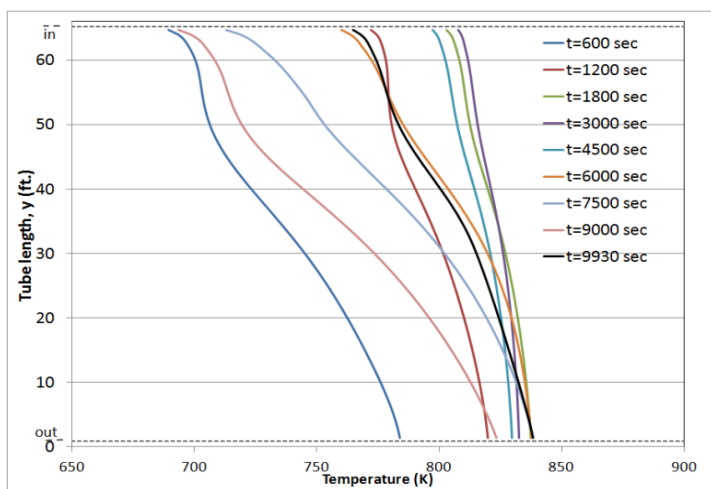
Figure 6.37 Outside wall temperature for type 3 harp tube of row 3

121

6.2.3 Outlet section

The initial condition for the outlet section is obtained from steady state solution corresponding to the operating condition at t=0 second. The steam temperature, and wall inside and outside temperature distributions for the components at t=0 second are shown in figures 6.38 and 6.39, respectively.
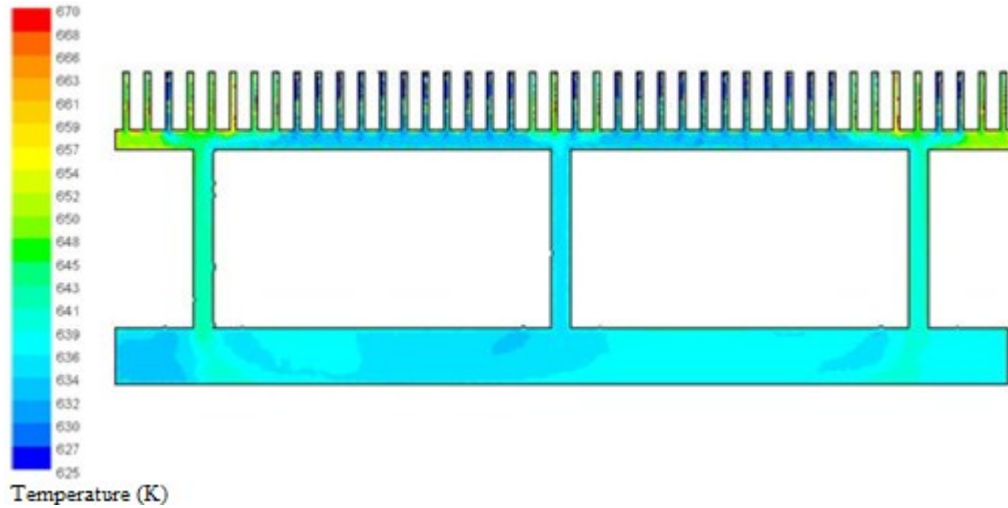
Figure 6.38 Steam temperature distribution in the outlet section at t=0 second
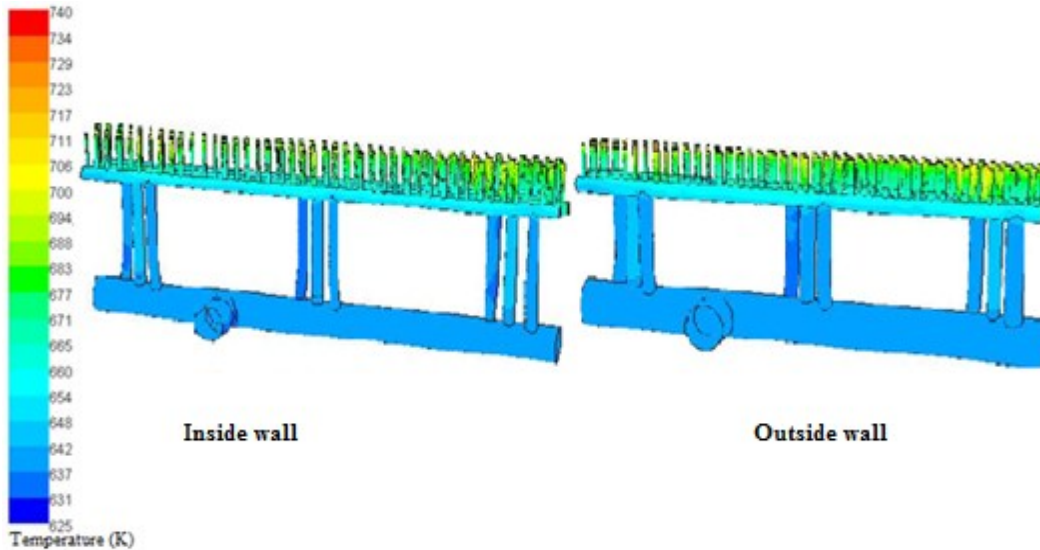
Figure 6.39 Outlet section components wall temperature distributions at t=0 second

User-defined functions are constructed to define the time-dependent boundary conditions for the outlet section transient analysis. The computed mass-weighted-average steam temperature at the exit of the section, figure 6.40, is found to be within ±8 K of the plant-measured temperature.
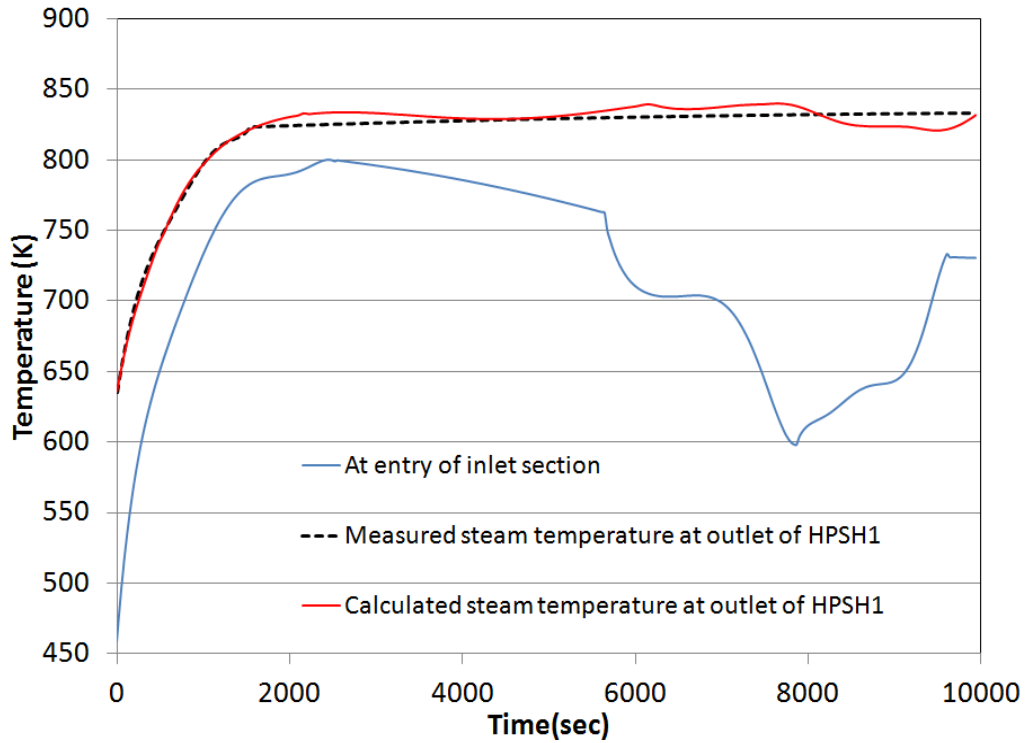
Figure 6.40 Mass-weighted-average steam temperatures for different sections of the HPSH1

Flue gas velocity and temperature distributions for the outlet section at different times are shown in figures 6.41 and 6.42, respectively.
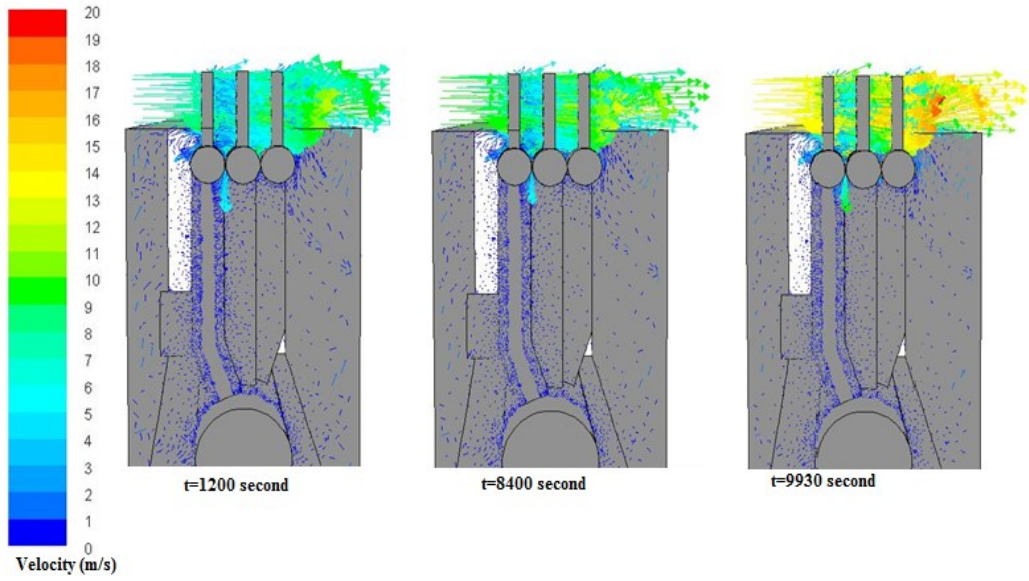
Figure 6.41 Flue gas velocity distribution for the outlet section
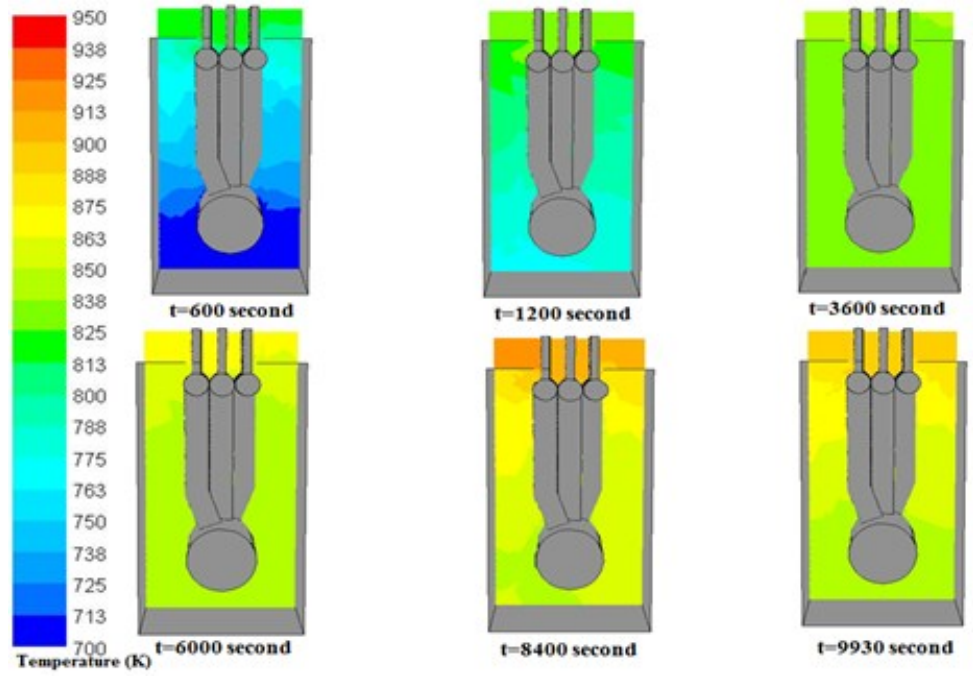
Figure 6.42 Flue gas temperature distribution for the outlet section

The inside and outside wall temperature distributions for the outlet section

components at different times are shown in figures 6.43 and 6.44, respectively.

The row 1 header and links are hotter as compared to the headers and links of the

124

subsequent rows. This is because of the higher steam temperature at the exit of row 1 finned harp tubes. The links to manifold temperature difference is also observed, this is because of their different wall thicknesses.

The pressure drop in steam across each of the three HPSH1 sections at different times is given in table 6.8. These results justify the assumption that the total pressure drop in steam across the HPSH1 at any time is very small as compared to the plant-measured pressure at the HPSH1 exit. It is also possible to solve again for the inlet and harp tube sections starting from t=8700 second to t=9930 second with the steam pressure at their exit equal to $P_o(t)+\Delta P_2(t)+\Delta P_3(t)$ and $P_o(t)+\Delta P_3(t)$, respectively, to reduce the ΔP to 56375 Pa, less than 1 percent of the measured pressure value.
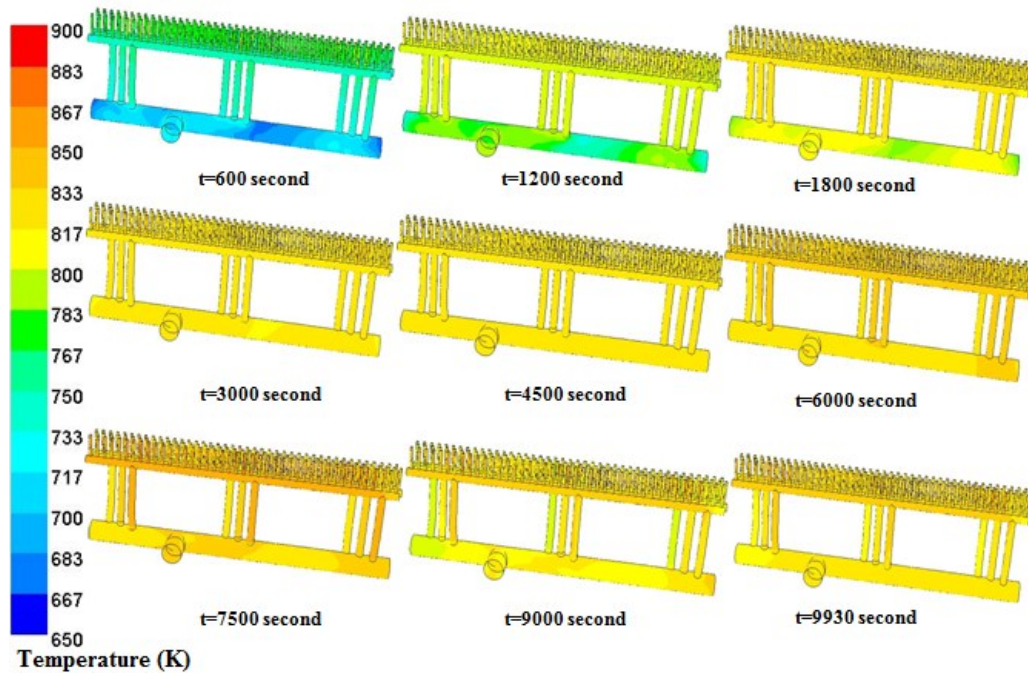
Figure 6.43 Inside wall temperature distribution for the outlet section at different times
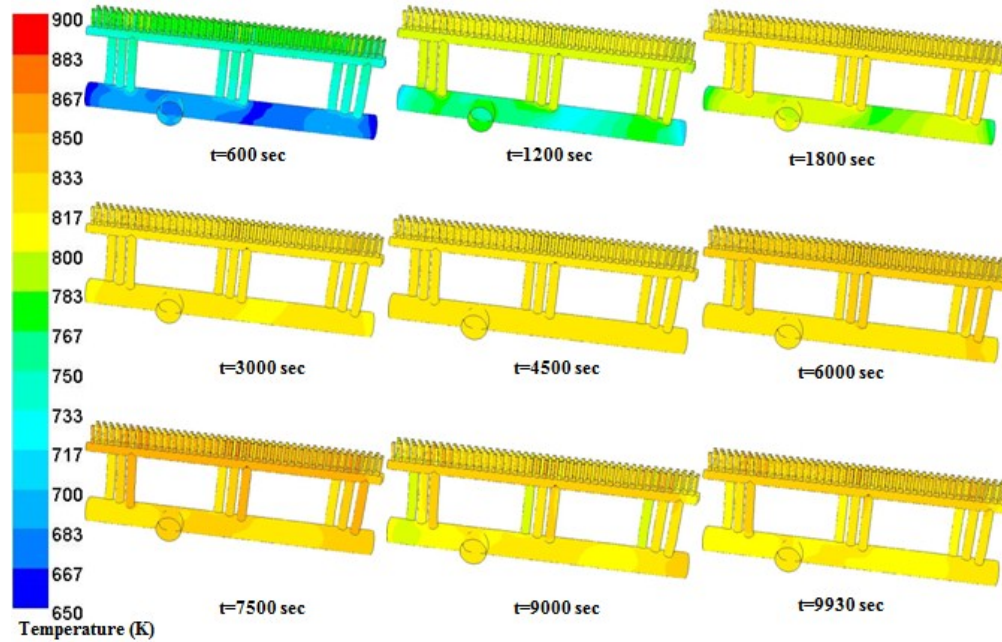
Figure 6.44 Outside wall temperature distribution for the outlet section at different times

Time (sec)	HPSH1 outlet Pressure $P_o(t)$-(Pa-g)	For *inlet section* $\Delta P_1(t)$-(Pa)	For *harp tubes section* $\Delta P_2(t)$-(Pa)	For *outlet section* $\Delta P_3(t)$-(Pa)	Total pressure drop-(Pa) $\Delta P(t)=\Delta P_1(t)+\Delta P_2(t)+\Delta P_3(t)$
300	2070388	4874.9	1507.1	3041.3	9423.4
600	3267533	2385.0	9147.1	4882.9	16415.1
1200	5866871	3388.2	9421.2	6372.7	19182.1
1800	5914734	5054.0	11700.0	9074.2	25828.2
3000	5754094	5983.0	13716.0	10631.3	30330.3
3600	5707089	5699.0	8125.4	10177.9	24002.4
4200	5682504	5393.5	12528.5	9724.1	27646.1
4800	5672909	5298.5	7666.0	9684.5	22648.9
5400	5669708	5529.0	8229.9	10303.4	24062.3
6000	5665972	5734.5	14404.0	11790.7	31929.2
6600	5658202	6655.5	10607.9	13923.9	31187.4
7200	5647013	7908.0	12640.5	17046.5	37595.0
7800	5636744	7973.5	13818.5	21116.5	42908.4
8100	5633991	6437.0	24267.0	23187.3	53891.3
8700	5637522	13091.5	31638.5	28579.6	73309.6
9300	5656873	37221.5	43658.5	36905.0	117785.0
9930	5692771	83621.5	51395.0	47435.5	182452.0

Table 6.8 Pressure drop in steam across each of three HPSH1 sections

The computed steam mass flow rates at the entry and exit of HPSH1 are shown in figure 6.45. These results justify the assumption that the difference

126

between steam mass flow rates at the HPSH1 entry and the exit at any time is negligible compared to the nominal mass flow rate through it.
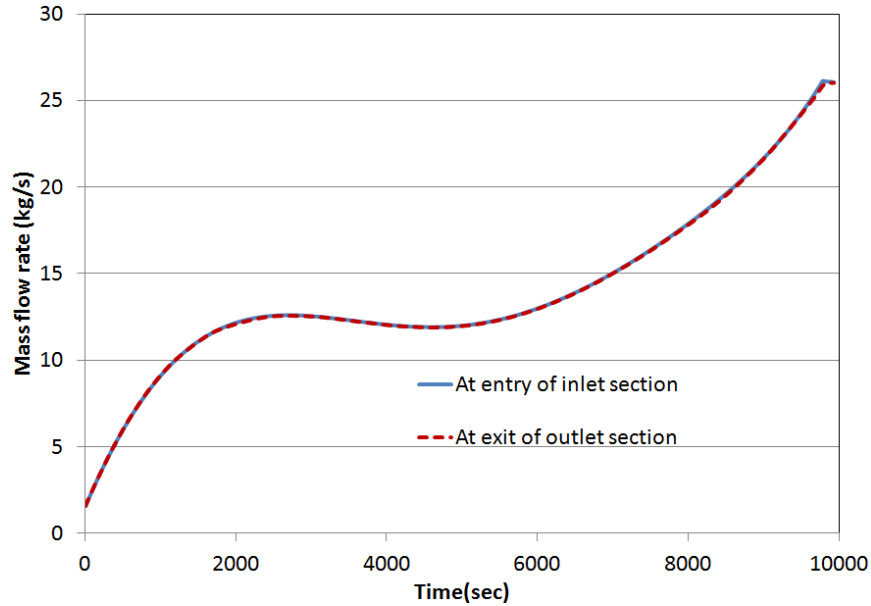
Figure 6.45 Steam mass flow rates for HPSH1

The heat transfer rates to steam for each of the three sections of HPSH1 at different times are shown in table 6.9. 99 percent of the total HPSH1 heat transfer rate is seen to occur in the harp tube section.

Time (sec)	Heat trasfer to steam for inlet section (kW)	Heat trasfer to steam for harp tube section (kW)	Heat trasfer to steam for outlet section (kW)	Heat trasfer to steam for the entire HPSH1 (kW)
300	-164.24	3537.11	7.64	3380.51
600	-192.52	4669.92	4.59	4481.99
1200	-159.27	4280.00	2.18	4122.91
3000	0.74	1819.97	0.86	1821.57
4800	19.18	2942.82	1.34	2963.34
6000	95.88	6200.35	2.77	6299.00
6600	29.23	8551.09	4.61	8584.94
7800	125.67	15765.89	7.31	15898.87
9000	8.59	19085.07	10.33	19103.99
9900	-17.18	15463.87	9.86	15456.55

Table 6.9 Heat transfer to steam for each of the three sections of HPSH1

6.3 Structural analysis for HPSH1

Structural analysis of HPSH1 for the cold start-up transient will be performed in future using the following thermal-fluid analysis results:

- Inside and outside wall temperature distributions for manifold, links, headers, and unfinned tubes of the inlet section every 30 seconds for 9930 seconds;

- Inside and outside wall temperature profiles for finned harp tubes along their length every 30 seconds for 9930 seconds;

- Inside and outside wall temperature distributions for manifold, links, headers, and unfinned tubes of the outlet section every 30 seconds for 9930 seconds.

- Average time-dependent steam pressure values for the inlet section, harp tube section, and outlet section after every 30 seconds for 9930 seconds.

First, a transient thermal conduction analysis will be performed for 9930 seconds based on the inside and outside wall temperature distributions. Next, a quasi steady-state structural analysis will be carried out using the temperature distributions from thermal conduction analysis and the time-dependent steam pressure values.

CHAPTER 7

CONCLUDING REMARKS AND FUTURE WORK

7.1 Concluding Remarks

Finite volume CFD and finite element FEA numerical methodologies were adopted to carry out thermal-fluid and structural analysis, respectively, for the high pressure superheater 1 (HPSH1) of Santan unit-5B heat recovery steam generator (HRSG). This analysis was done to address the thermal-structural stress field induced in HPSH1 components during a cold start-up transient. Prior to the cold start-up transient analysis, thermal-structural analysis was performed at full-load steady state condition in order to gain confidence in the CFD and FEA methodologies. All analysis was performed for one symmetrical half of the HPSH1 to reduce computational cost.

Due to the large computational domain required for the analysis, the HPSH1 was modeled as an assembly of three sections: inlet section, harp tubes section, and outlet section. First, flue gas velocity and pressure distributions were solved for the HPSH1 region within HRSG. Next, thermal-fluid simulations were performed sequentially for the inlet section, harp tube section, and outlet section. The results of thermal-fluid analysis at full-load steady state and cold start-up transient conditions were presented; structural analysis results were shown only for the full-load steady state condition. Conclusions from the full-load steady state and cold start-up transient analyses are as follows.

Full-load steady state analysis: flue gas velocity distribution was non-uniform over the HPSH1 tube bank, with higher gas mass flow rate in the lower

region of the HRSG. Inlet section analysis results led to the observation that the headers were at higher temperature as compared to the manifold and links. This was due to lower flue gas temperature and velocity around the manifold and links. The harp tube section results revealed that the mass-weighted-average steam temperature at the exit of the harp tubes was highest for the tube row 1 and lowest for the tube row 3. This was due to a gradual temperature drop in the flue gas as it flowed over the rows. The difference in steam temperature at the exit of harp tubes resulted in the outlet header and links of tube row 1 being at higher temperature as compared to the rows 2 and 3 headers and links. Steam temperature at the HPSH1 exit was calculated to be 841.5K; this is in good agreement with the plant measured value (840K). It was observed that 99 percent of the total HPSH1 heat transfer occurred in the harp tube section. The calculated outer wall temperature at specific locations of the inlet links and outlet manifold were found to be in agreement with the plant-measured temperature values.

Subsequent structural analysis of the HPSH1 assembly revealed that the peak effective stresses were located at the connecting regions of the manifold and links for the inlet section, and at the connecting regions of the headers and un-finned tubes for the outlet section. The corresponding factors of safety based on the yield strength and tensile strength were calculated to be 4.8 and 6.8, respectively. These were well above their minimum values.

Cold start-up transient analysis: this analysis was carried out for a time interval of 9930 seconds; at the end of this time interval, the steam mass flow rate

at the HPSH1 exit had attained the full-load steady state value. Analysis of the inlet section showed that steam either heated or cooled the thick-walled components of the section (manifold, links, and headers) depending upon the rate of change in steam temperature at the HPSH1 entry. A higher convective heat transfer rate occurred on the steam side as compared to the flue gas side for these components. Difference in wall thickness of the section components led to the different rates of heating of these. This resulted in a significant temperature difference between the manifold and links as the thicker-walled manifold took longer to warm or cool as compared to the links. The harp tubes were subdivided into four types for each row based on the steam mass flow rate through them in order to reduce the computational cost of transient analysis – type 1 had the lowest and type 4 the highest steam flow rate. Results for the harp tube section showed that mass-weighted-average steam temperature at the exit of the tubes was the lowest for type 4 and the highest for type 1 tubes. Also, the steam temperature at the exit of harp tube row 1 was higher, as compared to the two downstream rows because of decrease in flue gas temperature across the rows. This resulted in the outlet header and links of row 1 being hotter. The links-to-manifold temperature difference was also observed in the outlet section because of their different wall thickness. The calculated mass-weighted-average steam temperature at HPSH1 exit was found to be within ±8 K of the plant-measured temperature value. During the analysis, there was some steam accumulation inside the HPSH1; however, the difference between steam mass flow rates at the HPSH1

entry and exit was less than 0.5 percent of the nominal mass flow rate at HPSH1 exit.

This analysis showed that there was a larger temperature difference between the components of HPSH1 during a cold start-up as compared to the full-load steady state because of rapid changes during the transient, especially in steam temperature at the HPSH1 entry, as well as different rates of heating of components with different wall thicknesses.

7.2 Future work

Results obtained from cold start-up transient thermal-fluid analysis of HPSH1, such as the inside and outside wall temperature distributions in the components, and the steam pressure in each section, will be used to carry out structural analysis.

The CFD and FEA models developed can also be applied to other plant transients such as hot start-up, shut-down, and daily load change cycle to obtain the thermal-structural stress field induced in the HPSH1. Analysis of various plant transients will enable estimation of the fatigue life of the HPSH1 components.

REFERENCES

1. Ganapathy, V., "Heat recovery steam generators: performance management and improvement", in <u>Power plant life management and performance improvement</u>, Oakey, J. E. editor, Woodhead Publishing, (2011), pp. 606-634.

2. <u>ASME Boiler and Pressure Vessel Code Section I—Rules for Construction of Power Boilers</u>, American Society of Mechanical Engineers, New York, 2007.

3. Brown, T. B., "Assessing the effect of Thermal transients on the life of boiler plant," Babcock Energy Limited, Scotland, 1994.

4. Lu S., and Wilson B., "On-line stress calculation and life monitoring systems for boiler components", Trans. of the Institute of Measurement and Control, 1998.

5. Bauver, W., Perrin, I., and Mastronarde, T., "Fast Startup and Design For Cycling of Large HRSGs" POWER-GEN International, Las Vegas, Nevada, December 9-11, 2003.

6. Wilson, AB and Purper, H., "New Developments in Lifetime Monitoring of High Temperature Piping Systems", Proc. of Life Assessment of Industrial Components and Structures conference, Cambridge, 1993.

7. Węglowski, B., Taler, J., Duda, P., "Monitoring of Thermal Stresses in Steam Generators," Transactions of the 17th International Conference on Structural Mechanics in Reactor Technology (SMiRT 17), Prague, Czech Republic, August 17 –22, Paper # D05-2, 2003.

8. <u>Optimization of Heat Recovery Steam Generator Startup and Shutdown in F-Class Units: Avoidance of Cracking in Thick-Section Pressure Parts</u>, Electric Power Research Institute, Palo Alto, CA: 2009. 1015464.

9. Taler, J., Węglowski, B., Zima, W., Grądziel, S., Zborowski, M., "Analysis of Thermal Stresses in a Boiler Drum During Start-Up", Journal of Pressure Vessel Technology, Trans. of the ASME, Vol.121, (1999), pp. 84-93.

10. Duda, P., Taler, J., "Numerical Method for the Solution of Non-Linear Two-Dimensional Inverse Heat Conduction Problem using Unstructured Meshes", International Journal for Numerical Methods in Engineering 48, (2000), pp. 881-899.

11. Martinez. E, Vicente. W, Salinas. M, Soto. G. "Single-phase experimental analysis of heat transfer in helically finned heat exchanger", Applied Thermal Engineering, November 3-2008.

12. ANSYS-Fluent 13.0 - User's Guide. 2010.

13. Idelchik, I. Handbook of hydraulic resistance. 3rd. edition, CRC Press, Boca Raton, Florida, 1994.

14. Bejan, Adrian, and Allan D. Kraus., Heat transfer handbook. Hoboken New Jersey: John Wiley & Sons, Inc, 2003.

15. Ashrafi-Nik, M. "Thermo-hydraulic Optimization of the EURISOL DS target". Paul Scherrer Institute, 2006.